Alma Mater Studiorum – Università di Bologna

DOTTORATO DI RICERCA IN

MECCANICA E SCIENZE AVANZATE DELL'INGEGNERIA (DIMSAI)

Ciclo XXXIII

Settore concorsuale: 09/A2 - Meccanica applicata alle macchine

Settore scientifico disciplinare: ING-IND/13 Meccanica Applicata alle Macchine

Advanced Mission Synthesis Algorithms for Vibration-based Accelerated Life-testing

Presentata da: Pesaresi Emanuele

Coordinatore Dottorato:
Prof. Marco Carricato

Supervisore:
Prof. Marco Troncossi

Esame finale anno 2021

Abstract

In the field of vibration qualification testing, with the popular Random Control mode of shakers, the specimen is excited by random vibrations typically set in the form of a Power Spectral Density (PSD). The corresponding signals are stationary and Gaussian, i.e. featuring a *normal distribution*. Conversely, real-life excitations are frequently non-Gaussian, exhibiting high peaks and/or burst signals and/or deterministic harmonic components. The so-called *kurtosis* is a parameter often used to statistically describe the occurrence and significance of high peak values in a random process. Since the similarity between test input profiles and real-life excitations is fundamental for qualification test reliability, some methods of kurtosis-control can be implemented to synthesize realistic (non-Gaussian) input signals.

Durability tests are performed to check the resistance of a component to vibration-based fatigue damage. A procedure to synthesize test excitations which starts from measured data and preserves both the damage potential and the characteristics of the reference signals is desirable. The Fatigue Damage Spectrum (*FDS*) is generally used to quantify the fatigue damage potential associated with the excitation. The signal synthesized for *accelerated durability tests* (i.e. with a limited duration) must feature the same *FDS* as the reference vibration computed for the component's expected lifetime. Current standard procedures are efficient in synthesizing signals in the form of a *PSD*, but prove inaccurate if reference data are non-Gaussian.

This work presents novel algorithms for the synthesis of accelerated durability test profiles with prescribed *FDS* and a non-Gaussian distribution. An experimental campaign is conducted to validate the algorithms, by testing their accuracy, robustness, and practical effectiveness. Moreover, an original procedure is proposed for the estimation of the fatigue damage potential, aiming to minimize the computational time. The research is thus supposed to improve both the effectiveness and the efficiency of excitation profile synthesis for accelerated durability tests.

Acknowledgments

The research was financially supported by *Easting s.r.l.s.* (Trieste, Italy), which the author gratefully acknowledges.

Contents

Nomenclature

The main symbols and parameters appearing throughout the dissertation are the following:

Symbol	Description
DUT	Device under test
$D(f_n)$	Expected value of the Fatigue Damage if the DUT had a natural frequency equal to f_n
$G(f_n)$	PSD value at the frequency f_n
$z_{rms}(f_n)$	Root mean square of the relative displacement between the output and the input of the system, with the latter having natural frequency f_n
K	Proportionality constant between mechanical stress and relative displacement
b	Constant related to the slope of Wohler's curve[1]
C	Constant appearing in the Wohler's curve equation
Q	Quality factor of the system
$z(t)$	Relative displacement between the output and the input of the system at time t
$h(t)$	Impulse response of the system/DUT
RV	Random variable
ΔZ	RV related to the difference between a peak and its corresponding valley, both belonging to the relative displacement $z(t)$
$f_{\Delta Z}(\Delta z)$	The probability density of the $RV\ \Delta Z$ when the latter assumes the value Δz
$\mathrm{N_p}$	Number of positive peaks of the relative displacement per unit time
n	Number of concatenated blocks that compose a signal
k_j	Kurtosis of the j^{th} block
σ_j	Standard deviation of the j^{th} block
σ_{tot}	Standard deviation of the overall signal
k_{tot}	Kurtosis of the overall signal
T_j	Duration of the j^{th} block
T	Duration of the overall signal
N_{tot}	Number of samples of the overall signal
N_s	Sum of the number of samples contained in the:1st,2nd,…,s^{th} signal/block
n_s	Number of samples of the s^{th} signal/block

[1] If N_f is the number of cycles with sinusoidal amplitude σ that lead the DUT to failure, Wohler's curve (also known as *S-N* curve or Basquin's law) has the form: $\sigma^b N_f = C$ (where C is a constant). By taking the logarithm of the equation and applying simple algebraic manipulations, one can write: $\log(\sigma) = \left(-\frac{1}{b}\right)\log(N_f) + \frac{1}{b}\log(C)$. Therefore, in log-log scale, with $\log(\sigma)$ as the y coordinate and $\log(N_f)$ as the x coordinate, the slope of the curve is given by: $-\frac{1}{b}$.

Introduction and Overview

The main purpose of this work is to improve the current state of the art of mono-axial vibration fatigue tests. In order to discern the original content of the dissertation from the already available state of the art, a necessary contextualization will be given in the following.

In real-life applications, components are often subjected to stochastic loads that might lead to a premature failure; therefore, experimental tests are needed to check resistance to environmental vibrations. The tests must be conducted carefully, ensuring that the failure mechanism is the same as that observed under normal operating conditions [1]. Since the components are expected to remain functional for several hundreds or even thousands of hours, it is usually required to accelerate the tests performed in laboratories [2]. The category of tests related to the fatigue-life estimation of components operating in specific applications, aims to reproduce the entire fatigue damage experienced by the component during its operational life, but in a shorter amount of time. These tests are usually referenced as *fatigue-life tests* or *durability tests.* The use of tests tailored in accordance with the application and/or components to be analyzed (*Test Tailoring*) has been consolidated over the years [3,4]. The synthesis of signals based on the actual environmental conditions to which the components are subjected is generally referred to as *Mission Synthesis*, which more specifically aims to achieve the damage potential equivalence between the environmental conditions and synthesized signals. This is usually preferred to Standards that propose generic test procedures and are excessively strict in general (e.g. MIL STD 810F, GAM EG13). The vibrations measured in real-life applications are typically not replicated "as is" because their stochasticity would be lost. The specification is given in terms of a Power Spectral Density (PSD) to be used for the generation of a vibratory motion.

The shaker controller generates the physical motion through the application of the Inverse Fast Fourier Transform (*IFFT*) in combination with randomly selected phases [5,6]. The overall probability distribution of the input signal tends toward Gaussian, whereas distinctive peaks are often present in real-life random excitations (e.g. due to micro-collisions, road transportation [7,8], etc.), causing the probability distribution to be non-Gaussian. The statistical parameter known as kurtosis may be employed to quantify the feature of non-Gaussianity. Several methods have been proposed to control kurtosis (e.g. [9-25]), still maintaining the desired PSD profile, in order to synthesize more realistic signals.

The random excitations used in experimental tests, are generically ascribed to the field of vibration qualification testing. If the requirement to comply with a kurtosis value is added to the *PSD* specification, this type of vibration qualification testing is also referred to as *kurtosis control.* If the specification is given in terms of a target damage potential and duration, the resulting experimental tests belong to the category of durability tests, and the synthesized signals are generated through the Mission Synthesis procedure. If the target duration of durability tests is lower than the component's expected lifetime (as it is usually the case), these tests might also be referenced more specifically as *accelerated* durability tests (or fatigue-life tests, as already mentioned).

The study leading to this dissertation revolved around the search for novel Mission Synthesis methodologies aimed at the relatively unexplored field of non-Gaussian durability tests, possibly extending the work that had previously been conducted on kurtosis control. These tests not only have to comply with a prescribed damage potential and duration, but also with the preservation of non-Gaussian features (e.g. kurtosis) of signals measured from the applications. The main objective of this work is therefore to provide novel algorithms which may aid in the synthesis of non-Gaussian signals, to be used in (accelerated) durability tests. The provision of such novel algorithms will additionally be supported by a subsequent numerical and then experimental test procedure, in order

to highlight the most important aspects which may be "obscured" by the quite elaborate but necessary theory behind these algorithms.
In the remaining part of this introduction, an overview of the dissertation's structure is outlined; the bibliographical referencing of the technical topics already described in the literature is more thoroughly provided in the pertinent chapters and appendices.
Chapter 1 and section 1.1 aim to provide a thorough revision of the available references on kurtosis control in the literature, as well as provide a rigorous mathematical description about the ineffectiveness of some of the kurtosis control methods and how the bandwidth of the system plays a key role [26-32] in affecting the distribution of ergodic [33] signals. Despite the theory related to kurtosis control requires well-known concepts of signal processing, probability theory and stochastic processes, and despite the fact that the result is well-known, the theoretical presentation of section 1.1 is original and offers -to the author's knowledge- a novel perspective. The content of all the appendices is also original; to be more precise, the mathematical results presented in Appendices A-D are known, but originally adapted to the theory presented. On the other hand, Appendices E-H also present -to the author's knowledge- novel results.
In section 1.2, some of the algorithms available in the literature [10-17] to effectively control kurtosis in random vibration tests are revised and in chapter 2 and section 2.1 a technique to extend them to durability tests is discussed [34]. A proper procedure, which starts from reference signals (i.e. measured from real applications) and preserves both the accumulated fatigue damage and the signals' statistical characteristics, could potentially be more reliable than the standard approach; the development of such a procedure is also the main purpose of this work. In durability tests, the Fatigue Damage Spectrum (*FDS*) [35-40] is generally used to quantify the fatigue damage potential associated with the excitation. In Gaussian tests, this damage potential can be mathematically related to the *PSD* of the excitation; the complete mathematical description was provided by C. Lalanne et al. [36, 39-41]. The signal synthesized for accelerated fatigue-life tests must reproduce, in a short amount of time, the same *FDS* generated by the reference vibration throughout the component's expected lifetime. Despite the limited duration of the tests, one must proceed with caution in order to ensure that the decreased duration does not affect the failure mode; in fact, excessively short durations might lead to exceedingly high stress levels, possibly shifting the failure mode from a fatigue type of failure to a type of failure caused by exceeding the material's yield strength [42,43]. The synthesis procedures currently used generate Gaussian signals that may be unrealistic in representing the characteristics of the usually non-Gaussian reference data. In section 2.2, this dissertation presents novel algorithms for the synthesis of accelerated test profiles with prescribed *FDS* and a non-Gaussian distribution.
In addition, in Appendix F a novel procedure for the estimation of the damage is proposed. The standard estimation of the damage is usually obtained by adopting either the so-called time-domain or frequency-domain methods [44,45]. The former are valid for every type of load, whereas most of the latter have exact theoretical implementations only for Gaussian loads. However, the major downside of time-domain methods is usually the computational time required, whereas the frequency domain approach is generally much faster. Hence, in the literature several authors proposed novel frequency-domain methodologies on non-Gaussian signals as well [46-49]. However, the applicability of frequency-domain methods to non-Gaussian time-series is usually constrained by some factors such as: degree of non-stationarity of the time-series, statistical distribution of the time-series, natural frequencies of mechanical components. Therefore, a novel time-domain methodology is proposed in Appendix F to bridge the gap between time and frequency-domain, seeking to limit the computational effort and with a wider range of applicability than frequency domain methods.
In chapter 3, theoretical systems are modelled to test the novel algorithms numerically, whereas in chapter 4 an experimental campaign is conducted to test validity in actual experiments, with the aim to attach a practical value to the theoretical work presented. Chapter 3 and 4 comprise both accelerated and non-accelerated tests.

Finally, it is worth mentioning that the author's collaboration with industries (*Easting s.r.l.s.*) led to the development of Graphical User Interfaces that implement all the novel algorithms proposed, as well as the standard methodologies. Some of the relevant features of these interfaces are summarized in Appendix H.

1 Kurtosis control

In this chapter the theory of kurtosis control is described mathematically in the first part, where the mathematical formulae that relate kurtosis (and higher order moments) to the spectral phases and amplitudes of a vibratory signal are introduced. In section 1.1, the theory (which is worked out in detail in the Appendices A, B, C) is used to discuss the so-called Papoulis' Rule. In the rest of the chapter, starting from section 1.2, an overview of the current state-of-the-art kurtosis control algorithms is provided.

Given a random signal $x(t)$ in the time domain, its probability density $p(x)$ (assumed to be stationary for simplicity) and its average value c_0, the second and fourth order moments M_2 and M_4 can be defined as:

$$M_2 = \int_{-\infty}^{+\infty} (x - c_0)^2 p(x) dx = \sigma^2 \tag{1.1}$$

$$M_4 = \int_{-\infty}^{+\infty} (x - c_0)^4 p(x) dx \tag{1.2}$$

where σ^2 is called the variance and its square root σ is the standard deviation. If $c_0 = 0$, which is usually the case for signals measured from real applications, the signal root mean square (RMS) is equal to σ.
Kurtosis k is defined as:

$$k = \frac{M_4}{{M_2}^2} = \frac{M_4}{\sigma^4} \tag{1.3}$$

This parameter can be used to estimate the presence of high peaks in a signal: in fact, if $x(t)$ has high peaks and the latter's weight $p(x(t))$ is relevant, the terms $(x - c_0)^4 p(x)$ can be preponderant, hence increasing the kurtosis value.
For a Gaussian signal, the probability distribution has the form:

$$p(x) = \frac{1}{\sigma\sqrt{2\pi}} e^{-\frac{(x-c_0)^2}{2\sigma^2}} \tag{1.4}$$

If Eq.(1.4) is inserted into Eq.(1.1) moment M_2 gives σ^2, whereas if inserted into Eq.(1.2) moment M_4 gives $3\sigma^4$. Hence, for a Gaussian signal kurtosis is equal to 3.
Shaker controllers for random vibration testing can be based on the Fast Fourier Transform (FFT) data processing technique; the test specification is given in the frequency domain in terms of a power spectral density (PSD) and actual time histories are reconstructed from the prescribed PSD by the Inverse Fast Fourier Transform ($IFFT$). It means that the shaker is driven by a multi-frequency signal of the type:

$$x(t) = \frac{A_0}{2} + \sum_{n=1}^{N} A_n \cos(2\pi \cdot n \cdot \Delta f \cdot t + \varphi_n) \tag{1.5}$$

with a large number of harmonics N. The amplitudes of the harmonics are determined according to the given PSD shape $G(f)$ that is discretized with the frequency increment Δf:

$$A_n = \sqrt{2\,\Delta f\; G(n\Delta f)} \tag{1.6}$$

The phase angles φ_n are defined as uniformly distributed random numbers ranging from $-\pi$ to π (or 0 to 2π). The random generation of the harmonics phases provides the time signal with a Gaussian probability distribution.
In order to motivate that the signal is Gaussian, an expression for kurtosis could be used, which is derived in Appendix A (Eqs.(A.20, A.26)) from a more general formula. The following formula for kurtosis was derived by Steinwolf [14]:

$$\begin{aligned}
\mathrm{k} = 3 + \left(\frac{1}{4}\sum_{n}\sum_{k} {A_n}^2\,{A_k}^2\right)^{-1} \Bigg(& -\frac{3}{8}\sum_{n} {A_n}^4 \\
& + 3 \sum_{\substack{l+m=n+k \\ l<m,n<k,n<l}} A_n A_k A_l A_m \cos(\varphi_n + \varphi_k - \varphi_l - \varphi_m) + \\
& + 3 \sum_{n+k+l=m\; n<l<k} A_n A_k A_l A_m \cos(\varphi_n + \varphi_k + \varphi_l - \varphi_m) + \\
& + \frac{1}{2}\sum_{3k=m} {A_k}^3 A_m \cos(3\varphi_k - \varphi_m) + + \frac{3}{2}\sum_{\substack{2n+l=m \\ n\neq l}} {A_n}^2 A_l A_m \cos(2\varphi_n + \varphi_l - \varphi_m) + \\
& + \frac{3}{2}\sum_{\substack{n+k=2m \\ n<k}} A_n A_k {A_m}^2 \cos(\varphi_n + \varphi_k - 2\varphi_m) \Bigg)
\end{aligned} \tag{1.7}$$

The sums must be computed with all the indices ranging from 1 to N but only if the conditions under the summation symbols are verified.
From this expression a value of 3 emerges, plus other terms. If the phases are selected randomly and uniformly (i.e. with uniform probability distribution) the cosine functions will produce uniformly random values contained in the interval $[-1,1]$, thus the terms multiplied by the cosines will compensate each other making the value of k close to 3 so that the signal has a Gaussian probability distribution. To be more rigorous, kurtosis being equal to 3 might not be enough to assert that a signal is Gaussian; in fact this also depends on higher order moments. A more rigorous explanation is given in the next section.
By properly choosing the phases, it is evident that kurtosis may be manipulated (without affecting the *PSD*, which is only dependent upon the amplitudes): for instance, its maximum value can be reached when all the phase components are set to zero. Changing the kurtosis and preserving the *PSD* is known as kurtosis control. Kurtosis control by phase manipulation is a subject which will be dealt with in subsection 1.2.1; other techniques will be described in subsequent subsections.

1.1 Effectiveness of kurtosis control

Any kurtosis control algorithm aims to control the kurtosis value of a vibratory signal to be generated by the shaker; this is input kurtosis, while the device under test (*DUT*) will generally show a different value, because between the input and the output there is the transfer function of the system.

A. Papoulis [26] proved that if the transfer function of the system is that of a filter with a narrow band and some other technical assumptions are satisfied (mainly regarding the input signal features), the output tends to have a Gaussian distribution as the band goes to zero, regardless of the distribution of the input. This theorem is often referred to as Papoulis' rule [31,32], and it is important to stress that the validity of the statement depends on both the component's and the excitation signal's characteristics. Since the damping coefficient of mechanical systems is usually in the low percentage range, in this case the transfer function can usually be likened to that of a filter with a narrow band, therefore Papoulis' rule may hold and the output probability distribution could tend towards a Gaussian distribution. It may therefore be not easy, in general, to transfer the same amount of kurtosis from the input to the output, because kurtosis usually decreases in the output[2].
Since the physical intuition may be hidden by the mathematical details contained in Papoulis' derivation, a different explanation will be given in the following as to why the filtering process may lead towards Gaussianity. This is important in order to understand why some kurtosis control algorithms are effective and others are not.
The q[th] moment M_q of a time-series (be it the input or the output of a system) can be written in the following form in terms of its amplitudes and phases (see Appendix A):

$$M_q = \sum_{\substack{n_1+n_2+\cdots+n_q=0 \\ n_1\neq 0, n_2\neq 0, \ldots, n_q\neq 0}} \frac{1}{2^q} A_{n_1} A_{n_2} \ldots A_{n_q} \cos\left(\varphi_{n_1} + \varphi_{n_2} + \cdots + \varphi_{n_q}\right) \tag{1.8}$$

where the generic index n_k can assume the integer values from $-N$ to N with 0 excluded.
The central moments of zeroth and first order are trivially equal to 1 and 0 respectively[3], whereas that of second order corresponds to the variance of the signal:

$$M_2 = \sum_{\substack{n_1+n_2=0 \\ n_1\neq 0, n_2\neq 0}} \frac{1}{4} A_{n_1} A_{n_2} \cos\left(\varphi_{n_1} + \varphi_{n_2}\right) = \sum_{n_1\neq 0} \frac{1}{4} A_{n_1} A_{-n_1} \cos\left(\varphi_{n_1} + \varphi_{-n_1}\right) =$$

$$= \sum_{n_1\neq 0} \frac{1}{4} \left(A_{n_1}\right)^2 \cos\left(\varphi_{n_1} - \varphi_{n_1}\right) = \sum_{n\neq 0} \frac{1}{4} {A_n}^2 = \sum_{n>0} \frac{1}{2} {A_n}^2 \tag{1.9}$$

Under the narrowband assumption, it is possible to understand how the general q[th] moment of the system's output is affected. In the following, it is assumed that the system behaves as a filter with a bandwidth Δf_0, which is narrow enough for the amplitudes of the response to be assumed approximately constant over the frequencies contained in that bandwidth. Another assumption will be that the number of signal's harmonics remains "large" after filtering, that is $\frac{1}{T} \ll \Delta f_0$ for a signal of duration T, with the phases being uniformly random in the interval $[0,2\pi]$ over the filtered bandwidth. Alternatively, the following considerations remain valid for the system's input with a sufficiently large number of dominant harmonics and uniform random phases.

For even values of q, the moment M_q can contain both terms depending on the phases and terms which do not, depending therefore only on the amplitudes (i.e. when the phase terms inside the cosine of Eq.(1.8) cancel, and the cosine becomes equal to 1). Due to the indistinguishability of the indices

[2] However, it is noteworthy to point out that, for non-stationary signals, output kurtosis could still be higher than input kurtosis (see subsection 1.2.3). It is more of a "rule of thumb" than an accurate expression to say that output kurtosis is usually lower than input kurtosis because it is not always true.
[3] The first order central moment is assumed equal to 0 because vibration signals usually have zero mean.

$n_1, n_2, \dots, n_q$ in Eq.(1.8) (e.g. if n_1 is replaced by n_2 and vice versa, the result would not be affected), the functional form of M_q could also be expressed as:

$$M_q = C_{2q}\left(\sum_{n\neq 0}\frac{1}{4}{A_n}^2\right)^{\frac{q}{2}} + C_{4q}\left(\sum_{n\neq 0}{A_n}^4\right)^{\frac{q}{4}} + C_{6q}\left(\sum_{n\neq 0}{A_n}^6\right)^{\frac{q}{6}} + \cdots + C_{qq}\left(\sum_{n\neq 0}{A_n}^q\right)^{1} +$$
$$+C_{2,4,q}\left(\sum_{n\neq 0}{A_n}^2\right)^{\frac{j_1}{2}}\left(\sum_{n\neq 0}{A_n}^4\right)^{\frac{q-j_1}{4}} + C_{4,6,q}\left(\sum_{n\neq 0}{A_n}^4\right)^{\frac{i_1}{4}}\left(\sum_{n\neq 0}{A_n}^6\right)^{\frac{q-i_1}{6}} + \cdots +$$
$$+C_{2,q-2,q}\left(\sum_{n\neq 0}{A_n}^2\right)\left(\sum_{n\neq 0}{A_n}^{q-2}\right) + C_{4,q-4,q}\left(\sum_{n\neq 0}{A_n}^4\right)\left(\sum_{n\neq 0}{A_n}^{q-4}\right) + \cdots +$$
$$+C_{2,4,6,q}\left(\sum_{n\neq 0}{A_n}^2\right)^{\frac{u_1}{2}}\left(\sum_{n\neq 0}{A_n}^4\right)^{\frac{u_2}{4}}\left(\sum_{n\neq 0}{A_n}^6\right)^{\frac{q-u_1-u_2}{6}} + \cdots +$$
$$+f_q(A_1, A_2, \dots, A_N, \varphi_1, \varphi_2, \dots, \varphi_N) \qquad (1.10)$$

where the terms raised to the powers of: $\frac{q}{2}, \frac{q}{4}, \frac{q}{6}, \dots, \frac{j_1}{2}, \frac{i_1}{4}, \frac{q-j_1}{4}, \frac{q-i_1}{6}, \dots, \frac{u_1}{2}, \frac{u_2}{4}, \frac{q-u_1-u_2}{6}, \dots$, etc. may appear only if the latter are integers. Eq.(1.10) needs further clarification: a simple example can be given to motivate the seemingly complicated expression. If the term, say, ${A_3}^2{A_7}^{q-2}$ appears in M_q (multiplied by some constant, say, $\hat{C}$), then also ${A_7}^2{A_3}^{q-2}$ must appear (multiplied by the same constant) due to the symmetry of the indices. This must be generalized to the other indices as well, not just for 3 and 7 chosen in the example. Therefore, if ${A_3}^2{A_7}^{q-2}$ appears, it can be grouped for example in the term: $\left(\sum_{n\neq 0}{A_n}^2\right)\left(\sum_{n\neq 0}{A_n}^{q-2}\right)$. Of course, ${A_3}^2{A_7}^{q-2}$ could also appear in other terms, such as $\left(\sum_{n\neq 0}{A_n}^2\right)^{q/2}$; it is up to the multiplicative constants in Eq.(1.10) to add up to the right constant (i.e. the constants $C_{2q}, C_{2,q-2,q}$ and possibly others are related to $\hat{C}$). It is more convenient for further considerations to group together some terms of Eq.(1.10) more formally (and also relabel the constants differently), so that the equation could be rewritten in the following form:

$$M_q = C_{2q}\left(\sum_{n\neq 0}\frac{1}{4}{A_n}^2\right)^{\frac{q}{2}} - \sum_{\substack{0<\sum_{k=2}^{q/2}2k\cdot j_{2k}\leq q \\ j_{2k}\in\mathbb{N},\ k=2,3,\dots,q/2}} C_{j_4,j_6,j_8,\dots,j_q}\left(\sum_{n\neq 0}{A_n}^2\right)^{\frac{q}{2}}\prod_{k=2}^{q/2}\left(\frac{\sum_{n\neq 0}{A_n}^{2k}}{\left(\sum_{n\neq 0}{A_n}^2\right)^k}\right)^{j_{2k}} +$$
$$+f_q(A_1, A_2, \dots, A_N, \varphi_1, \varphi_2, \dots, \varphi_N) \qquad (1.11)$$

The term C_{2q} is obtained by dividing the q-tuple of phases $\varphi_{n_1}, \varphi_{n_2}, \dots, \varphi_{n_q}$ in subsets of $q/2$ disjoint pairs and counting all possible arrangements of those $q/2$ pairs having opposite indices (thus making the cosine of Eq.(1.8) equal to 1); this number of arrangements is equal to C_{2q} by definition. By doing so there are some terms that are over-counted, that is when the absolute value of the indices of different pairs is the same. In fact, for example, with $q = 4$ and indices $n_1 = 5, n_2 = -5, n_3 = -5, n_4 = 5$, it is clear that this combination should be counted only once, but by counting all possible arrangements n_1 could be paired with both n_2 (i.e. n_3 paired with n_4) and n_3 (i.e. n_2 paired with n_4), therefore C_{2q} actually counts this combination of indices twice. Hence, the coefficients $C_{j_4,j_6,j_8,\dots,j_q}$ act as a correction to avoid multiple counting (this is why a minus sign was put before the summation

symbol); for instance when $q = 4$ the only contribution is given by $j_4 = 1$, and the only coefficient C_1 is multiplied by $\sum_{n\neq 0} {A_n}^4 = 2\sum_{n>0} {A_n}^4$. Then, by comparing Eq.(1.11) when $q = 4$ with Eq.(A.26) or Eq.(1.7), one finds that the value of C_1 is $3/16$. If $q = 6$, then the second term in Eq.(1.11) gives: $C_{1,0}\left(\sum_{n\neq 0} {A_n}^4\right)\left(\sum_{n\neq 0} {A_n}^2\right) + C_{0,1}\left(\sum_{n\neq 0} {A_n}^6\right)$, and so on. Therefore, it should be clear how simple symmetry arguments about the indices may lead to the general formula for M_q written as in Eq.(1.11). The function $f_q(A_1, A_2, \dots, A_N, \varphi_1, \varphi_2, \dots, \varphi_N)$ depends on both amplitudes and phases because it considers all other possibilities, namely terms containing q-tuples for which at least one of the phase indices does not sum to zero with any of the other phase indices (the algebraic sum of *all* indices still equals zero). In this case the cosines of Eq.(1.8) will not equal 1 in general. However, due to the narrowband of the filter, and to the (i) assumed uniform randomness of the phases, (ii) small variation of the amplitudes and (iii) large number of harmonics $\left(\text{i.e. } \frac{1}{T} \ll \Delta f_0\right)$:

$$f_q(A_1, A_2, \dots, A_N, \varphi_1, \varphi_2, \dots, \varphi_N) \approx 0 \tag{1.12}$$

Besides, the term that multiplies the coefficient C_{2q} is large with respect to all others, in fact, by using the letter $\mathcal{O}$ to denote the big O notation, one can write:

$$\left(\sum_{n\neq 0} {A_n}^2\right)^k = \mathcal{O}\left({A_n}^{2k} N^k\right) \gg \mathcal{O}\left({A_n}^{2k} N\right) =$$

$$= \sum_{n\neq 0} {A_n}^{2k} \qquad \text{where} \quad k \geq 2 \text{ as in } Eq.(1.11) \tag{1.13}$$

Therefore, the term $\frac{\sum_{n\neq 0} {A_n}^{2k}}{\left(\sum_{n\neq 0} {A_n}^2\right)^k}$ goes to zero as N goes to infinity.

Hence, the error is negligible if only the first term is considered:

$$M_q = C_{2q}\left(\sum_{n\neq 0} \frac{1}{4} {A_n}^2\right)^{\frac{q}{2}} \qquad \text{where} \quad q = 2,4,6, \dots \tag{1.14}$$

This agrees with the fact that terms that are counted multiple times in the first term of Eq.(1.11), which appear when the absolute value of the indices of different pairs is the same, are much less than the number of possibilities where the indices of disjoint pairs are different.

According to the above considerations, the value of the coefficient C_{2q} can be computed by counting the number of q-tuples of indices $n_1, n_2, \dots, n_q$ among which pairs of them have opposite value (neglecting over-counting). If n_1 is fixed, there are $q - 1$ possible indices $\left(\text{i.e. } n_2, \dots, n_q\right)$ to which n_1 can be equal in absolute value and have opposite sign. Assuming that a second index is chosen such that it equals $-n_1$, a third index must be fixed. At this point there are $q - 3$ possible indices which the third index can be opposite to. By continuing this line of thought it is clear that the coefficient C_{2q} can be obtained according to the formula:

$$C_{2q} = (q-1)(q-3)(q-5) \dots 3 \cdot 1 = (q-1)!! \tag{1.15}$$

where the notation $(q-1)!!$ indicates the double factorial. Hence, Eq.(1.14) can be recast as:

$$M_q = (q-1)!! \, {M_2}^{\frac{q}{2}} \qquad \text{where} \quad q = 2,4,6, \dots \tag{1.16}$$

For odd values of q, it is clear that the moment M_q can contain terms depending only on the phases, because there is always at least one phase that remains unmatched; therefore it can be written in the following form:

$$M_q = g_q(A_1, A_2, \dots, A_N, \varphi_1, \varphi_2, \dots, \varphi_N) \tag{1.17}$$

The function g_q is conceptually the same as the function f_q considered for even values of q, thus it is approximately zero under the assumptions stated above:

$$M_q = 0 \qquad \text{where} \quad q = 1,3,5,\dots \tag{1.18}$$

As is well-known [33], if the signal is ergodic the moments computed in the time-domain (Appendix A, Eq.(A.18)) are equal to their ensemble average counterparts; therefore, Eq.(1.16) and Eq.(1.18), which represent moments calculated in the time-domain, may be assumed equal to the corresponding moments obtained from the statistical distribution. From all the moments, the probability density function $p(x)$ can be derived; in fact, by considering the definition of the central moment in terms of ensemble averages:

$$M_q = \int_{-\infty}^{+\infty} (x - c_0)^q p(x) dx \tag{1.19}$$

it is easy to see that:

$$\sum_{q=0}^{\infty} (-j\omega)^q \frac{M_q}{q!} = \int_{-\infty}^{+\infty} e^{-j\omega(x-c_0)} p(x) dx \tag{1.20}$$

where j is the imaginary unit and it is assumed that the series and the integral converge, by omitting any mathematical rigor.
The left side of Eq. (1.20) represents the Fourier Transform of the function $p(x)e^{j\omega c_0}$, thus the Inverse Transform can be used to calculate $p(x)$ from its moments:

$$p(x) = \frac{1}{2\pi} \int_{-\infty}^{+\infty} \sum_{q=0}^{\infty} (-j\omega)^q \frac{M_q}{q!} e^{j\omega(x-c_0)} d\omega \tag{1.21}$$

By substituting the expressions given by Eq.(1.16) and Eq.(1.18), Eq.(1.21) yields the Gaussian probability density function (see Appendix B).
Another interesting case to consider is when the narrowband filter has a bandwidth Δf_0 such that $\Delta f_0 < \frac{1}{T}$, and it is assumed that the response behaves like a sinusoid after filtering, such that there remains only one harmonic. In this case in Eq.(1.8), which still remains valid, the indices of the phases and amplitudes can only assume the values of $\pm l$ (since there is only one sinusoid), where l is a fixed integer. Since the sum of the indices $n_1, n_2, \dots, n_q$ must equal zero, it is easy to see the moment of order q is zero if q is odd:

$$M_q = 0 \qquad \text{where} \quad q = 1,3,5,\dots \tag{1.22}$$

because the condition under the summation symbol in Eq.(1.8) is not satisfiable. It is also straightforward to compute the moment of order q when q is even. In fact, since the indices can only assume the values $\pm l$, $q/2$ should be equal to l and the other $q/2$ equal to $-l$. The number of choices to achieve that is given by the binomial coefficient $\binom{q}{q/2}$, hence:

$$M_q = \binom{q}{q/2}\frac{A^q}{2^q} \qquad \text{where} \quad q = 2,4,6,\ldots \qquad (1.23)$$

where A is the amplitude of the sinusoid.
By substituting the expressions given by Eq.(1.22) and Eq.(1.23), Eq.(1.21) yields the probability density function of a sinusoid (see Appendix C).
The case of the filter bandwidth being so small such that only one sinusoid is extracted is not really likely in practice; nevertheless, the examples given in this section emphasize that the bandwidth of a system plays an important role in determining the distribution of the response of the system.

1.2 Kurtosis control algorithms

There are different types of kurtosis-control algorithms: phase manipulation [14,16,20], amplitude modulation [17-19], Polynomial Transformation [21-23]; another more recent type of algorithm [17] describes how to synthesize novel non-stationary signals with prescribed kurtosis and *PSD*. In the next subsections, most of the focus will be directed to the kurtosis-control algorithms presented by E. Pesaresi et al. in recent works [17], which span most of the different types of kurtosis-control algorithms available in the literature. Some of the algorithms proposed therein are novel and not negatively affected by Papoulis' Rule, as shown by means of a proper selection of input parameters. The algorithms are revised starting with the phase manipulation method as described by A. Steinwolf et al. [14] and then describing those introduced by E. Pesaresi et al. [17], with the aim to highlight the different characteristics in the synthesized signals.

1.2.1 Phase manipulation

By looking at one of the expressions for M_4 given by Eqs.(A.21, A.23, A.26) in Appendix A, it is evident that M_4 depends not only on the PSD, which is considered assigned (i.e. the amplitudes of the harmonics are fixed), but on the phases as well. Two approaches adopted in the literature are summarized in the following:

1) Some phases are chosen so that the arguments of some cosines in M_4 are equal to zero [14,24]. To exemplify and understand this approach, if Eq.(A.21) is considered, that is: $\mathrm{M}_4 = \frac{1}{16}\sum_{\substack{n+k+l+m=0 \\ n\neq 0,k\neq 0,l\neq 0,m\neq 0}} A_n A_k A_l A_m \cos(\varphi_n + \varphi_k + \varphi_l + \varphi_m)$, this expression has four different indices n, k, l, m (such that $n + k + l + m = 0$) associated with each term $A_n A_k A_l A_m \cos(\varphi_n + \varphi_k + \varphi_l + \varphi_m)$; for instance, if a new φ_n is chosen so that $\varphi_n = -(\varphi_k + \varphi_l + \varphi_m)$ for three selected indices k, l, m (considered to be fixed), the term $A_n A_k A_l A_m \cos(\varphi_n + \varphi_k + \varphi_l + \varphi_m)$ becomes equal to $A_n A_k A_l A_m$ and thus it is maximized.
This process can be carried out for other quartets of indices to maximize other terms.
If, instead of maximizing those terms it is required to minimize them, the same process can be carried out but, the argument of the cosine in this case will be set to $\pm\pi$ instead of 0.
Maximizing or minimizing those terms is useful for those cases where kurtosis needs to be, respectively, increased or decreased. Usually, phases are randomly generated at first, thus the signal starts (approximately) with the Gaussian value of 3 for kurtosis and then phase manipulation is used to increase (by maximizing the above terms) or decrease (by minimizing the above terms) the kurtosis parameter.
This procedure is not flawless: in fact, if for instance kurtosis needs to be increased and it is decided to maximize one term associated with a certain quartet of indices, it is not granted that the other terms grow as well or remain constant. Indeed, since the terms are numerous, there will be terms which

likely become negative, with a possible overall effect of kurtosis decrease instead of increase. Thus, the process is not optimal, because in order to obtain the kurtosis target value several iterations should be carried out.

2) The second approach [14] was conceived to improve the first one. It considers M_4 in terms of the a_n, b_n terms, defined in Appendix A:

$$M_4 = 3{M_2}^2 - \frac{3}{8}\sum_n {A_n}^4 +$$

$$3\sum_{\substack{j+k=n+m \\ j<k,n<m,n<j}} \{(a_j a_k - b_j b_k)(a_n a_m - b_n b_m) + (a_j b_k + a_k b_j)(a_n b_m + a_m b_n)\} +$$

$$3\sum_{\substack{j+k+n=m \\ j<k<n}} \{(a_j a_k - b_j b_k)(a_n a_m + b_n b_m) + (a_j b_k + a_k b_j)(a_n b_m - a_m b_n)\}$$

$$+\frac{1}{2}\sum_{j=3k} \{a_j a_k({a_k}^2 - 3{b_k}^2) - b_j b_k({b_k}^2 - 3{a_k}^2)\}$$

$$+\frac{3}{2}\sum_{\substack{j=k+2n \\ k\neq n}} \{(a_j a_k + b_j b_k)({a_n}^2 - {b_n}^2) - 2(a_j b_k - a_k b_j)a_n b_n\}$$

$$+\frac{3}{2}\sum_{\substack{j+k=2n \\ j<k}} \{(a_j a_k - b_j b_k)({a_n}^2 - {b_n}^2) + 2(a_j b_k + a_k b_j)a_n b_n\} \qquad (1.24)$$

Considering the first summation of Eq.(1.24):

$$\sum_{\substack{j+k=n+m \\ j<k,n<m,n<j}} \{(a_j a_k - b_j b_k)(a_n a_m - b_n b_m) + (a_j b_k + a_k b_j)(a_n b_m + a_m b_n)\}$$

each member contained in the curly brackets still has its maximum value equal to $A_j A_k A_n A_m$ because the formula derives directly from Eq.(1.7), knowing that: $a_n = A_n \cos\varphi_n, b_n = -A_n \sin\varphi_n$.
This maximum value is the target and it should be reached by keeping the PSD fixed, as already mentioned. It can be achieved if, for each of the harmonics involved, the a_n terms are expressed as a function of b_n (or vice versa):

$$a_j = \pm\sqrt{{A_j}^2 - {b_j}^2}, a_k = \pm\sqrt{{A_k}^2 - {b_k}^2}, a_n = \pm\sqrt{{A_n}^2 - {b_n}^2}, a_m = \pm\sqrt{{A_m}^2 - {b_m}^2}$$

Thus, for a fixed quartet of indices j, k, m, n, there are only 4 independent parameters for each term in the first summation of Eq.(1.24).
The procedure of this second approach requires that a quartet of indices be chosen, for instance: j, k, m, n belonging to the first summation of Eq.(1.24), and then one index be chosen for which the phase should vary (for instance k) and the phases of the other 3 indices be considered fixed (j, m, n). A mandatory condition to be satisfied is that the three fixed indices not be equal to the index for which the phase should vary (for the first summation this is always true).

Then, one can rewrite the term with indices j, k, m, n in the first summation as:

$$f(b_k) = Db_k + Ea_k = Db_k \pm E\sqrt{{A_k}^2 - {b_k}^2} \tag{1.25}$$

where:

$$D = a_j(a_n b_m + a_m b_n) - b_j(a_n a_m - b_n b_m)$$

and:

$$E = a_j(a_n a_m - b_n b_m) + b_j(a_n b_m + a_m b_n)$$

After differentiating the function given by Eq.(1.25) with respect to b_k and imposing the result to be equal to zero, the following solution can be found for b_k:

$$b_k = \pm A_k\sqrt{D^2/(D^2 + E^2)} \tag{1.26}$$

Then a_k can be calculated as already seen:

$$a_k = \pm\sqrt{{A_k}^2 - {b_k}^2} \tag{1.27}$$

With the double sign in Eq.(1.26) and another double sign in Eq.(1.27), there are 4 solutions, but only two of these solutions lead to the maximum and minimum of the function in Eq.(1.25). To find the signs for the b_k and a_k values corresponding to the maximum and minimum, the signs of D and E must be considered: for kurtosis increase, the sign of b_k should be selected to be the same as the sign of D and the sign of a_k the same as the sign of E. Then, the value of $f(b_k)$ will be maximum. For kurtosis decrease, the sign of b_k should be selected to be the opposite to the sign of D and the sign of a_k opposite to the sign of E. Then, the value of $f(b_k)$ will be minimum.
This is the procedure described by A. Steinwolf in his article [14]. If only one term[4] of the first summation of Eq.(1.24) is considered, the first and second approach lead to the same result but, if more terms are considered, the second approach leads to better results, because more sums are taken into consideration. Their maximum or minimum value is to be found by optimizing the function: $f(b_k) = D'b_k + E'a_k = D'b_k \pm E'\sqrt{{A_k}^2 - {b_k}^2}$, where D' and E' are constant with respect to b_k like D and E, but may depend in general on more than 3 indices[5] (i.e. the case if only one term is considered).
However, even the second approach is not flawless: indeed it cannot consider all the possible terms to be added in Eq.(1.24), because when the index k is chosen, the other indices must not be equal to k, otherwise the problem could not be written in the form: $f(b_k) = D'b_k + E'a_k = D'b_k \pm E'\sqrt{{A_k}^2 - {b_k}^2}$ because higher order terms would appear. Therefore, maximizing only some of the

[4]What is meant by "term" is the content of the curly brackets of the first summation appearing in Eq.1.24 (for a fixed quartet of indices j, k, m, n), namely: $(a_j a_k - b_j b_k)(a_n a_m - b_n b_m) + (a_j b_k + a_k b_j)(a_n b_m + a_m b_n)$.
[5] The expressions for D' and E' can be generalized from that of D and E. In particular, when one considers all possible indices, obtains:
$D' = \sum_{\substack{j+k=n+m \\ j<k,n<m,n<j \\ (k\ fixed)}} a_j(a_n b_m + a_m b_n) - b_j(a_n a_m - b_n b_m)$, $E' = \sum_{\substack{j+k=n+m \\ j<k,n<m,n<j \\ (k\ fixed)}} a_j(a_n a_m - b_n b_m) + b_j(a_n b_m + a_m b_n)$

terms does not prevent the others from having the opposite tendency, namely to create an overall effect that may thwart the desired one.

3) To conclude this subsection, a third approach of manipulating phases is introduced, which has a straightforward implementation; hereinafter it will be referred to as *PM* algorithm. The approach is not analytical and is based on the following steps:

step 0) generate phases randomly;

step 1) select one of the phases randomly in a pre-selected frequency range;

step 2) randomly set another value for that phase, between 0 and 2π;

step 3) calculate the new kurtosis value in the time domain[6];

step 4) if the new kurtosis value is closer to the target value, keep the value of the phase changed at step 2, otherwise discard it and restore the former value for that phase;

step 5) repeat from step 1 until the target is reached.

The speed of the *PM* algorithm is given by the fact that there is no analytical formula to compute. At step 1 of each loop, there is a 50% chance of increasing/decreasing kurtosis and only the operation of random number generation is needed, which is of no particular computational concern. Since the first two approaches described above usually consider only few of the terms contained in M_4 in the maximization process, the probability may be less than 50% at each loop, with possibly no advantage over the simple steps proposed above. In order to maximize the probability of increasing/decreasing kurtosis as desired, the second approach should consider a number of terms of the order $\mathcal{O}(N^2)$ at each loop, where N is the same number of harmonics as in Eq.(A.8). In fact, by considering Eq.(A.21) for the calculation of M_4, there are 4 indices and one constraint, hence $\mathcal{O}(N^3)$ operations; the number of operations to be done in the first sum of Eq.(1.24) is still of the order $\mathcal{O}(N^3)$. At each loop, the second approach fixes one of the indices, therefore there remain two free indices and $\mathcal{O}(N^2)$ operations. In this case, the coefficients D' and E' (see footnote 5) need a number of operations $\mathcal{O}(N^2)$ to be computed at each loop, which is much greater than the number of operations $\mathcal{O}(N)$ required for the computation of the kurtosis parameter (computed on step 3 in the *PM* method), with the M_k moment being defined in the discrete case as:

$$\mathrm{M}_k = \frac{1}{N_s}\sum_{l=0}^{N_s-1}(x(l\Delta t) - c_0)^k \tag{1.28}$$

[6] At step 3, it is necessary to perform an *IFFT* in order to generate the time-series.

where:

$$c_0 = \frac{1}{N_s}\sum_{l=0}^{N_s-1} x(l\Delta t) \tag{1.29}$$

$$N_s = 2(N-1) \tag{1.30}$$

It is also true that, on step 3 of the *PM* method, an *IFFT* is required to go from the frequency domain of the phases back to the time domain, before performing the kurtosis computation. Therefore, the number of operations $\mathcal{O}(N\log(N))$, which is distinctive of the *IFFT* implementation, must be added to the number $\mathcal{O}(N)$ related to the kurtosis computation in the time domain, but the total number still remains much smaller than $\mathcal{O}(N^2)$. This implies that, after one loop of the second phase manipulation approach proposed by A. Steinwolf and described in this subsection, a large number of steps is performed by the *PM* method. If this number is denoted by M, the probability of having the desired kurtosis increase/decrease in the *PM* method, increases from 50% to: $\sum_{i=1}^{M}\left(\frac{1}{2}\right)^i = \frac{2^M-1}{2^M} \approx 1$, namely close to 100% for even moderate values of *M*.

1.2.2 Modulation technique

Another technique to achieve kurtosis control is known as modulation. This approach consists in modulating a Gaussian signal $x(t)$ having the desired PSD spectrum with an appropriate function $w(t)$ such that: $y(t) = w(t)x(t)$ in order to obtain a Leptokurtic signal with a desired kurtosis value [17-19]. This method is effective in transferring the kurtosis value to the response of the *DUT* if the signal bursts created by the modulation have greater duration than the inverse of the bandwidth of the lightly damped system [18]. The carrier waveform $w(t)$ introduces low frequency components in the spectrum of $y(t)$ compared to that of $x(t)$, albeit negligible if $w(t)$ is properly designed.
The technique reported here was described by E. Pesaresi et al. [17]. The modulation algorithm therein was named "Multi-Level Variance" (MLV); it considers the signal to be synthesized as divided into n_b blocks of the same duration T_b (with no overlap). The generated blocks have different standard deviation, which represents the modulation procedure, with the modulating function $w(t)$ being of the form:

$$w(t) = \begin{cases} \frac{\sigma_1}{\sigma_{tot}}\ , & 0 \le t < T_b \\ \vdots & \\ \frac{\sigma_i}{\sigma_{tot}}\ , & (i-1)\cdot T_b \le t < i\cdot T_b \\ \vdots & \\ \frac{\sigma_n}{\sigma_{tot}}\ , & (n-1)\cdot T_b \le t < n\cdot T_b = T \end{cases}$$

The different levels of variance ${\sigma_i}^2$ $(i = 1, \dots, n_b)$ are produced in such a way that the synthesized signal is compliant with the kurtosis and PSD constraints as it will be shown in the following. In general, the PSD of a signal is computed by calculating the *FFT* over small-sized blocks, squaring their magnitude in order to obtain the so-called periodograms and then averaging the periodograms. More specifically, the periodogram could be thought of as some sort of PSD computed only for the generic block of the signal. Therefore, instead of using the word "periodogram", reference will be made hereinafter to the PSD of the blocks of the signal.

In the algorithm, the *PSD* $\boldsymbol{G_i}$ of the i^{th} block of the signal is set to be scaled with respect to the *PSD* $\boldsymbol{G}$ of the reference signal:

$$\boldsymbol{G_i} = \frac{{\sigma_i}^2}{{\sigma_{tot}}^2}\boldsymbol{G}, \qquad i = 1, \dots, n_b \tag{1.31}$$

In Eq.(1.31) σ_{tot} is the standard deviation of the overall signal, whereas σ_i is the standard deviation of the i^{th} block. It is to be highlighted that the σ_i parameters are the unknowns, whereas ${\sigma_{tot}}^2$ can be calculated from either the reference signal using Eq.(1.28) with $k = 2$ or from the reference *PSD* using the equation:

$${\sigma_{tot}}^2 = \int_0^\infty G(f)df \tag{1.32}$$

where $G(f)$ is the *PSD* of a continuous reference signal. However, since the processed signal is discrete in practice, the *PSD* is also discrete and the theoretical computation of Eq.(1.32) must be discretized.

The unknown parameters σ_i are also related to the overall variance ${\sigma_{tot}}^2$ via the relation (see Appendix D):

$${\sigma_{tot}}^2 = \frac{1}{n_b}\sum_{i=1}^{n_b} {\sigma_i}^2 \tag{1.33}$$

From Eqs.(1.31) and (1.33) the following relation must hold:

$$\boldsymbol{G} = \frac{1}{n_b}\sum_{i=1}^{n_b} \boldsymbol{G_i} \tag{1.34}$$

Since the *PSD* $\boldsymbol{G}$ is computed by averaging the *PSD* of the blocks, Eq.(1.34) is automatically satisfied (or *approximately* satisfied in case of a computation of the *PSD* with overlap of the blocks). Hence, the constraint on the *PSD* spectrum is respected if n_b coefficients σ_i ($\sigma_i > 0$) that comply with Eq.(1.33) are found.

In addition to Eqs.(1.33) and (1.34), another relation must hold between the kurtosis values of the overall signal k_{tot} and the kurtosis values of the single blocks k_i (see Appendix D):

$$k_{tot} = \frac{\sum_{i=1}^{n_b} k_i \cdot {\sigma_i}^4}{n_b \cdot {\sigma_{tot}}^4} \tag{1.35}$$

Eq.(1.35) will be used in one of the steps of the algorithm; the first step is to randomly generate the σ_i values such that $\sigma_i \in [\sigma_{min}, \sigma_{max}]$ and $\sigma_{min} < \sigma_{tot} < \sigma_{max}$. The ratio $r_\sigma = \frac{\sigma_{min}}{\sigma_{tot}} \in]0,1[$ must be set by the user, it being an input for the algorithm: the closer to 0 the more the variance of the synthesized signal will vary in time, whereas the opposite is true if closer to 1. The parameter σ_{max} is not selectable by the user because it is adjusted throughout the algorithm iterations in order to approach the target kurtosis within a certain tolerance; in particular, σ_{max} starts from an empirically set threshold higher than σ_{tot} and then is decreased at every loop until the algorithm converges. The threshold remains the same for every run of the algorithm; it should be neither too high, otherwise Eq.(1.33) may not be satisfied, nor too low because otherwise the target kurtosis value may not be reached. Besides, not only the value of σ_{max} may affect the speed of convergence of the algorithm, but its variation step at each loop may as well; the choice of the authors was guided by some trial and error runs of the algorithm and its non-uniqueness makes it difficult to give more rigorous details.

The user can also choose the parameter $n_p = 0,1, \dots, n_b$ intended to set the number of "bursts" of high amplitude excursion of the synthesized signal. The algorithm generates n_p blocks with a standard deviation equal to σ_{max}, which is greater than that of the other blocks.

The kurtosis k_i of the blocks may be calculated via the moments of Eq.(1.28) for greater accuracy, but it should be noted that the kurtosis values of the blocks are expected to be close to the value of 3, because the time-series associated with each block is (approximately) Gaussian. The overall discrete

signal x_n is obtained by performing the *IFFT* on each of the blocks' *PSD* spectra with randomly generated phases; then, the blocks are concatenated.
At an initial step of the procedure, a random integer s representing a single block is automatically generated in the interval $[1, n_b]$.
After the σ_i levels are generated ($i = 1, \dots, n_b, i \neq s$), the standard deviation and kurtosis of the randomly selected s^{th} block are calculated via the following relations, which stem from Eqs.(1.33) and (1.35):

$$\sigma_s = \sqrt{n_b {\sigma_{tot}}^2 - \sum_{\substack{i=1 \\ i \neq s}}^{n_b} {\sigma_i}^2} \tag{1.36}$$

$$k_s = \frac{n_b k_{tot} {\sigma_{tot}}^4 - \sum_{\substack{i=1 \\ i \neq s}}^{n_b} k_i {\sigma_i}^4}{{\sigma_s}^4} \tag{1.37}$$

Eqs.(1.36) and (1.37) are used in order to verify whether the prescribed *PSD* and target kurtosis can be achieved: indeed σ_s is required to be greater than zero and k_s greater than a lower threshold (the lower theoretical limit of kurtosis being 1) and less than an upper threshold. The upper threshold should not be set excessively high, possibly leading to the undesired effect to generate unrealistic peaks in the s^{th} block exceeding by far the amplitude of the peaks in the other blocks. Afterwards, in order to obtain the desired k_s given by Eq.(1.37), some harmonics phases of the s^{th} block are adjusted by means of a phase manipulation procedure. After few iterations, where the parameter σ_{max} is changed in order to converge towards the target kurtosis value, Eqs.(1.36) and (1.37) are usually satisfied.
The final step of the algorithm is to smooth the signal at the edges of the blocks (by means of special windows), in order to avoid unrealistic discontinuities among them.
In conclusion, the user has to insert:

- the reference input signal or, alternatively, reference *PSD* and kurtosis value;
- the parameter T_b;
- the ratio r_σ;
- the number of bursts n_p;
- the duration T of the signal to be synthesized;
- the sampling frequency of the synthesized signal (usually the same as the reference signal, therefore not necessarily an input).

1.2.3 Variable spectral density

A novel algorithm that does not fall under any category of kurtosis control algorithms thoroughly discussed in the literature (e.g. phase selection [14,16,20], modulation [17-19], Polynomial Transformation [21-23]), was described by E. Pesaresi et al. [17] and named "Variable Spectral Density" (*VSD*). It splits the signal to be synthesized into n_b disjoint blocks of the same duration T_b, as the algorithm discussed in subsection 1.2.2. The major difference is that the *PSD* $\boldsymbol{G_i}$ of the i^{th} block is randomly generated.
Let the *PSD* matrix $[G'_{ij}]$ be defined as:

$$[G'_{ij}] = \begin{bmatrix} G_1 & G_1 & \cdots & G_1 \\ \vdots & \vdots & \ddots & \vdots \\ G_{N_h} & G_{N_h} & \cdots & G_{N_h} \end{bmatrix} \tag{1.38}$$

where N_h is the number of harmonics/*PSD* points.

This matrix has N_h rows and n_b columns, with the j^{th} column being the PSD vector of the j^{th} block of the reference signal ($j = 1, \dots, n_b$). Eq.(1.38), where all the columns have the same elements (harmonic amplitudes), refers implicitly to a signal having a stationary PSD. On the other hand, the PSD matrix $[G''_{ij}]$ corresponding to the signal synthesized via the MLV algorithm has the following form:

$$[G''_{ij}] = \begin{bmatrix} \left(\frac{\sigma_1}{\sigma_{tot}}\right)^2 G_1 & \left(\frac{\sigma_2}{\sigma_{tot}}\right)^2 G_1 & \cdots & \left(\frac{\sigma_{n_b}}{\sigma_{tot}}\right)^2 G_1 \\ \vdots & \vdots & \ddots & \vdots \\ \left(\frac{\sigma_1}{\sigma_{tot}}\right)^2 G_{N_h} & \left(\frac{\sigma_2}{\sigma_{tot}}\right)^2 G_{N_h} & \cdots & \left(\frac{\sigma_{n_b}}{\sigma_{tot}}\right)^2 G_{N_h} \end{bmatrix} \tag{1.39}$$

Both the matrices in Eqs.(1.38) and (1.39) satisfy Eq.(1.34) that may be rewritten in this case, in conformity with the notation used in this subsection, as:

$$\sum_{j=1}^{n_b} G_{ij} = G_i \, n_b \qquad i = 1, \dots, \mathrm{N_h} \tag{1.40}$$

The VSD algorithm synthesizes a signal with a variable PSD over time, corresponding to a PSD matrix having the most general form:

$$[G'''_{ij}] = \begin{bmatrix} G_{11} & G_{12} & \cdots & G_{1n_b} \\ \vdots & \vdots & \ddots & \vdots \\ G_{N_h1} & G_{N_h2} & \cdots & G_{N_hn_b} \end{bmatrix} \tag{1.41}$$

where the elements must comply with Eq.(1.40).
The matrix in Eq.(1.41) is useful to generate signals whose PSD varies over time.
To comprehend the method, a few steps are illustrated to show how the generic matrix's form of Eq.(1.41) can be derived from Eqs.(1.38) and (1.40). The procedure starts from the matrix shown in Eq.(1.38): then, as a first step, the i^{th} row is taken and changed as follows (where $p \in [0,1]$ and l is a positive integer such that $l \leq n_b$):

$$[G_{ij}] = \begin{bmatrix} G_1 & G_1 & \overbrace{G_1}^{j^{th}\text{ column}} & G_1 & G_1 & G_1 \\ \vdots & \vdots & \vdots & \vdots & \vdots & \vdots \\ G_i & \dots pG_i \dots & [1+(l-1)(1-p)]G_i & \dots pG_i \dots & pG_i \dots & G_i \\ \vdots & \vdots & \vdots & \vdots & \vdots & \vdots \\ G_{N_h} & G_{N_h} & G_{N_h} & G_{N_h} & G_{N_h} & G_{N_h} \end{bmatrix} \tag{1.42}$$

Eq.(1.40) is still respected if the terms of the type pG_i are $l-1$ in the ith row and there is only one term of the form: $[1+(l-1)(1-p)]G_i$; the ordering of the terms in the row is unimportant and the remaining $n_b - l$ terms on the same row are still equal to G_i. If similar operations were done not only on the term G_{ij} but on other terms as well and in a random manner, the PSD of each block could be varied still preserving the overall PSD. The steps of the algorithm are given with more detail in the following:

0) insert a reference input signal or, alternatively, a reference PSD and kurtosis value;
1) set the duration T and the sampling frequency F_s of the signal to be synthesized;
2) choose $p \in [0,1]$ (user's choice), start from a certain T_b (automatically set), and set $i = 1$;
3) start from the i^{th} row and set $s = 0$;
4) choose a random element j of that row;
5) generate a positive random integer $l \leq n_b - s$;
6) set:
   $G_{ij} = [1 + (l-1)(1-p)]G_i$ and $s = s + l$;
7) repeat $4 - 5 - 6$ with another value for j (different from the values generated in the previous loops), and another value of l, until $s \geq n_b - 1$;
8) set
$$G_{im} = pG_i;$$
   with m ranging over all the elements of the i^{th} row which have not been modified at step 6;
9) if $i < N_h$, set $i = i + 1$ and repeat from step 3, otherwise proceed to step 10;
10) terminate if the kurtosis of the synthesized signal matches the target value (within a certain tolerance, to be preliminarily set), otherwise repeat from point 2 without changing p but with a different T_b, automatically defined. Decreasing T_b makes the kurtosis value increase and vice versa (this is how the algorithm converges towards target kurtosis).

The algorithm can be implemented efficiently from a computational perspective; however, the bottleneck could be step 10, in which a precise calculation of kurtosis is achieved only if the *IFFT*'s are performed on the *PSD* spectra of the blocks (the phases are randomly generated). This could cause the synthesis procedure to be slow for large signals. A way to speed up the process, by loosening the target precision on the kurtosis value, could be that to implement a special case of Eq.(1.35) without performing the *IFFT*'s:

$$k_{tot} = \frac{3\sum_{i=1}^{n_b} {\sigma_i}^4}{n_b \cdot {\sigma_{tot}}^4} \tag{1.43}$$

Since the phases of the blocks are randomly generated, the latter's kurtosis k_i can be considered approximately equal to 3, thus leading from Eq.(1.35) to Eq.(1.43). This is the more accurate the more wide-banded the *PSD* of the particular block, otherwise that block's kurtosis value would be closer to 1.5, typical of a sinusoid, and the calculation errors would increase. This simplified approach was not necessary in the simulations carried out by the authors: even with signals lasting upwards of 10 minutes and sampled at more than 8 kHz, the synthesis procedure is completed in a few seconds with a standard *pc*.

One of the main features of the algorithm is that the variation of the PSD over time (i.e. over the blocks) is not controlled but randomly generated.

As in the case of the MLV algorithm, the last step is to smooth the signal at the edges of the blocks, in order to avoid unrealistic discontinuities.

2 Durability tests

In this chapter the current state of the art of durability tests is described in the first part. In particular, the fatigue damage spectrum is introduced, together with mathematical formulae used for its calculation. In section 2.1 a technique to extend kurtosis control algorithms to durability tests is described. This technique is already available in the literature, even though the mathematical formulation contained in section 2.1 is original. Then, starting from section 2.2, novel algorithms aimed at fatigue-life tests are proposed.

The mechanical loads operating in real applications are often the cause of fatigue failure of components. Due to their expected lifetime being worth of several hundreds or even thousands of hours, it is usually required to accelerate the tests performed in laboratories. These tests must reproduce the entire fatigue damage experienced by the component during its operational life, but in a shorter amount of time[7].

The metric used to estimate the fatigue damage is a spectral function called "Fatigue Damage Spectrum" (*FDS*) [36-40]. Therefore, the purpose of the laboratory tests is to synthesize signals (Mission Synthesis) that have the same *FDS* as the one calculated from the signal measured in the real application, which is representative of the components' operating conditions.

The calculation of the *FDS* for general signals is performed in the time-domain. It starts from the computation of the relative displacement response[8] of a single degree of freedom (*SDOF*) system; the latter is the most simplistic representation of the *DUT* frequently adopted. To calculate the relative displacement, a fast and accurate ramp-invariant filtering technique is usually employed [50]. Afterwards, the peaks and valleys (i.e. extrema) of the relative displacement are extracted from the time-series, which are then input to a time-counting algorithm (usually the Rainflow counting) in order to find the amplitudes of the damaging cycles.

This procedure is looped through a diverse range of *SDOF* systems' natural frequencies, which take into account the fact that the component to be tested is unknown in practice.

It is well known [40] that current standard practices lead to the synthesis of signals characterized by a Gaussian distribution of their values, with the specification being prescribed by a target *FDS* and duration. The distribution is Gaussian because the *FDS* specification translates to a *PSD* specification, with the phases being generated randomly; this leads to a Gaussian distribution according to the discussion in chapter 1.

How to obtain a *PSD* from a *FDS* was described by C. Lalanne [40], who proposed a methodology to synthesize a *PSD* from a target *FDS*. From the *PSD*, the actual time-series is then generated by performing the *IFFT* on the *PSD* as described in chapter 1.

A most general expression for the fatigue damage's expected value is the following [40]:

$$D(f_n) = \frac{K^b}{C} T N_p \int_0^{+\infty} \Delta z^b \, f_{\Delta Z}(\Delta z) d\Delta z \tag{2.1}$$

[7] The so-called Inverse Power Law is usually employed to scale vibration data in order to obtain a desired test duration, by knowing the time-to-failure associated with the unscaled data.

[8] Some authors prefer to calculate the pseudo-velocity instead of relative displacements [14].

When the damage is thought of as a function of f_n, $D(f_n)$ represents the *FDS*. Appendix E provides another expression for the damage, which is equivalent to Eq.(2.1).
The integral in Eq.(2.1) is the b^{th} moment of the peak-valley amplitudes contained in the (random) relative displacement time-series (i.e. the *RV* ΔZ). In general, the m^{th} moment M_{mX} of a positive *RV* called X is defined as:

$$M_{mX} = \int_0^{+\infty} x^m \, f_X(x) dx \tag{2.2}$$

If X is a discrete process constituted by a sufficiently large number of samples N_s, for which the assumption of ergodicity holds [33], then:

$$M_{mX} \approx \frac{1}{N_s} \sum_{j=1}^{N_s} x[j]^m \tag{2.3}$$

where $x[j]$ is the j^{th} sample of the underlying discrete stochastic process.
With the assumption that the reference signal is Gaussian and the system narrow-banded (i.e. characterized by small values of ζ typically in the range 1%-10%), an equation [36, 40] that relates the *FDS* to z_{rms} is the following:

$$D(f_n) = \frac{K^b}{C} T f_n \left(\sqrt{2}\, z_{rms}(f_n)\right)^b \Gamma\left(\frac{b}{2} + 1\right) \tag{2.4}$$

where Γ is the gamma function:

$$\Gamma(x) = \int_0^{\infty} \alpha^{x-1} e^{-\alpha} d\alpha \quad , \quad \Re(x) > 0 \tag{2.5}$$

The z_{rms} value can be related to the *PSD* of the input signal[9] via [40,41]:

$$z_{rms}(f_n)^2 = \frac{1}{2\pi(2\pi f_n)^3} \int_0^{\infty} \frac{G(h)}{(h^2-1)^2 + (2\zeta h)^2} dh \tag{2.6}$$

Using Eqs.(2.4-2.6), it is possible to implement efficient procedures to compute the *FDS* from a *PSD* or vice versa [40].
In Eqs.(2.1,2.4,2.6) the expressions for the *FDS* $D(f_n)$ and root mean square of relative displacement $z_{rms}(f_n)$ hold true for both continuous and discrete values of the natural frequency f_n. This is useful because the expressions for these functions do not change when computed numerically, namely when the parameter f_n assumes only discrete values. In the following, the notation $x[\cdot]$ will be used to indicate a discrete signal x, whereas in the case of x being continuous it will be denoted as $x(\cdot)$. Unlike $D[f_n]$ and $z_{rms}[f_n]$, the function $G(h)$ in Eq.(2.6) is rigorously continuous, it being an integrand. However, the *PSD* is discrete in practice; therefore, it is required to discretize the integral. A straightforward expression can be derived by considering $G(h)$ as a sum of Dirac deltas centered at different frequencies:

$$G(h) = \sum_j G[j] \cdot \delta(j - h[j]) \tag{2.7}$$

where $G[j]$ is the j^{th} *PSD* point and $h[j]$ is the j^{th} frequency $f[j]$ of the *PSD* divided by the frequency of the *SDOF* system, namely:

[9] It is worth recalling that z_{rms} is a displacement, whereas the input signal is an acceleration.

$$h[j] = \frac{f[j]}{f_n} \tag{2.8}$$

By inserting Eqs.(2.7-2.8) in Eq.(2.6), one obtains:

$$z_{rms}[f_n]^2 = \frac{1}{2\pi(2\pi)^3} \sum_j \frac{f_n \, G[j]}{\left(f[j]^2 - {f_n}^2\right)^2 + (2\zeta \, f[j] \, f_n)^2} \tag{2.9}$$

As an alternative to Eq.(2.9), continuous expressions of $G(h)$ could be obtained, as described by C. Lalanne [41], by interpolating the discrete points $G[j]$ in different ways (e.g. linearly or logarithmically).

In the time-domain, the difficulty in evaluating the *FDS* using Eq.(2.1) is mostly due to the integral therein, because the statistical distribution $f_{\Delta Z}(\Delta z)$ is generally unknown for real-life random excitations unless computed numerically, which could be done but at the expense of an increased number of computations at each loop.

Another parameter to be estimated in order to evaluate Eq.(2.1) is N_p. In random vibration testing, its value is usually set equal to f_n under the assumption of a narrow-banded *SDOF* system, implying that the component is lightly damped, which is usually the case in practice. For all these reasons, current time-domain algorithms use the following formula to compute the damage in place of Eq.(2.1):

$$D(f_n) = \frac{K^b}{C} \sum_j n_j \, {\Delta z_j}^b \tag{2.10}$$

where n_j is the number of amplitude cycles Δz_j extracted (by any counting algorithm) from the peaks and valleys of the *SDOF* system response $z[\cdot]$ at the natural frequency f_n. Eq.(2.10) holds regardless of the bandwidth of the *SDOF* system.

Since time-domain methods are expensive computational-wise, in Appendix F an improvement of current time-domain methods is proposed, aiming at a compromise between precision and speed.

The standard frequency domain-approach is an alternative to time-domain methods; the former estimates the damage in terms of a Power Spectral Density (*PSD*) with the assumption of the distribution of the reference signal being stationary and Gaussian.

The Gaussian distribution could be a strong limitation given the recurring non-Gaussianity of reference signals in practice. Non-Gaussian features are often due to high peaks/bursts located in the signal with a random pattern (i.e. caused by micro-collisions, road-bumps, etc.) and/or deterministic components (i.e. sinusoidal tones, which prevail over the background noise). If mostly bursts and peaks characterize a signal, its distribution is called Leptokurtic, whereas if sinusoidal tones are predominant, the distribution is called Platykurtic, otherwise it is Gaussian. In general, it is complicated to quantify non-Gaussianity with simple global parameters, because of the usual non-stationarities being present locally in some parts of the reference signals. However, the simplest parameter adopted in the literature is the already discussed kurtosis, whose value allows to outline a boundary between Gaussian (when kurtosis equals 3), Leptokurtic (when kurtosis is larger than 3) and Platykurtic (when kurtosis is smaller than 3) distributions [41].

Since kurtosis is a simple metric that could control the "nature" of a signal (i.e. its distribution), several authors [9-25] proposed different procedures to synthesize signals with prescribed kurtosis value and Power Spectral Density (*PSD*). As described in chapter 1, these procedures are enclosed in the category of the so-called "kurtosis control" methods. They do not focus directly on preserving the same fatigue damage or *FDS* function, but rather on preserving the kurtosis of the reference signals and their *PSD*. As suggested by J. Antoni et al. [51,52], kurtosis is a *global* parameter and should not

be considered a fatigue damage metric per se. M. Troncossi et al. [53], provided cases where signals with the same kurtosis value could have substantially different Fatigue Damage Spectra. This is the reason why, together with the kurtosis parameter, it would be wise to take into consideration other features related to non-stationarities. This is also one of the reasons why other tools, such as the spectral kurtosis [51] and the kurtogram [54] (as well as *FDS* itself), are present in the literature.
With these caveats highlighted, kurtosis still remains a useful tool if considered together with other metrics, such as the *PSD* (and its variation over time) and especially the *FDS* in the case of durability tests. At present, to the author's knowledge, only F. Kihm et al. [34] proposed novel algorithms for non-Gaussian accelerated tests, seeking to control the *FDS* and kurtosis value. The aim of section 2.1 is to revise the method proposed by F. Kihm with additional considerations; then, in section 2.2 novel algorithms are proposed for the synthesis of more realistic vibration tests with Leptokurtic signals.

2.1 Extension of kurtosis control algorithms

F. Kihm et al. [34] proposed a novel procedure that modifies a signal synthesized by a kurtosis-control algorithm so that its *FDS* matches a reference input one, with the aim of preserving its non-Gaussianity as well. In order to achieve the *FDS* match, a filter is used. The steps of the procedure and the filter definition are briefly reported:

1) calculate the *FDS* of the reference and synthesized signal, respectively $D_r(f_n)$ and $D(f_n)$;
2) define the spectral function: $G(f_n) = \left[\frac{D_r(f_n)}{D(f_n)}\right]^{\frac{1}{b}}$;
3) calculate the *IFFT* of $G(f_n)$ to obtain the impulse response of the filter;
4) convolve the so-obtained impulse response with the synthesized signal.

The mathematical justification is given next.
Eq.(2.1) could be equivalently re-written in terms of $z(t)$ in the following way (see Appendix E):

$$D(f_n) = \frac{N_p T K^b}{C} \int_{-\infty}^{\infty} \int_{-\infty}^{\infty} (z(t_2) - z(t_1))^b \; p(t_1, t_2)\, dt_1 dt_2 \qquad (2.11)$$

where $p(t_1, t_2)$ is the probability density to find a valley/trough at instant t_1 and its corresponding peak at instant t_2. Since $z(t)$ can be related to the signal $x(t)$ (which is the acceleration signal generated by any kurtosis control algorithm) via the latter's convolution with the impulse response function $h(t)$ of the system:

$$z(t) = \int_{-\infty}^{\infty} x(\tau) h(t - \tau) d\tau \qquad (2.12)$$

equation (2.11) can also be put in the following form:

$$D(f_n) = \frac{N_p T K^b}{C} \int_{-\infty}^{\infty} \int_{-\infty}^{\infty} \left(\int_{-\infty}^{\infty} x(\tau)[h(t_2 - \tau) - h(t_1 - \tau)] d\tau \right)^b \; p(t_1, t_2)\, dt_1 dt_2 \qquad (2.13)$$

It is now assumed that the Fatigue Damage Spectrum $D(f_n)$ of $x(t)$ has been computed and it differs from the reference one, symbolically written as $D_r(f_n)$. In order to simplify the mathematical details and arrive at simple results, it is supposed that the spectral function:

$$G(f_n) = \left[\frac{D_r(f_n)}{D(f_n)}\right]^{\frac{1}{b}} \tag{2.14}$$

can be considered relatively constant over the natural frequency axis. One should note that in Eq.(2.14) $G(f_n)$ can be considered relatively constant if the shape of $D(f_n)$ is similar to that of $D_r(f_n)$, but the same condition can also be approached as the coefficient b related to Wohler's curve slope increases. Hence, its *IFFT* is approximately proportional to a Dirac delta:

$$g(t) \approx \left[\frac{D_r(f_n)}{D(f_n)}\right]^{\frac{1}{b}} \delta(t) \tag{2.15}$$

If a new signal $\check{x}(t)$ is considered, given by the convolution between $x(t)$ and $g(t)$, its *FDS* $\check{D}(f_n)$ can be easily proved to be equal to the reference one.

Simple mathematical steps[10] show that the *FDS* of the function $\check{x}(t)$, obtained from convolving $x(t)$ with $g(t)$, is indeed equal to the reference one. Thus, the filter defined by Eq.(2.14) is effective in adjusting the *FDS* of a signal synthesized by kurtosis-control methods, provided the assumption of constancy of $\left[\frac{D_r(f_n)}{D(f_n)}\right]^{\frac{1}{b}}$ with respect to f_n holds.

After this filtering procedure, the kurtosis value and *PSD* are modified; nevertheless, the peaks and bursts, if present, may remain unaltered as it will be shown in chapter 3. It will also be shown that in some cases the signal tends to Gaussian after filtering, thus losing its non-Gaussian characteristics. A possible downside of the procedure is that the problem is tackled indirectly: namely, a signal with a prescribed kurtosis value and *PSD* is synthesized, then its *FDS* is computed. The computation of the *FDS* is usually time expensive computationally especially if a time domain calculation is performed (i.e. via Counting methods applied to long time-series). F. Kihm et. al [19,34] proposed a frequency domain method for the calculation of the *FDS*, which is renowned for its better computational efficiency. This could be done since the synthesized signal was assumed to be obtained by modulation, with the modulation defining the duration and separation of the signal's bursts, and the signal to be modulated was supposed to be stationary and Gaussian.
The distribution of the peaks of the output signal f_p can be calculated using the rule to find the *PDF* of the product of two independent random variables *X* (representing the peaks of a stationary Gaussian

[10] The mathematical proof is obtained by making use of Eqs.(2.13, 2.15) and the definition of $\check{x}(t)$:

$$\check{D}(f_n) = \frac{N_p T K^b}{C} \int_{-\infty}^{\infty}\int_{-\infty}^{\infty}\left(\int_{-\infty}^{\infty}\check{x}(\tau)[h(t_2-\tau)-h(t_1-\tau)]d\tau\right)^b p(t_1,t_2)\,dt_1dt_2 =$$

$$= \frac{N_p T K^b}{C} \int_{-\infty}^{\infty}\int_{-\infty}^{\infty}\left[\int_{-\infty}^{\infty}\left(\int_{-\infty}^{\infty}x(s)g(s-\tau)ds\right)[h(t_2-\tau)-h(t_1-\tau)]d\tau\right]^b p(t_1,t_2)\,dt_1dt_2 =$$

$$= \frac{N_p T K^b}{C} \int_{-\infty}^{\infty}\int_{-\infty}^{\infty}\left[\int_{-\infty}^{\infty}\left(\int_{-\infty}^{\infty}x(s)\left[\frac{D_r(f_n)}{D(f_n)}\right]^{\frac{1}{b}}\delta(s-\tau)ds\right)[h(t_2-\tau)-h(t_1-\tau)]d\tau\right]^b p(t_1,t_2)\,dt_1dt_2 =$$

$$= \frac{D_r(f_n)}{D(f_n)}\frac{N_p T K^b}{C} \int_{-\infty}^{\infty}\int_{-\infty}^{\infty}\left[\int_{-\infty}^{\infty}\left(\int_{-\infty}^{\infty}x(s)\delta(s-\tau)ds\right)[h(t_2-\tau)-h(t_1-\tau)]d\tau\right]^b p(t_1,t_2)\,dt_1dt_2 =$$

$$= \frac{D_r(f_n)}{D(f_n)}\frac{N_p T K^b}{C} \int_{-\infty}^{\infty}\int_{-\infty}^{\infty}\left(\int_{-\infty}^{\infty}x(\tau)[h(t_2-\tau)-h(t_1-\tau)]d\tau\right)^b p(t_1,t_2)\,dt_1dt_2 = \frac{D_r(f_n)}{D(f_n)}D(f_n) = D_r(f_n)\ \blacksquare$$

signal) and A (representing the modulation) with distributions f_G and f_A respectively [19], given by the equation:

$$f_p(s) = \int_{-\infty}^{\infty} f_G(a) \frac{1}{|a|} f_A\left(\frac{s}{a}\right) da \tag{2.16}$$

Eq.(2.16) requires an expression for the *PDF* of the modulating signal to be determined. This task is though straightforward for simple burst waveforms such as a sinusoid, for example. The fatigue damage is then calculated based on the stress peak distribution and the material Wohler's curve. Kurtosis and damage can therefore be related mathematically in this case, without resorting to time domain methods. However, not all signals in practice can be obtained via modulation, as motivated in the next section.

It has already been highlighted that some of the most sought-after characteristics that a vibration test should have are: the possibility of reducing the duration of the tests, the same *FDS* as the signals measured in real applications, as well as the preservation of the "nature" (i.e. distribution) of these signals. A step forward in the field of random fatigue vibration tests, namely to control the nature of the signals together with the *FDS*, was made by F. Kihm et al [34] as described in this section, who developed an algorithm that is based on the correction of a signal synthesized by kurtosis-control methods in order to match a target *FDS*. However, the *PSD* and kurtosis value are affected; in particular, the *PSD* is affected the more the greater the time reduction factor of the tests. In fact, as the duration of the synthesized signal decreases, its energy level is increased in order to contain the same damage potential as the reference signal. Also, the correction of the synthesized signal is dependent upon the computation of the *FDS* of the signal itself, which is time consuming. Another possible limitation is that the signals considered are based on modulation. The latter method is one of the most used since it is effective in transferring the kurtosis value to the response of the *DUT* if the signal bursts of the modulating signal have greater duration than the inverse of the bandwidth of the lightly damped system [18]. As it will be shown in the simulation results, the kurtosis of the system's response is close to that of the input signal in the case of algorithms based on modulation; the behavior of the response to a signal measured in real applications may be different. The fact that the kurtosis of the output is similar to that of the input in the case of modulated signals can be motivated by the following reason: the blocks constituting the synthesized signal all have the same *PSD* bandwidth and shape [17], thus either resonance is present in *each* of the blocks or in none of them. In both cases, the shapes of the input and output signals are similar.

On the other hand, real signals could also contain narrow-band blocks interspersed with wide-band ones; in this case resonance effects may occur and their occurrence could lead to high peaks in some blocks of the response that are not present in the input signal. This may cause the response to have a much higher kurtosis value than the input, which is often the case in real applications.

In the following four novel algorithms are proposed, which all present different features and face the above-mentioned problems, with the purpose of expanding on the work of Kihm et al.

2.2 A priori control of the Fatigue Damage Spectrum

In this section, four novel Mission Synthesis algorithms are proposed, which achieve controlling the *FDS* in conjunction with other parameters, specific to the algorithm selected. Their commonality is the synthesis of Leptokurtic signals, thus extending the standard procedure described in the literature [39,40] and some other recent methodologies [34]. Instead of achieving the *FDS* control a posteriori,

by means of a filtering process applied to signals generated by kurtosis control algorithms as described in section 2.1, the *FDS* is controlled a priori, without resorting to the intermediate step of kurtosis control.
The first algorithm that will be introduced, named *kFDS*, manages to control both the *FDS* and kurtosis value of a signal to be synthesized. Because of the limitations of this global parameter[11], highlighted in the introduction of chapter 2 and section 2.1, three more algorithms are proposed. The second algorithm is named *RF* and complies with a prescribed *FDS* and *RMS* value that the synthesized signal is required to have, irrespective of the possible time reduction factor applied to the test. Subsequently, the *RP* algorithm will be introduced, which adds the possibility of controlling the *PSD* shape in addition to the *FDS* and *RMS* value. Finally, a modified version of the *RF* is shown, the *PSF* algorithm, which omits to control the *RMS* value and complies only with a *FDS* and a *PSD* shape specification.
The main advantages of the methodologies are related to the computational efficiency due to the simple mathematical formulae required, which are basically the same as those found in the standard practice, with the necessary time-domain calculations being performed only to calculate the *FDS* from reference signals.

2.2.1 *kFDS* algorithm

This algorithm, hereinafter referred to as *kFDS,* achieves synthesizing signals with a prescribed *FDS* and kurtosis value. It is based on the observation that the overall *FDS* $D(f_n)$ of a signal is (approximately) equal to the sum of all the smaller blocks' *FDS* spectra the signal is composed of, namely:

$$D(f_n) = \frac{1}{n}\sum_{j=1}^{n} D_j(f_n) \tag{2.17}$$

where D_j is the *FDS* of the j^{th} block and n is the total number of blocks which the signal is considered divided into, hereinafter supposed to have the same duration. In the following, the overall *FDS* $D(f_n)$ must be viewed as the desired *FDS* (i.e. the one prescribed by the specification), which should be characteristic of the synthesized signal(s). Eq.(2.17) is an approximation because by introducing blocks, possible interactions among them (e.g. due to the counting methods used in the computation) are neglected. Nevertheless, these effects are negligible if the ratio of the number of blocks to the number of points of the signal in each block is sufficiently small, which will be the case hereinafter. The algorithm defines n coefficients v_j such that:

$$D_j(f_n) = v_j D(f_n) \tag{2.18}$$

thereby constraining their choice to comply with the following equation:

$$\frac{1}{n}\sum_{j=1}^{n} v_j = 1 \tag{2.19}$$

[11] However, it is worth highlighting that if kurtosis is controlled together with the *FDS* of a signal, it may become much more meaningful than just kurtosis considered by itself. The practical application shown in chapter 4 will exemplify the statement.

The signal to be synthesized is considered to be generated by concatenating n different Gaussian blocks, whose target *FDS* functions are the ones given by Eq.(2.18). The "discontinuities" possibly arising from concatenation are smoothed out by interpolating the values close to the edges of adjoining blocks, without affecting the overall damage noticeably and the target kurtosis value is achieved as explained in the following.
From the target *FDS* of the j^{th} block $D_j(f_n)$, a *PSD* $G_j(f_n)$ is synthesized by means of the standard procedure reported in chapter 2, from which the (Gaussian) time-series constituting the block is generated. Since the blocks are characterized by different *FDS* curves, some can have a higher energy level than others, thus leading to Leptokurtic signals. The kurtosis value can be achieved by a small number of iterations, each one performed with different v_j coefficients; the entire procedure can be summarized, with all necessary details, by the following steps:

1) start with the coefficients v_j being "close to" homogeneous, thus "almost" equal to $1/n$. The words "close to" and "almost" instead of exactly "equal to" permit to spare one iteration, since in case the coefficients were exactly equal to $1/n$, a signal with kurtosis (approximately) equal to 3 would be obtained.
   Also choose a tolerance value Δk for target kurtosis;
2) calculate a *PSD* G from the overall *FDS* according to Eqs.(2.4-2.6);
3) set the *PSD* G_j of each block j according to the following equation:

$$G_j(f_n) = v_j^{\frac{2}{b}} G(f_n) \tag{2.20}$$

4) calculate the variance ${\sigma_j}^2$ of each block by integrating its *PSD* G_j;
5) calculate the variance ${\sigma_{tot}}^2$ of the signal with the following formula (analogous to Eq.(1.33)):

$${\sigma_{tot}}^2 = \frac{\sum_{j=1}^{n} {\sigma_j}^2}{n} \tag{2.21}$$

6) calculate the kurtosis k_{tot} of the signal with the following (approximated) formula (analogous to Eq.(1.43)):

$$k_{tot} = \frac{3\sum_{j=1}^{n} {\sigma_j}^4}{n \cdot {\sigma_{tot}}^4} \tag{2.22}$$

7) compare the kurtosis of the signal k_{tot} with the reference value k_{ref}: if $k_{tot} < k_{ref} - \Delta k$ increase the variability of the v_j coefficients (in a random manner) and go to step 3, if $k_{tot} > k_{ref} + \Delta k$ decrease the variability of the v_j coefficients and go to step 3, otherwise proceed to step 8;
8) generate the blocks by applying the *IFFT* to the *PSD*'s G_j;
9) concatenate the blocks so generated and smooth them by means of proper interpolation of the values close to the edges of adjoining blocks.

The steps of the algorithm converge rapidly since there are no burdensome analytical formulae to compute on large vectors.

2.2.2 *RF* algorithm

This algorithm, hereinafter referred to as *RF*, achieves synthesizing signals with a prescribed *RMS* value and the *FDS*. The reason why it was developed is that if the duration of a vibration test is

reduced, the energy level (i.e. the *PSD*) of the signal increases. This is true for both the standard algorithm described in chapter 2 and for those methods that control the *FDS* and the kurtosis value (e.g. *kFDS* algorithm). In fact, by fixing a certain kurtosis value, if the duration of the signal is reduced while at the same time preserving the target *FDS*, the energy level has to increase. This algorithm manages to preserve the *FDS* and at the same time the energy level, namely the variance (i.e. the square of the *RMS*), with any selected time reduction. The shape of the *PSD* is constrained by Eqs.(2.4-2.6), whereas its intensity can be manipulated by adjusting the kurtosis value[12] in order to achieve the prescribed *RMS*. If the target kurtosis is greater than 3, one obtains the same *PSD* shape as in the Gaussian case, but its intensity decreases because of the presence of high bursts in the signal. The generation of the blocks of the signal is identical to that of the *kFDS* algorithm, but with a different procedure to find the coefficients v_j. The steps of the algorithm are similar and reported in the following:

1) start with the coefficients v_j being "close to" homogeneous, thus "almost" equal to $1/n$. The words "close to" and "almost" instead of exactly "equal to" permit to spare one iteration, since if the coefficients were exactly equal to $1/n$, a signal with kurtosis equal to 3 would be obtained.
   Also choose a tolerance value $\Delta\sigma$ for target *RMS*;
2) calculate a *PSD* G from the overall *FDS* according to Eqs.(2.4-2.6);
3) set the *PSD* G_j of each block j according to Eq.(2.20);
4) calculate the variance ${\sigma_j}^2$ of each block by integrating its *PSD* G_j;
5) calculate the *RMS* σ_{tot} of the signal to be synthesized via Eq.(2.21);
6) compare the *RMS* of the signal σ_{tot} with the reference value σ_{ref} (computed from the reference signal): if $\sigma_{tot} > \sigma_{ref} + \Delta\sigma$ increase the variability of the v_j coefficients (in a random manner) and go to step 3, if $\sigma_{tot} < \sigma_{ref} - \Delta\sigma$ decrease the variability of the v_j coefficients and go to step 3, otherwise proceed to step 7;
7) generate the blocks by applying the *IFFT* to the *PSD*'s G_j;
8) concatenate the blocks so generated and smooth them by means of proper interpolation of the values close to the edges of adjoining blocks.

2.2.3 *PF* algorithm

This algorithm, hereinafter referred to as *PF*, manages to control: the *PSD* shape of a signal, its *RMS* and the *FDS* (i.e. it controls the *PSD* and the *FDS*). Unlike the *kFDS* and *RF* algorithm, this one does not use modulation. In fact, from Eq.(2.20) and step 8 in subsection 2.2.1 (or steps 3 and 8 in subsection 2.2.2) it is evident that the time-series of each block of the *kFDS* and *RF* algorithms was achieved by modulating a Gaussian time-series by ${v_j}^{1/b}$, with j an integer from 1 to n varying over the blocks that constitute the signal (i.e. varying over time). In addition to the features of the *RF* algorithm, the *PF* adds the control of the *PSD* shape to that of the *RMS* and *FDS*, with any time reduction selected.
The first step considers the duration T of the signal to be given by the sum of the duration t_B of all the blocks with higher energy (bursts) and the duration t_L of all the blocks with lower energy (i.e. $T=t_B+t_L$). Then, the following assumption is made: the damage caused by the blocks with lower

[12] In this case the kurtosis parameter depends on the target *RMS* and is not necessarily equal to the reference signal's kurtosis.

energy can be neglected. This assumption is reasonable if the signal is Leptokurtic and even more so if time reduction is applied to the test. In fact, in order to preserve the *RMS* value (as well as the *FDS*) and reduce the duration and/or cause the synthesized signals to be Leptokurtic, the signal must contain "high-energy" blocks interspersed with "low-energy" ones. It should be noted that the *PF* algorithm considers either "high-energy" or "low-energy" blocks, thus only two levels; this is a difference with respect to *kFDS* and *RF*, which could synthesize signals with a variable variance over n blocks (i.e. n possibly different energy levels).
The next step is the synthesis of a *PSD* G_B from the reference *FDS* via Eqs.(2.4-2.6), with the latter being computed over the duration t_B of the blocks with high energy.
Then, the *PSD* G_L of the blocks with low energy is computed by ensuring compliance with the reference *PSD* $G_{ref}(f_n)$, namely:

$$G_L(f_n) = \frac{G_{ref}(f_n) \cdot (t_L + t_B) - G_B(f_n) \cdot t_B}{t_L} \tag{2.23}$$

The low-energy part of the signal (characterized by duration t_L) is then generated by applying the *IFFT* to G_L, whereas the high-energy part (characterized by duration t_B) by applying the *IFFT* to G_B.
The next step, after having set a number of blocks n, is to concatenate the random permutations obtained by splitting the low-energy and high-energy part in n blocks. This is legitimate if Eq.(2.17) holds, because in doing the permutations the damage must remain the same. The permutations must also preserve the overall *PSD* of the signal, maintaining it equal to the reference one: G_{ref}. This constraint is also respected if the number of blocks n is chosen less than or equal to the number of blocks used in the computation of the reference *PSD* (calculated from the reference signal). In general, the number of blocks involved in the computation is related to the statistical error of the *PSD* spectrum [41]. The steps of the algorithms are summarized with more detail in the following:

1) automatically set the duration t_B of all the bursts of the signal and the duration t_L of the low energy part of the signal such that $t_B + t_L$ be equal to the duration T of the signal to be synthesized. Also set the number of blocks n of the signal to be synthesized. The latter should be set equal or smaller than the number of blocks used for the calculation of the reference *PSD* (e.g. the total number of points in the signal divided by the *NFFT* parameter used in the function pwelch in $Matlab^{®}$);
2) compute a *PSD* G_B from the overall *FDS* according to Eqs.(2.4-2.6), with the duration t_B in place of T in Eq.(2.4);
3) set the *PSD* G_L of the low-energy part in accordance with Eq.(2.23);
   If $G_L(f_n) < 0$ for some frequency f_n (this could happen because of the minus sign in Eq.(2.23)), restart from step 2 with a lower t_B, automatically set, and set t_L equal to $T - t_B$;
4) construct two time-series: one generated by performing the *IFFT* on G_L , the other by applying the same technique to G_B, and concatenate them into one signal;
5) divide the signal so obtained into n blocks;
6) do a random permutation of the blocks so generated and smooth the signal by means of proper interpolation of the values close to the edges of adjoining blocks.

2.2.4 *PSF* algorithm

This algorithm, hereinafter referred to as *PSF*, achieves controlling the *PSD* shape of a signal and the *FDS*. Unlike the *PF* algorithm, the *PSF* does not control the *RMS* in case time reduction is applied;

in fact, the energy level would increase in place of the kurtosis value as occurs with the *PF* algorithm, but the shape of the reference *PSD* would remain preserved. If no time reduction is applied, the *PF* and the *PSF* algorithm are conceptually identical. The detailed steps are reported in the following:

1) let r be the reduction factor of the test ($r \geq 1$): set the target *FDS* $D(f_n)$ according to: $D(f_n) = D_{ref}(f_n)/\, r$ where $D_{ref}(f_n)$ is the *FDS* prescribed by the specification;
2) automatically set the duration t_B of all the bursts of the signal and the duration t_L of the low energy part of the signal such that $t_B + t_L$ be equal to the duration T of the signal to be synthesized. Also set the number of blocks n of the signal to be synthesized. The latter should be set equal or smaller than the number of blocks used for the calculation of the reference *PSD* (e.g. the total number of points in the signal divided by the *NFFT* parameter used in the function pwelch in $Matlab^{®}$);
3) calculate a *PSD* G_B from the target *FDS* $D(f_n)$ according to Eqs.(2.4-2.6), with the duration t_B in place of T in Eq.(2.4);
4) set the *PSD* G_L of the low-energy part in accordance with Eq.(2.23);
   If $G_L(f_n) < 0$ for some frequency f_n (this could happen because of the minus sign in Eq.(2.23)), restart from step 2 with a lower t_B, automatically set, and set t_L equal to T-t_b.
5) construct two time-series: one generated by performing the *IFFT* on G_L , the other by applying the same technique to G_B, and concatenate them into one signal;
6) divide the signal so obtained into n blocks;
7) do a random permutation of the blocks so generated and smooth the signal by means of proper interpolation of the values close to the edges of adjoining blocks;
8) multiply the time-series so obtained by $r^{1/b}$.

Most of the steps of the *PSF* algorithm are the same as those for the *PF* with the only difference being given by steps 1 and 8.

2.3 Accelerated tests: caveats

The algorithms presented in chapters 1 and 2 can be used to generate signals having a duration which, a priori, could be different from that of the reference signal. The reference signal is one representative measurement from the application considered. For durability tests, this measurement is then usually thought to be replayed in sequence until fatigue failure of the *DUT* occurs; the motivation is due to the fact that measurements representing the thousands of hours' lifetime of the components are unfeasible.

In the case of kurtosis control algorithms, the *PSD* and kurtosis of the reference signal are usually taken as specifications for the Mission Synthesis procedure, whereas in the case of algorithms aimed at durability tests, the specification is the *FDS*. As for the latter category, it may be required to accelerate the tests, namely to shorten the duration of the synthesized signals with respect to that of the reference signals. The signals are generated via a shaker that can be employed in different modes: one mode is the random mode, which generates a (Gaussian) signal starting from a *PSD*. Another mode, which is applicable to the algorithms presented so far, is the waveform replication mode. The latter consists in replicating an already available signal on a shaker; this signal could be measured either from a real environment or synthesized by algorithms. As regards accelerated tests, one has to deal with caveats that do not usually arise in tests preserving the same duration as that of the reference signal. In fact, when reducing the duration, since the *FDS* should be preserved, the severity of the test could be such that the failure mechanism of the *DUT* is not anymore fatigue-related and turns into a yield-type of failure [42,43]; this is obviously undesirable in durability tests. The spectral function

that is usually investigated when evaluating whether the test falls under the fatigue or yield test category is the Maximum Response Spectrum (*MRS*) [40]. The *MRS* represents the maxima of the absolute value of the relative displacement responses $z(t)$ of independently excited *SDOF* systems; the latter have a different natural frequency f_n and the maxima of the responses are plotted against f_n and multiplied by $(2\pi f_n)^2$ in order to obtain the units of acceleration. In accelerated tests, the general rule of thumb is that the MRS of the reference signal should not be much lower than the *MRS* of the test, otherwise one would incur the risk of possibly switching from fatigue failure to a yield failure mechanism. The extent to which the *MRS* of the test can exceed the reference one is not clearly outlined. This is due to the uncertainties related to the simplifying assumptions used in the calculation: for instance, the knowledge of the material of the *DUT*, its shape (which may affect the single degree of freedom assumption), nonlinearities, and the experience of the user may play an important role.

Besides, as the duration decreases, the test becomes more sensitive to parameters such as the coefficient b related to Wohler's curve slope for instance, whose knowledge is definitely not precise. All these aspects should be considered when reducing the duration of a test.

3 Simulation results

In this chapter, the algorithms previously presented in chapters 1 and 2 are tested, starting from the synthesis results of kurtosis control algorithms, which are shown in section 3.1, then moving on to synthesis results related to durability test profiles in section 3.2. As regards kurtosis control, in section 3.1 it is described how to properly select the input parameters for the algorithms. In addition, the PSD plots and kurtosis values of the reference and synthesized profiles are compared, and the response kurtosis of a generic lowly-damped system is also calculated to garner the first visual information about what has only been discussed theoretically so far, that is the so-called Papoulis' Rule. Then, both the fatigue damage spectra associated with the reference profile and with the profile synthesized by kurtosis control are compared; the difference in the FDS is highlighted in order to clarify the necessity of durability tests. Durability tests are addressed in subsection 3.1.1 and section 3.2, by adopting a similar approach to section 3.1, namely comparing the PSD plots and statistical parameters (such as kurtosis), albeit focusing more on the fatigue damage in this case (the FDS curves). In subsection 3.1.1 the kurtosis control algorithms of section 3.1 are simply extended by means of Kihm's filtering technique [34], whereas in section 3.2 the profiles are synthesized by using the algorithms that control the FDS a priori, which were introduced in section 2.2.
The algorithms were tested starting from numerous reference input profiles. For the sake of brevity, only the results of some applications will be shown for each section dedicated to results. Nevertheless, some general considerations can be inferred from the particular cases.

3.1 Kurtosis control

The starting reference signals, here denoted as *RS1* and *RS2*, are field data with a sample rate of 1000 Hz and 300 Hz respectively, with durations of about 660 seconds. The signals' plots and *PSD* are shown in Fig. 3.1, whereas some statistical parameters are listed in Table 3.1, in particular: *RMS*, kurtosis, crest factor. One should note that both reference signals are Leptokurtic. The kurtosis values of the responses of *SDOF* systems having different natural frequencies and a damping coefficient ζ of 2%, are also graphed in Fig. 3.2 to check the sensitivity to the Papoulis' Rule. The responses were obtained in terms of acceleration $[m/s^2]$, by implementing the well-known convolution between the impulse response of the system and the reference signal.

The *PM*, *MLV* and *VSD* algorithms are first applied to the reference signal *RS1*. The input parameters for the *PM* algorithm are:

- duration of the synthesized signal: $T = 660\ s$ (the same as for the reference signal);
- sampling frequency of the synthesized signal: $F_s = 1000\ Hz$;
- phases manipulated in the frequency range: [200 Hz, 400 Hz];
- duration of the synthesized blocks that compose the signal: T_b= 3 s (i.e. the number of blocks is equal to: $n_b = \frac{T}{T_b} = 220$).

The input parameters for the *MLV* algorithm are:

- duration of the synthesized signal $T = 660\ s$ (the same as for the reference signal);
- sampling frequency of the synthesized signal $F_s = 1000\ Hz$;
- $r_\sigma = 0.3$;
- duration of the synthesized blocks that compose the signal: T_b= 3 s $\left(n_b = \frac{T}{T_b} = 220\right)$;
- number of bursts: n_p= 5;

The input parameters for the VSD algorithm are[13]:

- duration of the synthesized signal: T = 660 s
- sampling frequency of the synthesized signal $F_s = 1000\ Hz$;
- p=0.2.

The choice for the interval of frequencies over which the phases were varied in the *PM* algorithm was due to most of the energy content of the signal being contained in the band [200 Hz, 400 Hz] as it can be inferred from the *PSD* of *RS1* plotted in Fig.3.1c.

By inspecting the plot of the signal *RS1*, several distinctive peaks appear. The parameter related to the number of bursts was arbitrarily chosen equal to 5 for the MLV algorithm. In addition, the signal shows a visible amount of variability of the standard deviation over time; hence, the parameter r_σ has been chosen equal to 0.3.

The signals synthesized by the three algorithms are reported in Fig.3.3 along with their PSDs. The PSD spectra plotted in Fig.3.3d-f were computed with a 50% overlap among the n_b blocks and using a Hamming window. The resolution in frequency of the *PSD* curves was therefore chosen equal to the inverse of the T_b parameter of the algorithms. On the other hand, one should note that the *MLV* and *VSD* algorithms theoretically consider 0% overlap and rectangular windows. It is also worth mentioning that the *PSD* curves in Fig.3.3d-f depend on the T_b parameter used by the algorithm selected; since the curves are plotted with the same T_b used by the algorithm, when this parameter is different, the curves could also be visually different (this difference is not conspicuous, but it can be noticed).

The parameter p of the VSD algorithm has a similar meaning to the parameter r_σ of the MLV algorithm. Nevertheless, in order to give the same amount of variability it requires to be set to a lower value[14].

The statistical parameters of the synthesized signals are shown in Table 3.2.

The kurtosis values of the responses are plotted[15] versus the *SDOF* systems' natural frequencies in Fig.3.4a-c. The *FDS* and *MRS* are also computed by assuming $b = 6$ in Fig.3.4d-i; these curves will be considered in section 3.1, when the filtering procedure described in section 2.1 is used to change the *FDS* curves so that they match the reference ones. The frequency resolution of the *MRS* and *MRS* curves is logarithmic (1/12th of an octave).
The results of the *PM*, *MLV* and *VSD* algorithms applied to the reference signal *RS2* are now shown.

The input parameters for the *PM* algorithm are:

- duration of the synthesized signal $T = 660\ s$ (the same as for the reference signal);
- sampling frequency of the synthesized signal $F_s = 300\ Hz$;
- phases manipulated in the frequency range [50 Hz, 100 Hz];
- T_b= 10 s $\left(n_b = \frac{T}{T_b} = 66\right)$.

[13] It is worth noting that, in the case of the *VSD* algorithm, the duration of the synthesized blocks that compose the signal is not an input, as explained in subsection 1.2.3.
[14] This is motivated by the different definitions of the parameters r_σ and p given in subsections 1.2.2 and 1.2.3, but especially on anecdotal evidence obtained from simulations.
[15] It should be noted that the kurtosis of the response to the *VSD* signal reaches much higher values than the responses to the *PM* and *MLV* signals.

The input parameters for the *MLV* algorithm are:

- duration of the synthesized signal $T = 660\ s$ (the same as for the reference signal);
- sampling frequency of the synthesized signal $F_s = 300\ Hz$;
- $r_\sigma = 0.5$;
- T_b= 20 s $\left(n_b = \frac{T}{T_b} = 33\right)$;
- number of bursts: n_p= 4.

The input parameters for the *VSD* algorithm are:

- duration of the synthesized signal: T = 660 s
- sampling frequency of the synthesized signal $F_s = 300\ Hz$;
- p=0.1.

The choice for the interval of frequencies over which the phases were varied was chosen because most of the energy content of the signal is contained in the band [50 Hz, 100 Hz] as it can be inferred from the *PSD* of *RS2* plotted in Fig.3.1d.

By inspecting the plot of the signal *RS2*, few distinctive "peaks" appear. Consequently, the parameter related to the number of bursts was chosen equal to 4 for the MLV algorithm. In addition, the signal shows some variability of the standard deviation[16] over time; hence, the parameter r_σ has been chosen equal to 0.5.

The signals synthesized by the two algorithms are displayed in Fig.3.5 along with their PSDs. The PSD spectra plotted in Fig.3.5d-f were computed with a 50% overlap among the n_b blocks and using a Hamming window. Therefore, the resolution in frequency of the *PSD* curves was chosen equal to the inverse of the T_b parameter. It is also worth mentioning that the *PSD* curves in Fig.3.5d-f depend on the T_b parameter used by the algorithm selected; since the curves are plotted with the same T_b used by the algorithm, when this parameter is different, the curves could also be visually different (this difference is not conspicuous, but it can be noticed).

The statistical parameters of the synthesized signals are shown in Table 3.3.

The kurtosis values of the responses are plotted versus the *SDOF* systems' natural frequencies in Fig.3.6a-c. The *FDS* and *MRS* are computed with Wohler's curve slope $b = 6$ in Fig.3.6d-i. The frequency resolution of the *FDS* and *MRS* curves is logarithmic (1/12th of an octave).

[16] It is also worth recalling that the *RMS* value is nearly coincident with the standard deviation in the case of zero-mean signals.

Table 3.1: Statistical parameters of the reference signals *RS1* and *RS2*

	RS1	***RS2***
RMS $[\boldsymbol{m/s^2}]$	8.28	32.9
Kurtosis [-]	7.36	4.16
Crest factor [-]	10.6	4.81

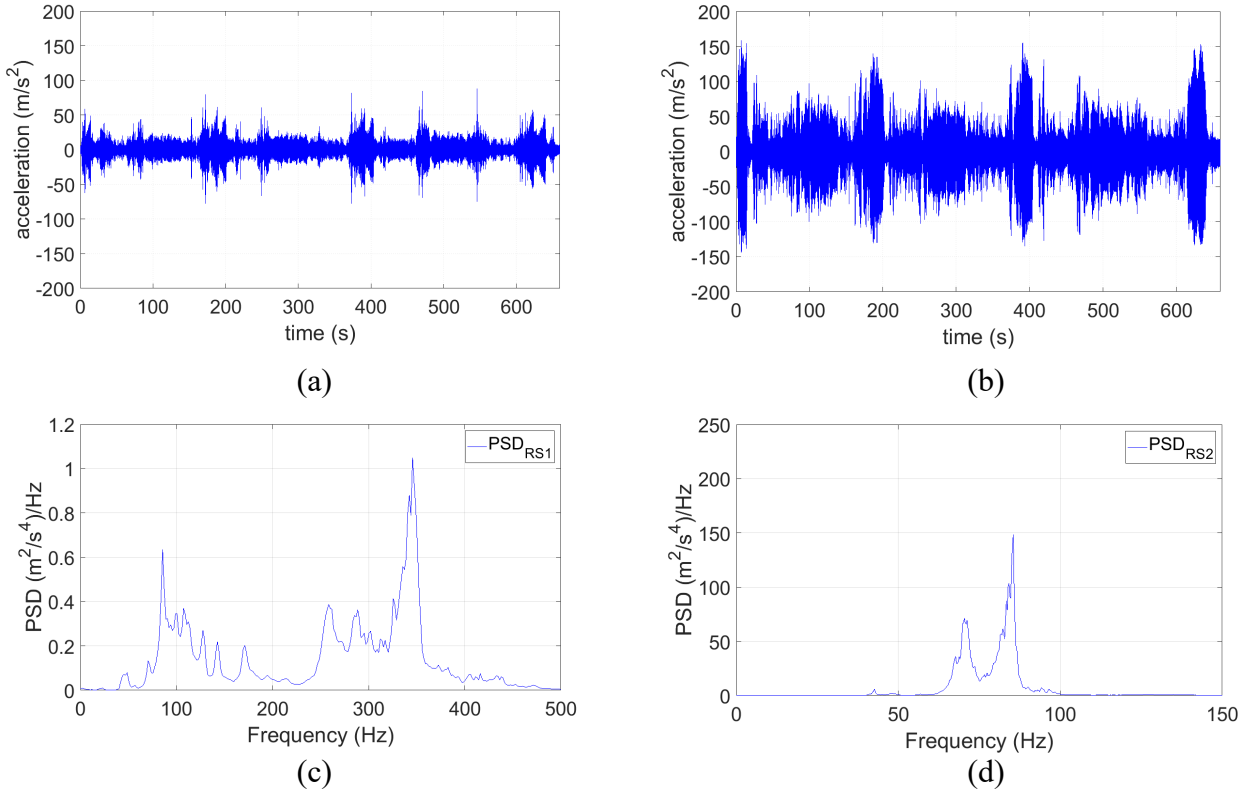

Figure 3.1: Reference signals and their *PSD* plots used in the two applications: a) *RS1*, b) *RS2,* c) *PSD* of signal *RS1,* d) *PSD* of signal *RS2.*

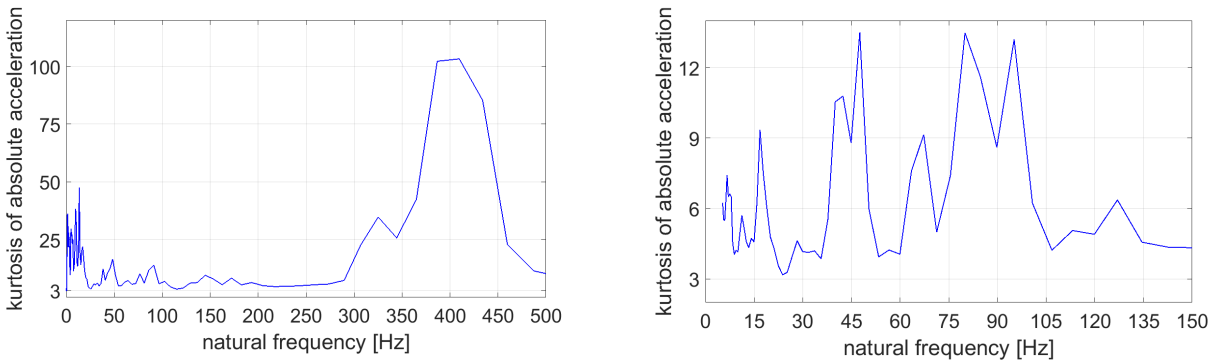

Figure 3.2: Kurtosis of the *SDOF* systems' responses to the signals *RS1* (a) and *RS2* (b) from 0 to their corresponding Nyquist frequencies. The damping coefficient ζ of the *SDOF* systems was set equal to 2%.

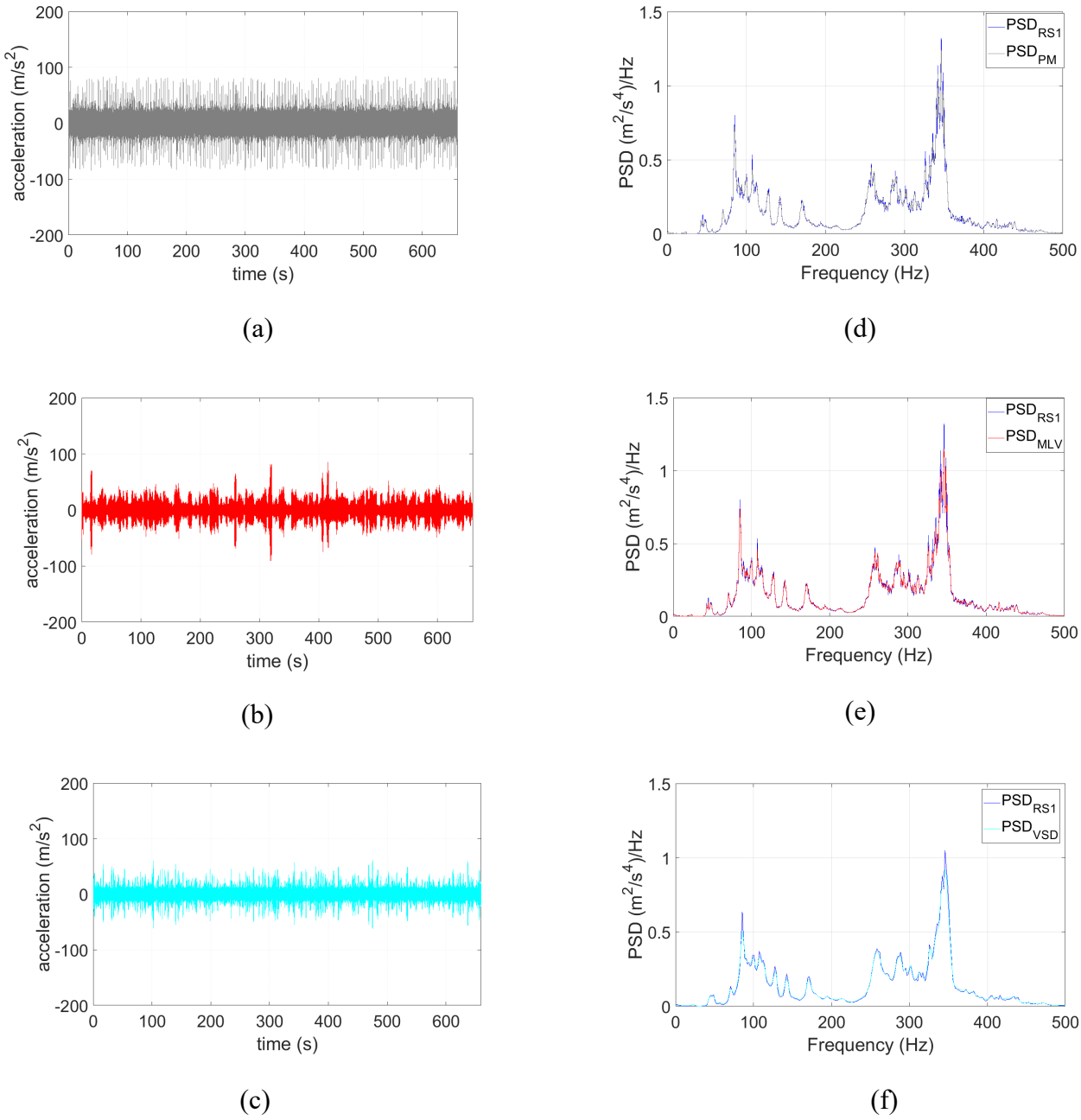

Figure 3.3: Synthesis results starting from the reference input profile *RS1*. Signal synthesized by the: a) *PM*, b) *MLV*, c) *VSD* algorithms. *PSD* comparison between *RS1* and the: d) *PM*. e) *MLV*, f) *VSD* algorithms.

Table 3.2: Statistical parameters of the signals synthesized starting from the reference profile *RS1*

	PM signal	***MLV signal***	***VSD signal***
RMS $[\boldsymbol{m/s^2}]$	8.30	8.28	8.28
Kurtosis [-]	7.29	7.14	7.14
Crest factor [-]	10.2	10.9	7.45

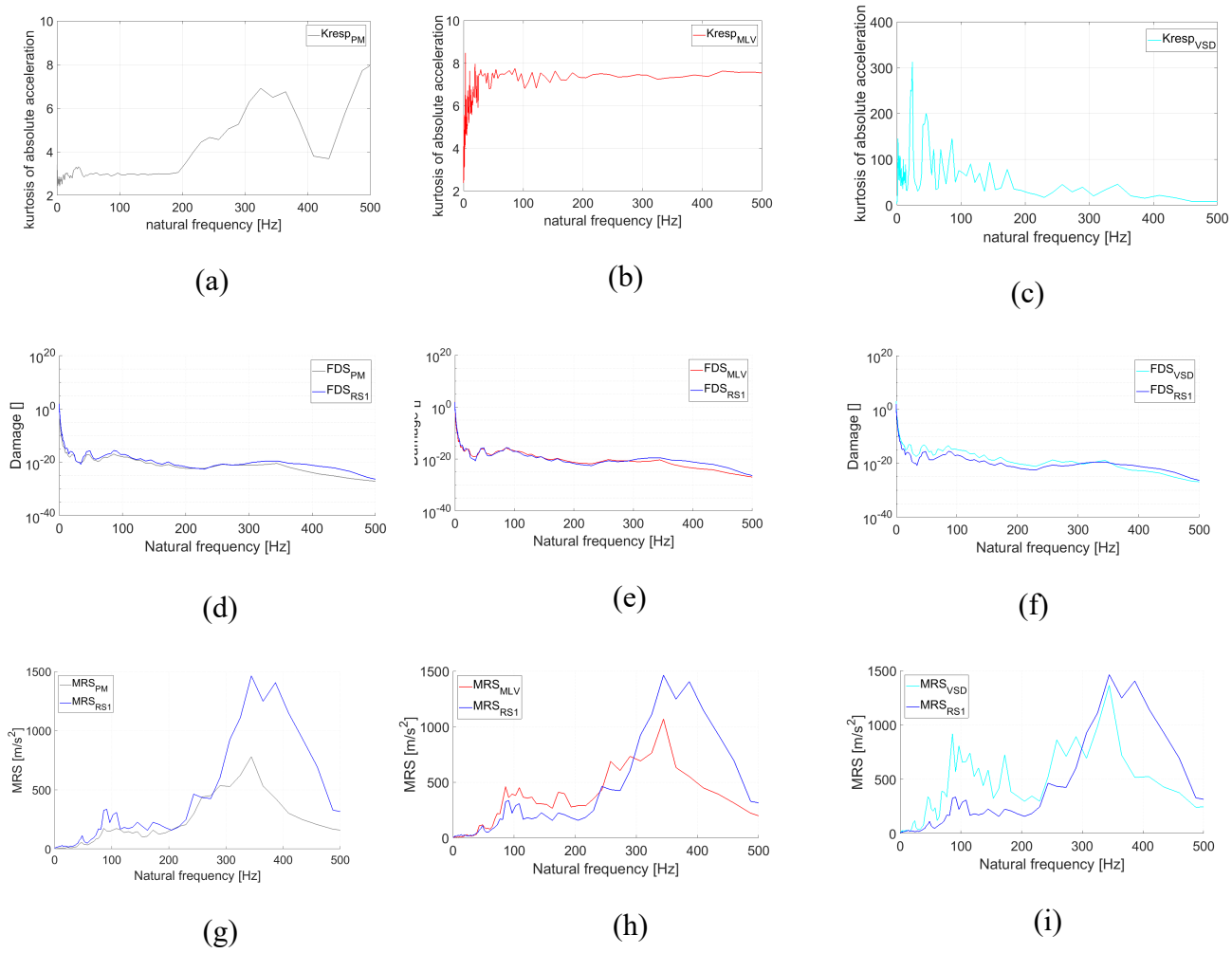

Figure 3.4: Synthesis results starting from the reference input profile *RS1*. Kurtosis of *SDOF* systems' responses, with $\zeta = 2\%$, to the signal synthesized by the: a) *PM*, b) *MLV*, c) *VSD* algorithms. *FDS* comparison, with $b = 6$ and $\zeta = 2\%$, between *RS1* and the: d) *PM*, e) *MLV*, f) *VSD* algorithms. *MRS* comparison, with $\zeta = 2\%$, between *RS1* and the: g) *PM*, h) *MLV*, i) *VSD* algorithms.

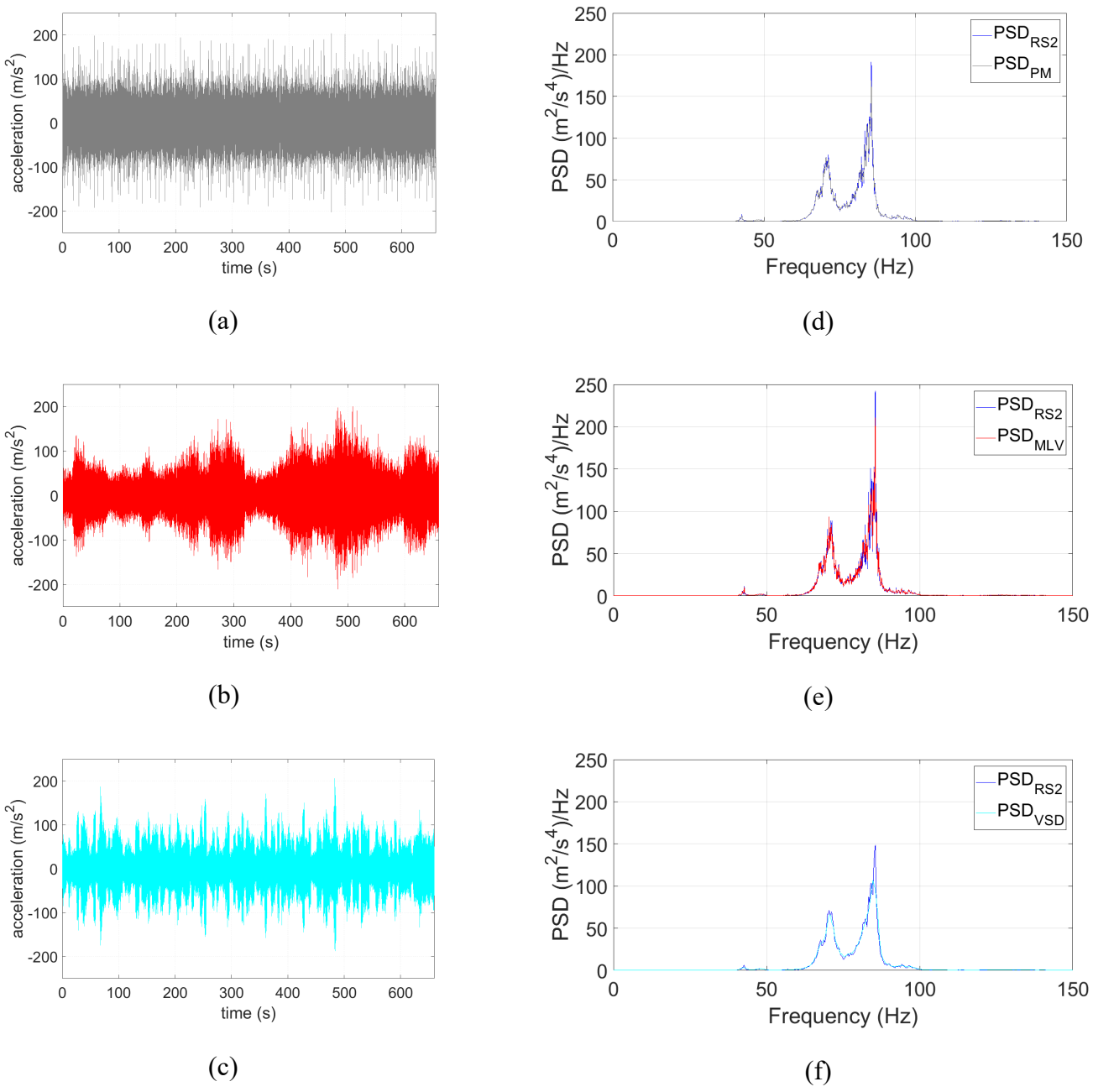

Figure 3.5: Synthesis results starting from the reference input profile *RS2*. Signal synthesized by the: a) *PM*, b) *MLV*, c) *VSD* algorithms. *PSD* comparison between *RS2* and the: d) *PM*. e) *MLV*, f) *VSD* algorithms.

Table 3.3: Statistical parameters of the signals synthesized starting from the reference input profile *RS2*

	PM signal	***MLV signal***	***VSD signal***
RMS $[\boldsymbol{m/s^2}]$	33.2	32.9	32.9
Kurtosis [-]	4.10	4.16	4.01
Crest factor [-]	6.14	6.38	6.25

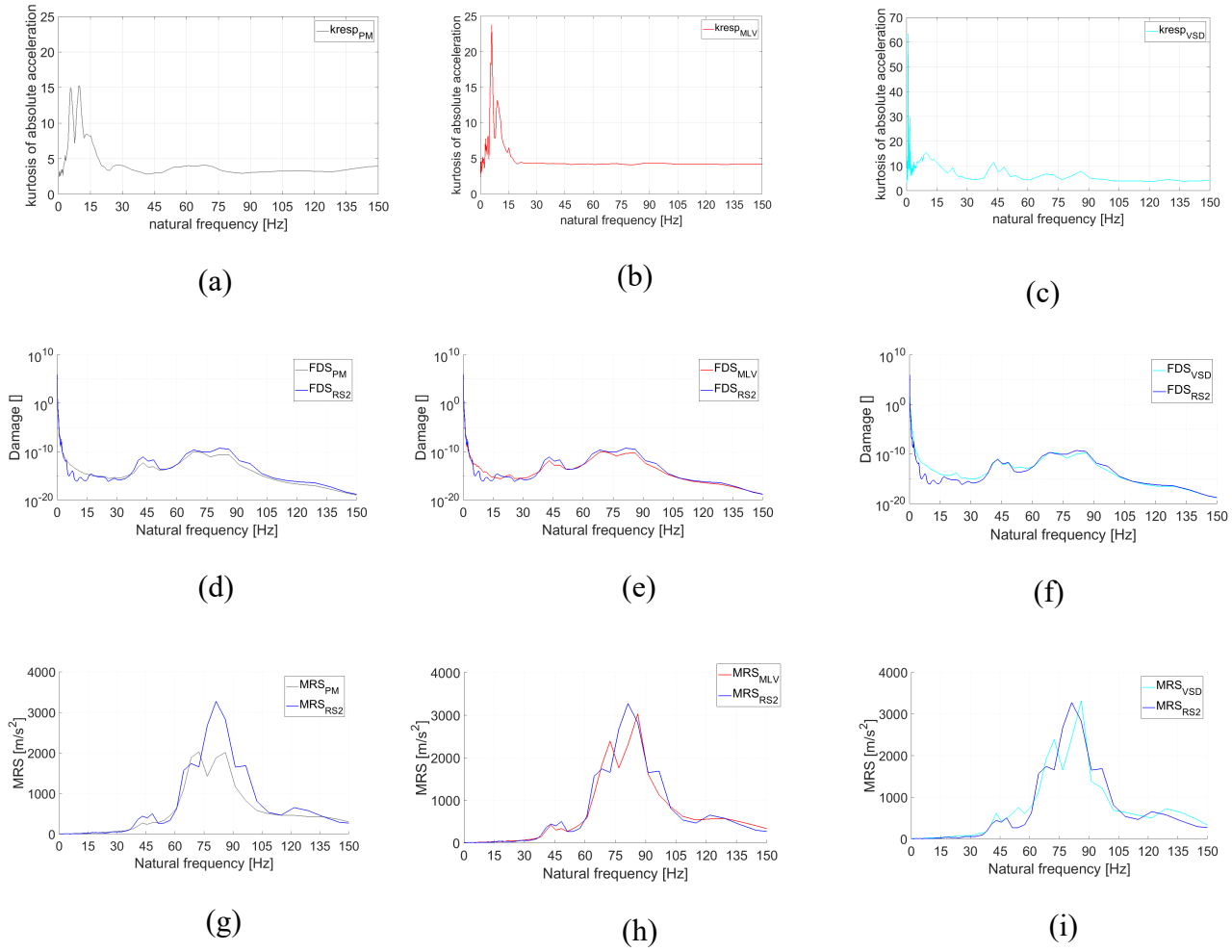

Figure 3.6: Synthesis results starting from the reference input profile *RS2*. Kurtosis of the *SDOF* systems' responses, with $\zeta = 2\%$, to the signal synthesized by the: a) *PM*. b) *MLV*, c) *VSD* algorithms. *FDS* comparison, with $b = 6$ and $\zeta = 2\%$, between *RS2* and the: d) *PM*, e) *MLV*, f) *VSD* algorithms. *MRS* comparison, with $\zeta = 2\%$, between *RS2* and the: g) *PM* algorithm, h) *MLV* , i) *VSD* algorithms.

3.1.1 Extension to durability tests

In this subsection, durability tests are considered. The test profiles are obtained through the filtering procedure described in section 2.1. In order to assess the filter's suitability to match the reference *FDS* and simultaneously affect the signals' characteristics as little as possible, a sizeable time reduction of the test would only amplify the difference between the original and filtered signals, making it harder to judge solely the filter's behavior. Therefore, the duration of the tests was chosen to be the same for both the reference and synthesized signals. The durability test profiles are obtained by means of the filtering procedure applied to the synthesized signals from section 3.1.
After filtering the signals obtained by considering the signal *RS1* as the reference (Fig.3.3a-c), the resulting profiles are plotted in Fig.3.7a-c, whereas their *PSD* are plotted in Fig.3.7d-f. Their statistical parameters are shown in Table 3.4.

The kurtosis values of the responses to the filtered signals are plotted versus the *SDOF* systems natural frequencies in Fig.3.8a-c. The *FDS* and *MRS* curves were computed with $b = 6$ and are plotted in Fig.3.8d-i. The frequency resolution of the *FDS* and *MRS* curves is logarithmic ($1/12^{th}$ of an octave).

In the case of the filtering procedure applied to the signal *RS2,* the durability test profiles obtained are plotted in Fig.3.9a-c and their *PSD* in Fig.3.9d-f. Their statistical parameters are shown in Table 3.5.

The kurtosis values of the responses to the filtered signals are plotted versus the *SDOF* systems' natural frequencies in Fig.3.10a-c. The *FDS* and *MRS* are computed with $b = 6$ in Fig.3.10d-i. The frequency resolution of the *FDS* and *MRS* curves is logarithmic ($1/12^{th}$ of an octave).

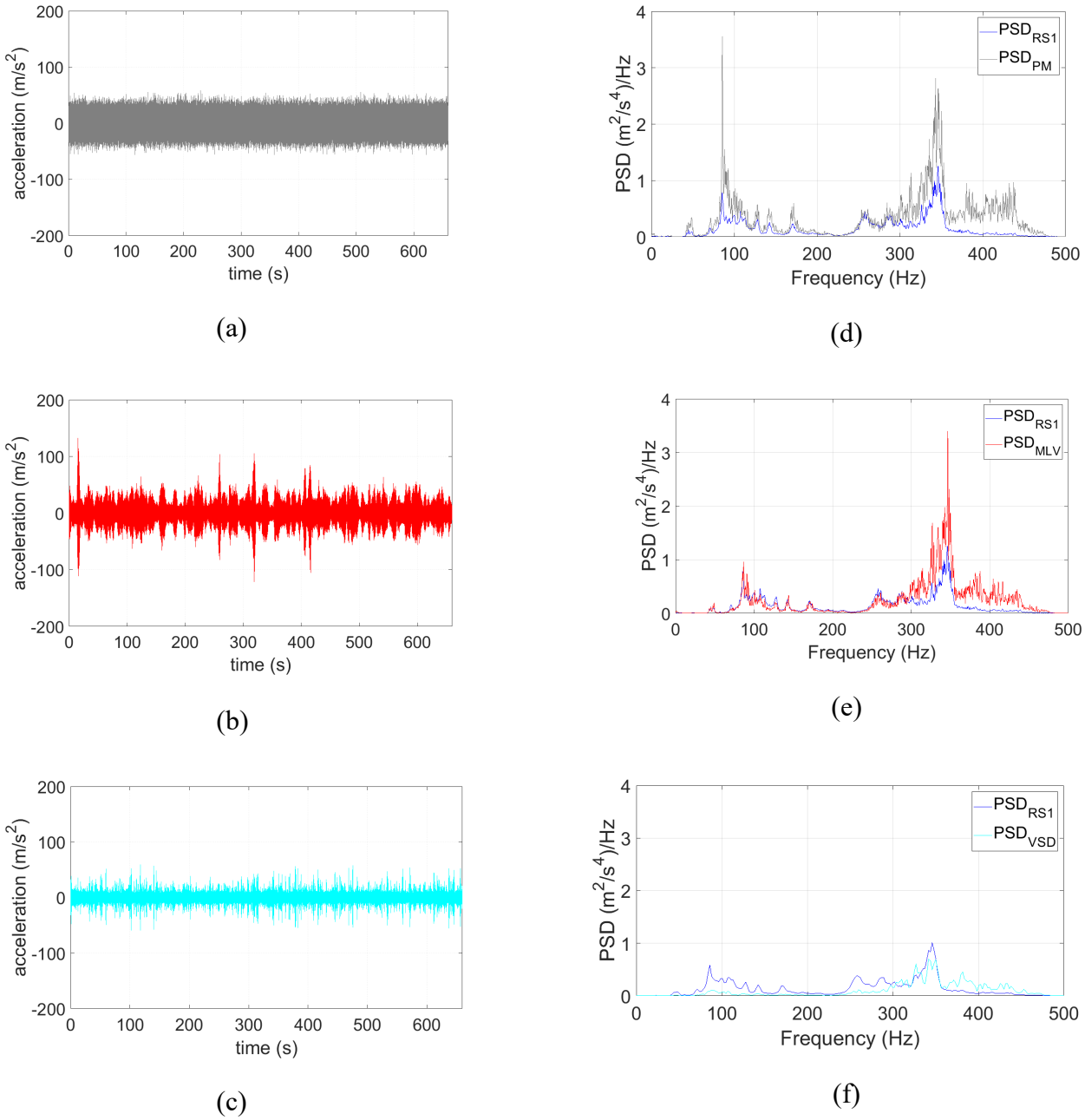

Figure 3.7: Synthesis results starting from the reference input profile *RS1*. Signal synthesized by the: a) *PM,* b) *MLV*, c) *VSD* algorithms, as they appear after filtering. *PSD* comparison between *RS1* and the: d) *PM*, e) *MLV*, f) *VSD* algorithms after filtering

Table 3.4: Statistical parameters of the signals synthesized starting from the reference input profile *RS1,* after the application of the filtering procedure that corrects the *FDS*

	PM signal	***MLV signal***	***VSD signal***
RMS $[\boldsymbol{m/s^2}]$	12.8	10.7	7.14
Kurtosis [-]	3.01	6.35	8.07
Crest factor [-]	4.55	12.3	8.28

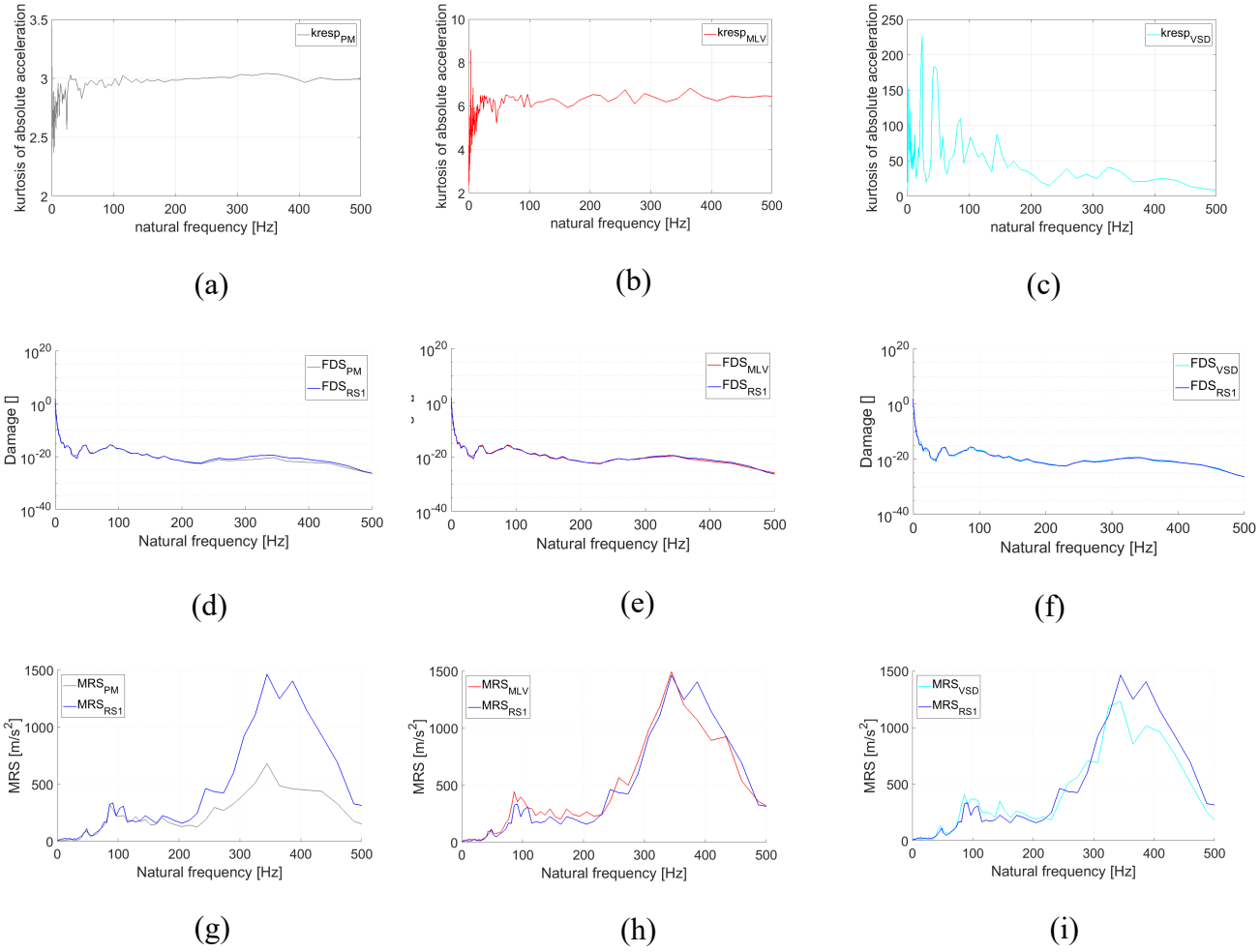

Figure 3.8: Synthesis results starting from the reference input profile *RS1*. Kurtosis of *SDOF* systems' responses, with $\zeta = 2\%$, to the signal synthesized by the: a) *PM*, b) *MLV*, c) *VSD* algorithms, after filtering. *FDS* comparison, with $b = 6$ and $\zeta = 2\%$, between *RS1* and the: d) *PM*, e) *MLV,* f) *VSD* algorithms after filtering. *MRS* comparison, with $\zeta = 2\%$, between *RS1* and the: g) *PM*, h) *MLV*, i) *VSD* algorithms after filtering.

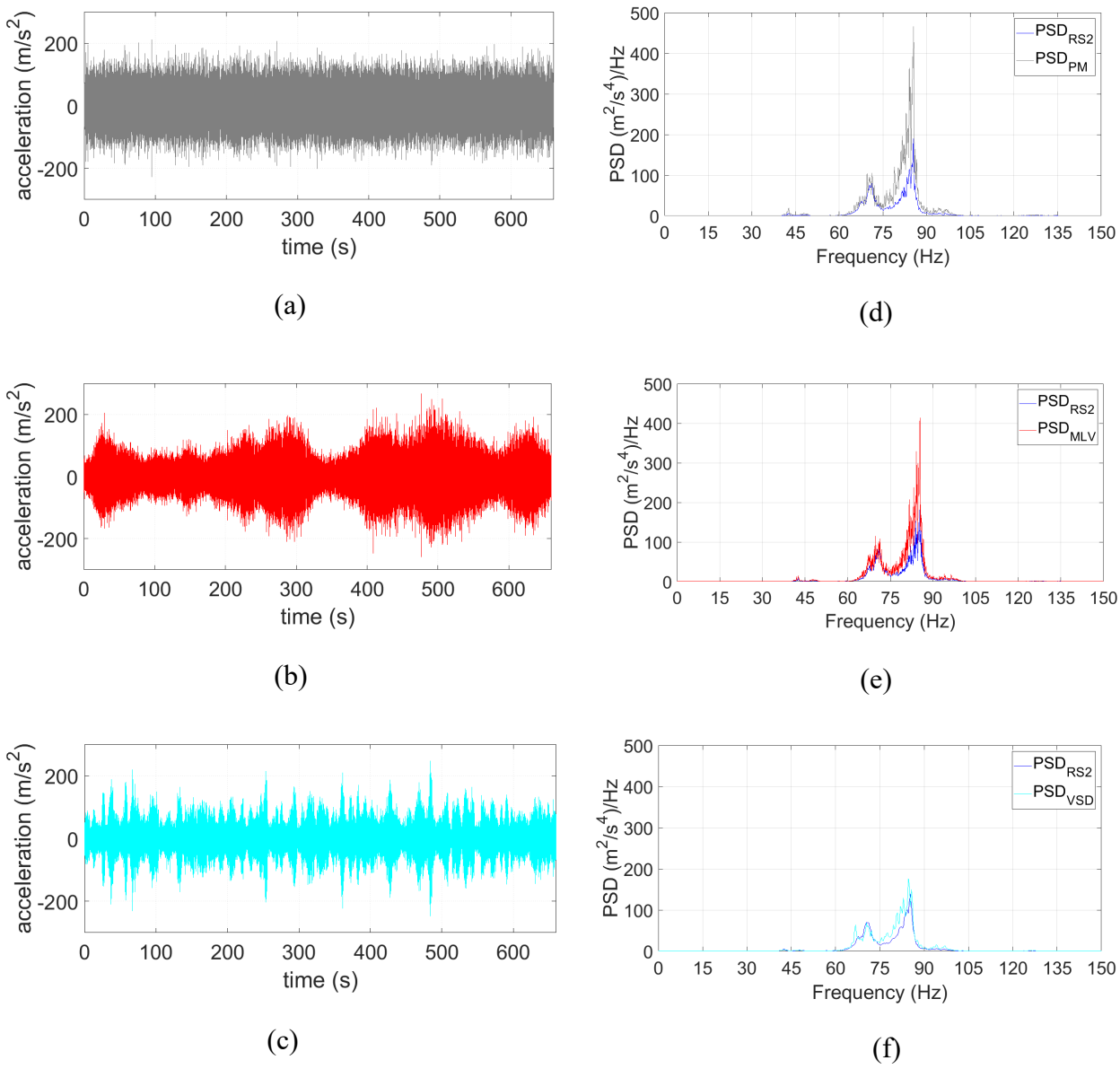

Figure 3.9: Synthesis results starting from the reference input profile *RS1*. Signal synthesized by the: a) *PM*, b) *MLV*, c) *VSD* algorithms after filtering. *PSD* comparison between *RS1* and the: d) *PM*, e) *MLV*, f) *VSD* algorithms after filtering.

Table 3.5: Statistical parameters of the signals synthesized starting from the reference input profile *RS2,* after the application of the filtering procedure that corrects the *FDS*

	PM signal	***MLV signal***	***VSD signal***
RMS $[\boldsymbol{m/s^2}]$	47.7	43.1	37.8
Kurtosis [-]	3.00	4.02	4.46
Crest factor [-]	4.42	6.20	6.54

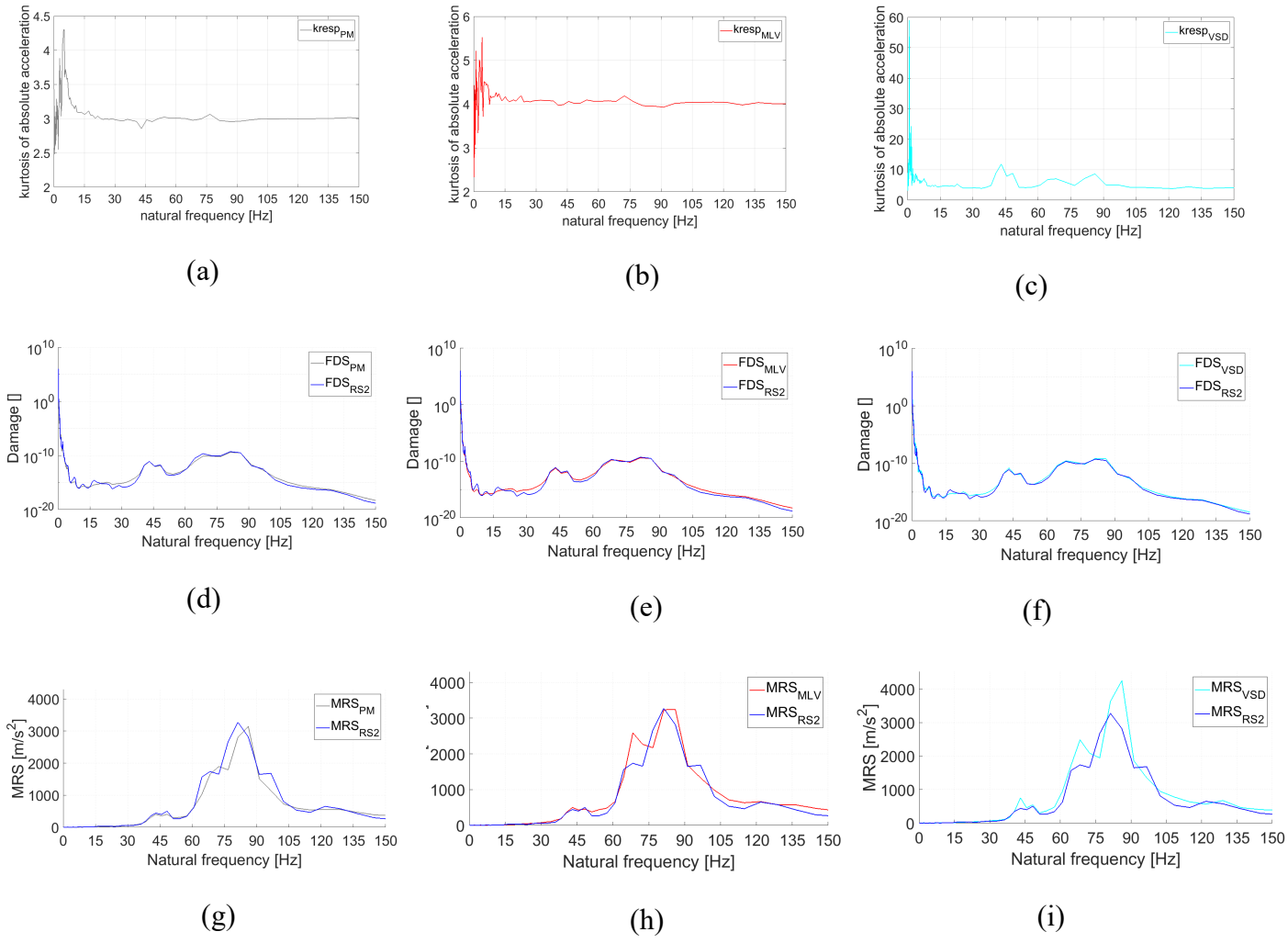

Figure 3.10: Synthesis results starting from the reference input profile *RS2*. Kurtosis of *SDOF* systems' responses, with $\zeta = 2\%$, to the signal synthesized by the: a) *PM*, b) *MLV*, c) *VSD* algorithms (all filtered). *FDS* comparison, with $b = 6$ and $\zeta = 2\%$, between *RS2* and the: d) *PM*, e) *MLV*, f) *VSD* algorithms after filtering. *MRS* comparison, with $\zeta = 2\%$, between *RS2* and the: g) *PM*, h) *MLV*, i) *VSD* algorithms after filtering.

3.1.2 Discussion

As it can be observed from Fig.3.4a and Fig.3.6a, the kurtosis values of the responses to the signals synthesized by the *PM* algorithm are close to 3 in a wide range of frequencies; this suggests that Papoulis' Rule may hamper the algorithm effectiveness, thus the high peaks present in the input signal may be filtered out by the *SDOF* system. As it can be observed from Fig.3.4b and Fig.3.6b, the kurtosis values of the responses to the signals synthesized by the *MLV* algorithm are closer to the kurtosis of the reference input profile (except at low frequencies), whereas the kurtosis of the responses to the signals synthesized by the *VSD* algorithm can take much larger values (Fig.3.4c and Fig.3.6c). These values highlight an important difference between the *MLV* and *VSD* algorithms: the *VSD* algorithm can generate signals whose system response has a (much) higher kurtosis than the input one. This is the reason why the reference signal *RS1* has been considered particularly significant to illustrate the special feature of the *VSD* algorithm. In fact, as it can be observed from Fig.3.2a, the kurtosis values of the system responses are higher than those of the input excitation. This is due not

only to the variation of the variance of the signal over time, but mainly to the variation of the PSD. The high kurtosis values of the responses are due to a resonance effect: in particular, some blocks of the reference signals present a sharp PSD around the natural frequency of one of the *SDOF* systems. This implies that in those blocks the signal is approximately a sinusoid with the same frequency as the system, causing the system to resonate. Unlike the VSD algorithm, the resonance effect does not occur by using the MLV algorithm, because all the blocks of the signal have the same *PSD* shape and a wide band (the same as the reference signal's overall *PSD*).

The resonance effect may be used effectively also in the *PM* algorithm: the main problem of phase selection is that, especially if the phases are manipulated in a wide range of frequencies, the high peaks are easily filtered because of their sparsity and therefore cannot excite the system long enough for it to respond with correspondingly high excursions.

There is still an alternative way of selecting the phases such that Papoulis' Rule does not negatively affect the PM algorithm, in the case of only a narrow band being of interest. The idea is to change the phases in a small interval in the narrow band, in order to align those harmonics with frequencies in that range so that they constructively interfere. Their interference generates high peaks whose frequencies are contained in the narrow band of interest, thus capable of making a system with frequencies reasonably close to the band resonate[17].

As regards the MLV algorithm, one can motivate why the kurtosis computed for the responses of the excited *SDOF* linear systems has relatively small fluctuations around a value close to the excitation signal kurtosis (see Fig.3.4b and Fig.3.6b). In fact, as already hinted at, the blocks constituting the synthesized signal all have a wide-band *PSD*, so that unexpected resonant effects are unlikely to occur. However, one should note that the setup parameters might significantly affect the results. In particular, if the bursts' duration is not long enough, the system may not have time to respond, thus preventing high excursions to appear in the response (as is the case for the *PM* algorithm).

Finally, it is worth recalling that randomness in the synthesized profiles is guaranteed since the algorithms: (i) manipulate only some of the phases (*PM* algorithm), (ii) randomly generate the modulating function and manipulate the phases of only one block (MLV algorithm), (iii) randomly generate the phases, as well as randomly vary the *PSD* over time (VSD algorithm). Different runs of the algorithms– with unchanged setup parameters –provide the synthesis of different profiles (all complying with the target *PSD* and kurtosis).

From the observation of Fig.3.4d-f and Fig.3.6d-f, it is clear that the three kurtosis control algorithms could lead to signals with markedly different *FDS* curves from that of the excitation (note that the y axis is reported in logarithmic scale), since they do not directly control the *FDS*. If the Mission Synthesis is performed for durability testing purposes, the filter proposed by Kihm et al. [34] can be effectively applied to correct the *FDS* of the signals generated by the algorithms.

As shown by Figs.(3.7-3.10) presented in subsection 3.1.1, the filtered MLV and VSD signals feature similar Leptokurtic distributions as their unfiltered versions, with some differences – due to the filter action – observed in the *PSD*s and the statistical parameters. On the other hand, the filtered *PM* signal is close to Gaussian, showing no difference with respect to the standard methodology that synthesizes Gaussian signals in (accelerated) fatigue life tests.

The combination of the *VSD* algorithm with the subsequent *FDS* correction appears particularly promising whenever the loads acting on the shaker are required to be as low as possible, compatibly with the *FDS* specification and duration of the test. In fact, the synthesized excitations are

[17] For example, Fig.3.4a exemplifies this statement in the relatively "narrow" band [200 Hz, 400 Hz], where the phases were manipulated. Outside of that bandwidth, in the interval [0 Hz, 200 Hz], Papoulis' Rule seems to affect output kurtosis more severely than in the case of the other algorithms. On the other hand, for those intervals containing frequencies which are higher than 400 Hz, the system becomes more responsive, therefore the response kurtosis resumes values which are closer to input's kurtosis.

characterized by a relatively low *RMS* value (Tables 3.4 and 3.5), but still able to generate responses with (noticeably) high kurtosis (i.e. with high amplitude peaks) and with the prescribed *FDS*, therefore subjecting the shaker to moderate loads. However, the high peaks in the response might as well constitute a non-negligible problem shifting the type of failure from fatigue-related to yield-related; therefore, all pros and cons should be evaluated with caution.
In general, the filtering technique proposed by Kihm et al. increases the *RMS* value (i.e. the energy) of the signal the more the duration of the test decreases.

3.2 Durability tests with a priori *FDS* control

In section 3.1 two reference signals were considered. Nevertheless, for the sake of conciseness, in this section only one reference signal is chosen to display results, from which considerations could be drawn without loss of generality.
The reference profile, sampled at 500 Hz with a duration of 287 s, is shown in Fig.3.11. The life of the component to be tested is supposed to be 2300 h, which implies that the signal is considered to be replayed approximately 28850 times.
At first no time reduction factor is applied, which implies the same duration as the component's life (2300 h) for the output signals. Due to memory limitations, the duration of the synthesized signals was automatically limited to approximately 4.44 h by the *kFDS* and *RF* algorithms and to 2.246 h by the *PF* and *PSF* (for reasons due to their implementations), with the signals considered to be replayed until 2300 h are reached (518 and 1024 times respectively).
The following values of the parameters are chosen:

- $b = 7$ (constant related to the slope of Wohler's curve)
- $\zeta = 2.5\%$ (damping coefficient of the *SDOF* system model considered)

The frequency range for the calculation of the *FDS* is chosen to be from 5 to 250 Hz with a constant resolution of 0.5 Hz and the same resolution is used in the calculation of the *PSD*. The reference's and the synthesized signals' *FDS* curves are calculated in the time domain.
In the following, four different plots are shown for each of the four algorithms presented. Let *X* be a number equal to an integer between 12 and 15 (with 12 and 15 included). When reference is made in this section to "algorithm *X*": algorithm 12 represents the *kFDS* algorithm, algorithm 13 the *RF* algorithm, algorithm 14 the *PF* algorithm and algorithm 15 the *PSF* algorithm.
Fig.3.*X*a shows the plot of the time-series synthesized by algorithm *X*; in order to appreciate some of the details better, only the first 2500 s are shown. Fig.3.*X*b shows its corresponding *PSD* versus that of the reference signal, whereas Fig.3.*X*c shows the corresponding *FDS* versus that of the reference signal. Finally, Fig.3.*X*d shows the kurtosis of the system response to the synthesized signal versus that to the reference signal, plotted in the frequency range 5-250 Hz with $1/12^{th}$ of an octave resolution.
Some statistical parameters of the reference and the synthesized signals are shown in Table 3.6.
In Fig.3.16 the *MRS* curves of the four algorithms are plotted together with the *MRS* of the reference signal of Fig.3.11.

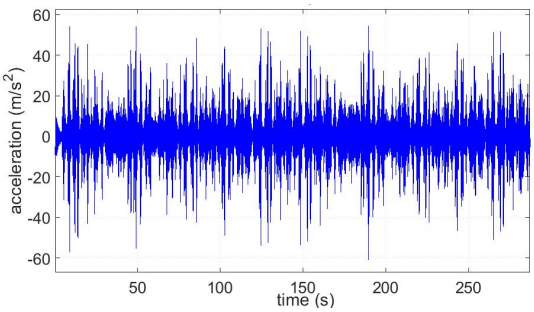

Fig.3.11: reference signal

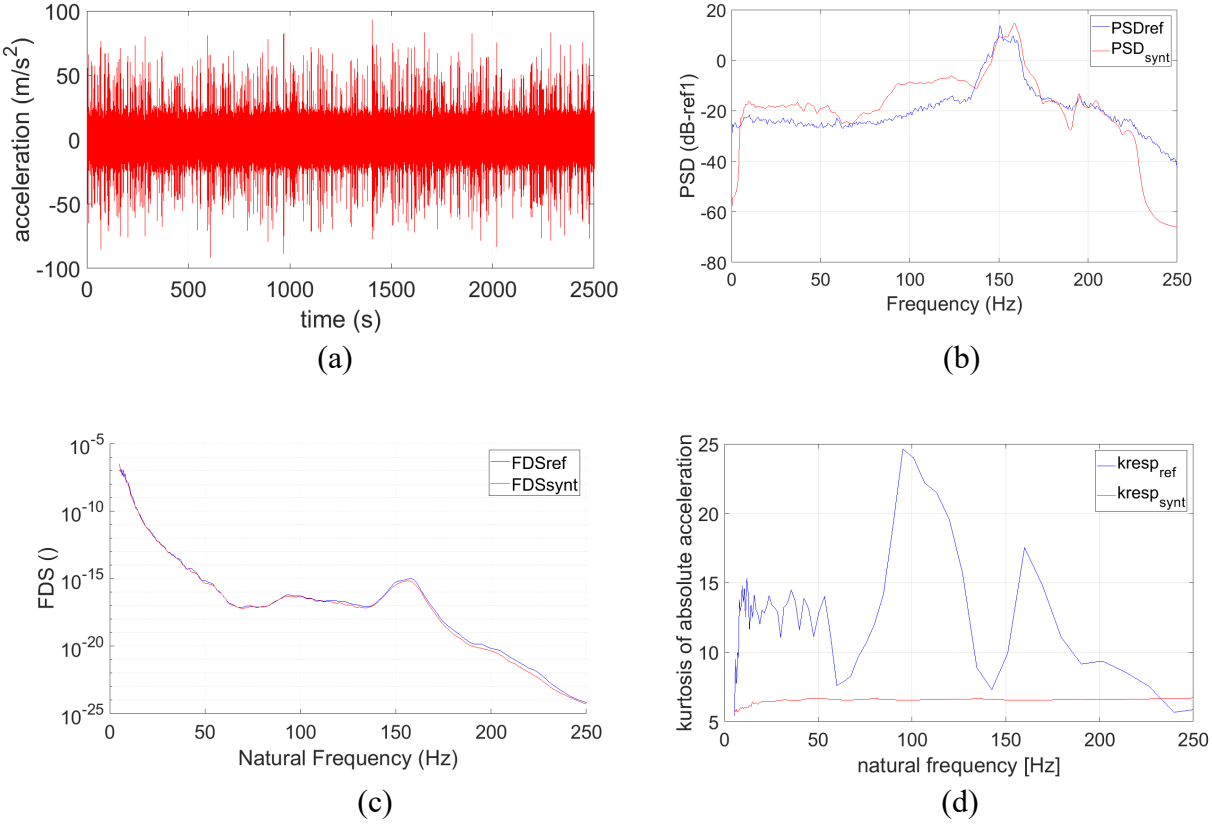

Fig.3.12: a) signal synthesized by the *kFDS* algorithm; b) *PSD* of the synthesized signal vs reference *PSD*; c) *FDS* of the synthesized signal vs reference *FDS*; d) kurtosis of the response to the synthesized signal vs kurtosis of the response to the reference signal

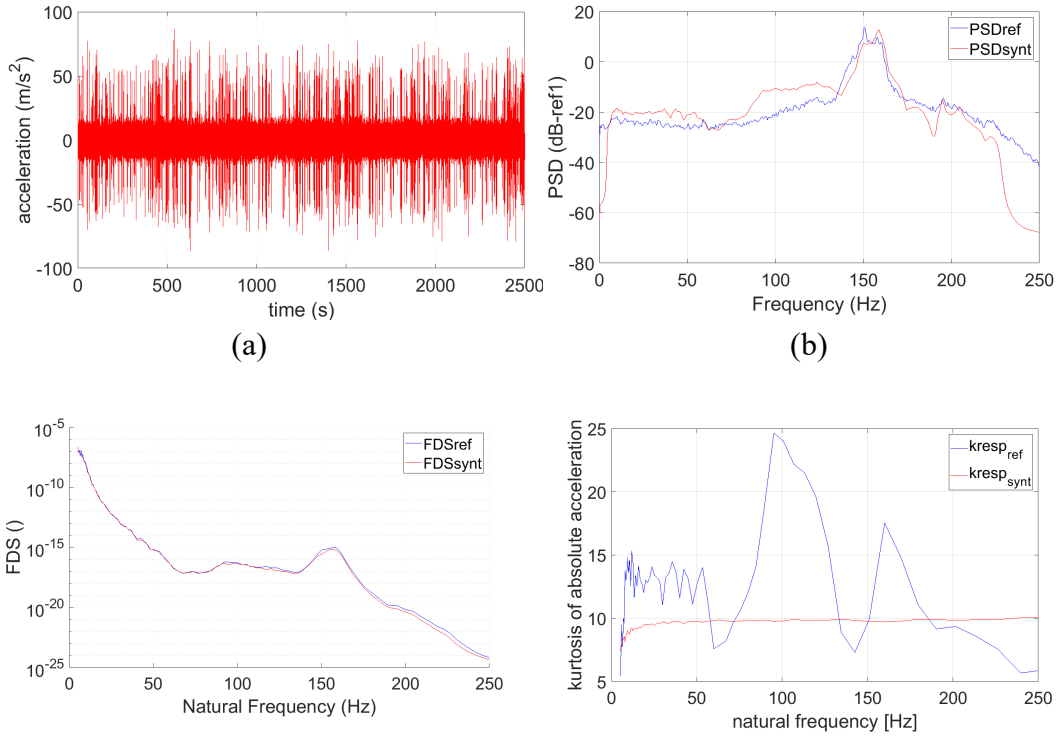

Fig.3.13: a) signal synthesized by the *RF* algorithm; b) *PSD* of the synthesized signal vs reference *PSD*; c) *FDS* of the synthesized signal vs reference *FDS*; d) kurtosis of the response to the synthesized signal vs kurtosis of the response to the reference signal

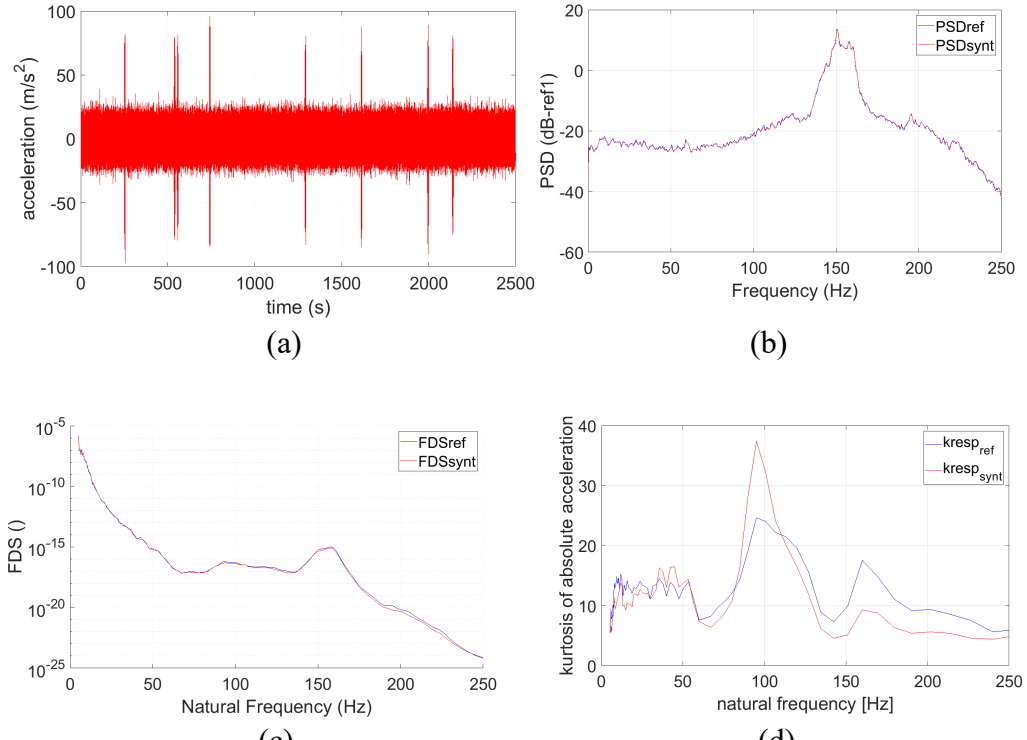

Fig.3.14: a) signal synthesized by the *PF* algorithm; b) *PSD* of the synthesized signal vs reference *PSD*; c) *FDS* of the synthesized signal vs reference *FDS*; d) kurtosis of the response to the synthesized signal vs kurtosis of the response to the reference signal

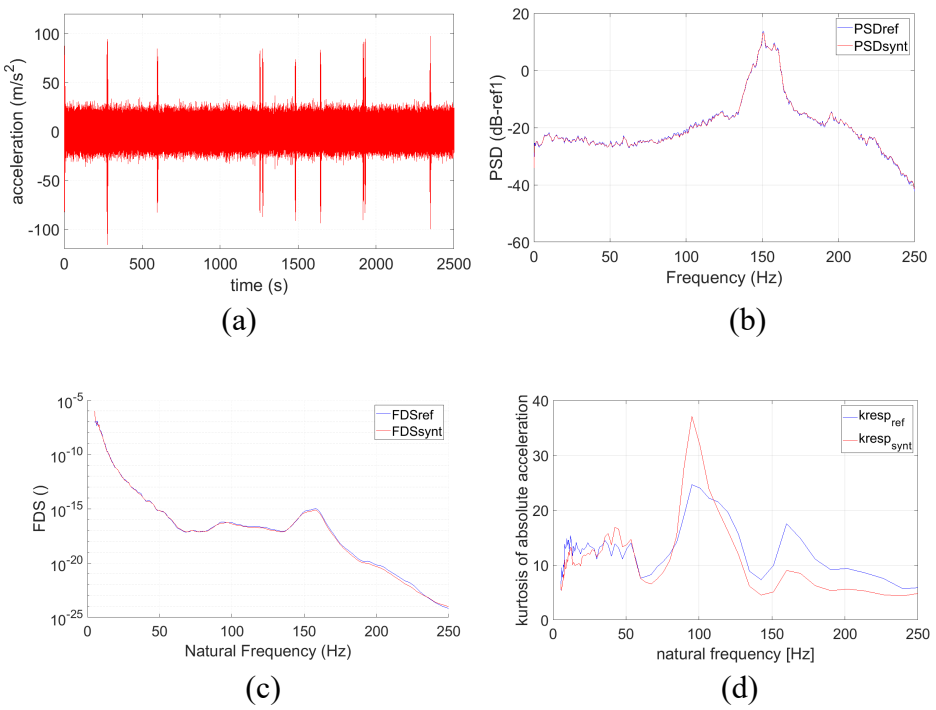

Fig.3.15: a) signal synthesized by the *PSF* algorithm; b) *PSD* of the synthesized signal vs reference *PSD*; c) *FDS* of the synthesized signal vs reference *FDS*; d) kurtosis of the response to the synthesized signal vs kurtosis of the response to the reference signal

Table 3.6: Time-domain characteristics of the reference and synthesized signals

	Reference signal	***kFDS***	***RF***	***PF***	***PSF***
RMS $[\boldsymbol{m/s^2}]$	8.41	9.81	8.72	8.41	8.41
Kurtosis [-]	6.52	6.54	9.75	7.16	7.08
Crest factor [-]	7.26	10.3	12.6	12.1	13.8
Signal Duration $[\boldsymbol{s}]$	287	15985	15985	8086	8086
replays	28850	518	518	1024	1024

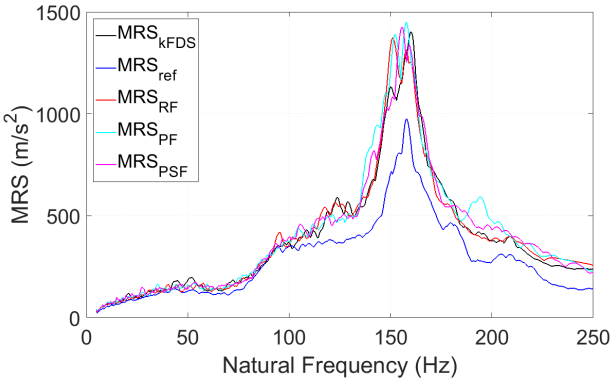

Fig.3.16: *MRS* curves of the algorithms compared with that of the reference signal

In the case of accelerated tests, the same reference signal as the one displayed in Fig.3.11 is chosen to display results.
The life of the component to be tested is still supposed to be 2300 h, which implies that the signal is considered to be replayed approximately 28850 times.
In order to show the effects of time reduction, a factor of 5 is used, implying a duration of 460 h of the synthesized signals. Due to memory limitations, the duration of 460 h was automatically limited to approximately 4.423 h by the *kFDS* and *RF* algorithms and to 3.594 by the *PF* and *PSF*, with the signals considered to be replayed until 460 h are reached (104 and 128 times respectively).
The following values of the parameters are chosen:

- $b = 7$
- $\zeta = 2.5\%$

The frequency range for the calculation of the *FDS* is chosen to be from 5 to 250 Hz with a constant resolution of 0.5 Hz and the same resolution is used in the calculation of the *PSD*. The reference's and the synthesized signals' *FDS* curves are calculated in the time domain.
In the following, four different plots are shown for each of the four algorithms presented. Let now *X* be a number equal to an integer between 17 and 20 (with 17 and 20 included). When reference is made in the next part of this section to "algorithm *X*": algorithm 17 represents the *kFDS* algorithm, algorithm 18 the *RF* algorithm, algorithm 19 the *PF* algorithm and algorithm 20 the *PSF* algorithm.
As in the case of non-accelerated tests, Fig.3.*X*a shows the plot of the time-series synthesized by algorithm *X*; in order to appreciate some of the details better, only the first 2500 s are shown. Fig.3.*X*b shows its corresponding *PSD* versus that of the reference signal, whereas Fig.3.*X*c shows the corresponding *FDS* versus that of the reference signal. Finally, Fig.3.*X*d shows the kurtosis of the system response to the synthesized signal versus that to the reference signal, plotted in the frequency range 5-250 Hz with 1/12th of an octave resolution.
Some statistical parameters of the reference and the synthesized signals are shown in Table 3.7.
In Fig.3.21 the *MRS* curves of the four algorithms are plotted together with the *MRS* of the reference signal of Fig.3.11.

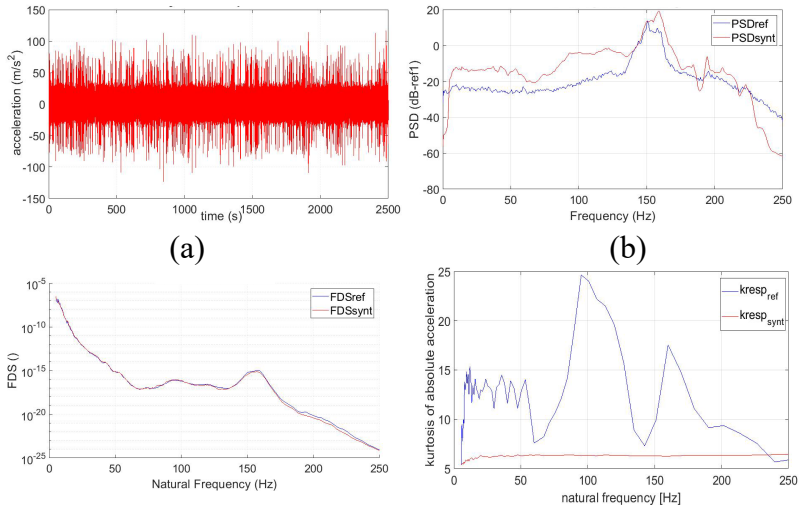

Fig.3.17: (a) signal synthesized by the *kFDS* algorithm; (b) *PSD* of the synthesized signal vs reference *PSD*; (c) *FDS* of the synthesized signal vs reference *FDS*; (d) kurtosis of the response to the synthesized signal vs kurtosis of the response to the reference signal

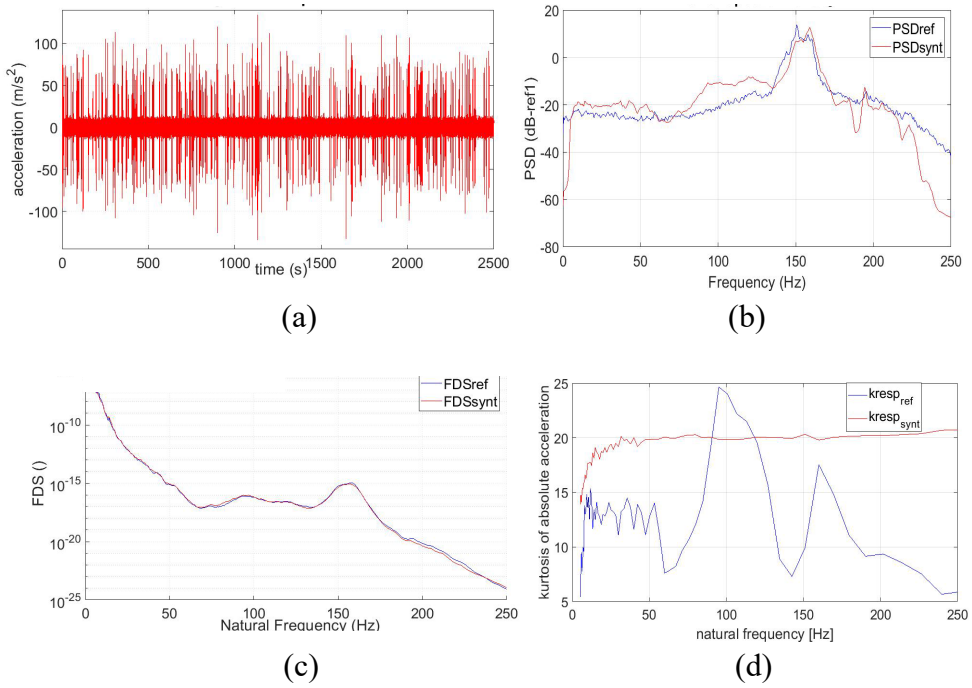

Fig.3.18: (a) signal synthesized by the *RF* algorithm; (b) *PSD* of the synthesized signal vs reference *PSD*; (c) *FDS* of the synthesized signal vs reference *FDS*; (d) kurtosis of the response to the synthesized signal vs kurtosis of the response to the reference signal

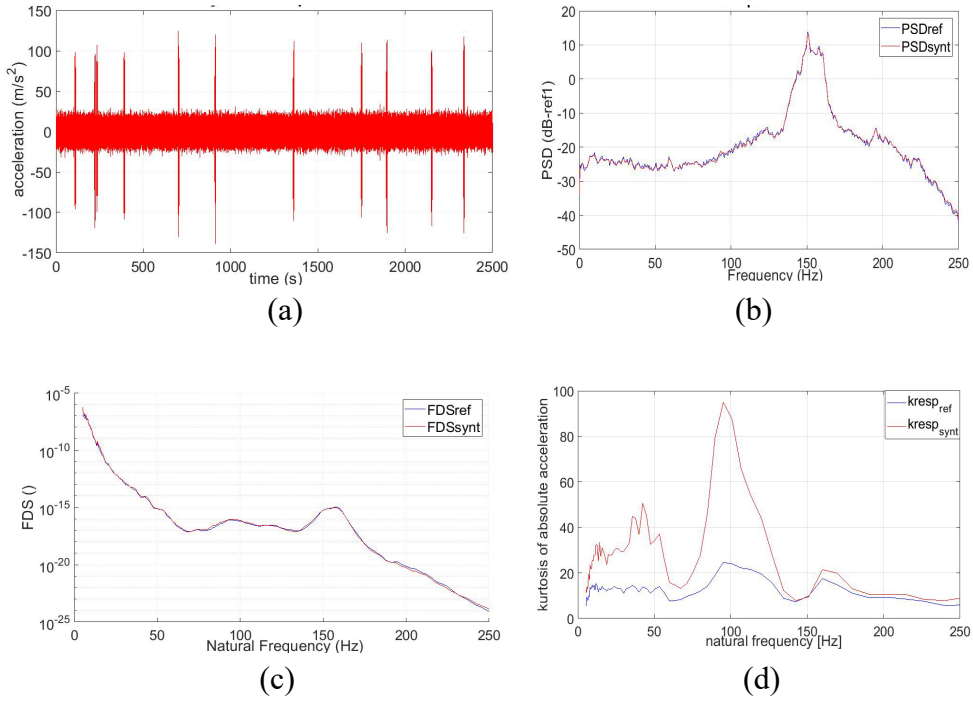

Fig.3.19: (a) signal synthesized by the *PF* algorithm; (b) *PSD* of the synthesized signal vs reference *PSD*; (c) *FDS* of the synthesized signal vs reference *FDS*; (d) kurtosis of the response to the synthesized signal vs kurtosis of the response to the reference signal

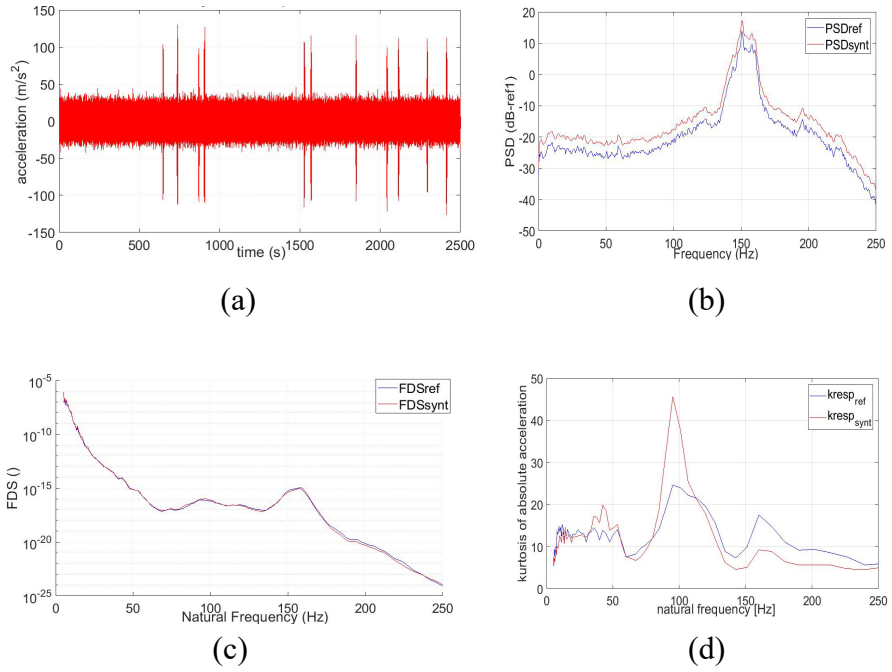

Fig.3.20: (a) signal synthesized by the *PSF* algorithm; (b) *PSD* of the synthesized signal vs reference *PSD*; (c) *FDS* of the synthesized signal vs reference *FDS*;(d) kurtosis of the response to the synthesized signal vs kurtosis of the response to the reference signal

Table 3.7: Time-domain characteristics of the reference and synthesized signals

	Reference signal	***kFDS***	***RF***	***PF***	***PSF***
RMS $[\boldsymbol{m/s^2}]$	8.41	12.7	8.66	8.42	10.6
Kurtosis [-]	6.52	6.28	19.9	15.4	7.35
Crest factor [-]	7.26	11.4	17.2	18.3	14.6
Signal Duration $[\boldsymbol{s}]$	287	15923	15923	12932	12932
replays	28850	104	104	128	128

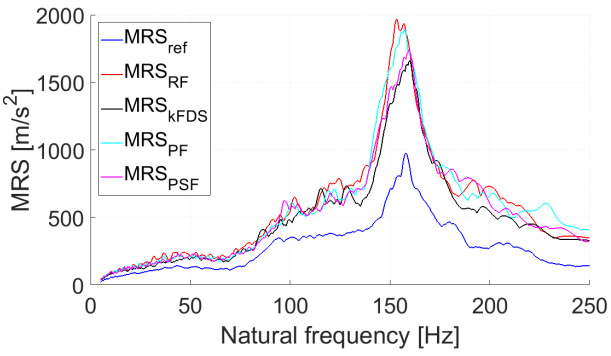

Fig.3.21: *MRS* curves of the algorithms compared with that of the reference signal

3.2.1 Discussion

The results in section 3.2 show a precise match between the reference's and the synthesized signals' *FDS*, even more precise than the matching obtained in subsection 3.1.1. Moreover, the distribution of the generated time-series is Leptokurtic and not Gaussian, thus generalizing standard procedures.
It must be highlighted that when the test duration is reduced, before performing actual tests on specimens, the maximum values of the system response (in terms of either displacement or velocity or acceleration) should be checked, in order to assess whether the type of failure is still fatigue related and not due to exceeding the yield strength of the material. This assessment was carried out by plotting the *MRS* associated with the profiles synthesized by the different algorithms. As regards the non-accelerated tests, the *MRS* of the synthesized profiles are higher in some frequency ranges. However, one should note that the synthesized profiles were several hours long compared with the 287 s duration of the reference profile; this definitely affects the *MRS* since the longer the duration, the more likely it is to find higher peaks. Besides, the *MRS* may also be affected by the non-stationarity of the reference profile's distribution; this aspect highlights the importance of choosing reference vibrations that are representative of the application.
Because of the large difference in duration between the synthesized and reference profile, the amount by which the *MRS* of the synthesized profile exceeds the *MRS* of the reference profile is not of great concern. When the duration of the test is the same as the life of the *DUT*, it is usually the case that the *MRS* of a synthesized signal is more or less of the same order of magnitude as the reference's *MRS*. In order to exemplify the dependence of the *MRS* upon the duration of the signal, the reference signal's *MRS* is compared with that of a signal synthesized by the *kFDS* algorithm in Fig.3.22, with the duration of the synthesized signal being the same as that of the reference signal (about 287 s). It is evident that the two curves are closer this time, and it is also noteworthy to point out that the randomness of the algorithm and the choice of the algorithm itself (in this case the *kFDS*), might produce different results even with the same input parameters.
Also in the case of accelerated tests, the amount by which the *MRS* of the synthesized profiles exceed the *MRS* of the reference profile is partly explained by the large difference in duration between the synthesized and reference profiles. Nevertheless, because there is a time reduction factor of 5 applied to reduce the test duration, the *MRS* associated with the synthesized profiles increase with respect to the ones shown in Fig.3.16. It should be noted that the increase in the *MRS* is much less than the time reduction factor of 5; in fact, the points in the vicinity of the maxima of the curves are about just 1.4 times higher than the corresponding ones where no acceleration of the tests is performed. This suggests that in the case shown, the test had the potential to be accelerated. This is the case for many practical applications: often, there are periods of time when the loads are below a threshold such that no amount of damage accumulates; therefore, if these periods are extracted from the signal the test would become conceptually and automatically accelerated. The main problem is that it is usually not easy to determine these low amplitude loads and whether or not they can be considered to be below the fatigue limit.
Besides controlling precisely the *FDS* and other parameters such as: *RMS, PSD* shape, kurtosis, depending on the algorithm selected, it can be observed that another characteristic is that, for the *kFDS* and *RF* algorithms, the kurtosis of the linear system's response is relatively constant when plotted against natural frequency. This is not the case for the *PF* and *PSF* algorithms, where the shape of the curve becomes closer to that of the reference signal. In general, as already discussed, this occurs when the *PSD* of the signals changes not only in scale but also in shape over time, and this happens

only for the *RF* and *PSF* algorithms. When signals are synthesized by modulation (as is the case for *kFDS* and *RF*), the response kurtosis curve remains relatively flat because every block is wide-banded, therefore there is no possibility that some may cause greater bursts in the responses due to resonance as it may occur in the case of the *RF* and *PSF* algorithms.
The algorithms that control the *RMS* and/or the *PSD* shape, namely the *RF* and the *PF,* might cause greater bursts in the response than the *kFDS* and the *PSF* algorithms, especially when the test duration is reduced. This suggests a greater sensitivity to the Wohler's curve slope (related to parameter b) on the part of the *RF* and the *PF* algorithms, which might make it more difficult to carry out reliable tests, mainly because of the uncertainty on the value of b. Besides, since the *PSF* and *PF* algorithms only allow of two energy levels in the synthesized signals, the amount of randomness that can be generated is less than in the case of the *kFDS* and the *RF* algorithms. According to these considerations, the most promising algorithm among the ones proposed is the *kFDS,* which was therefore chosen in the experimental campaign described in the next chapter.
For the sake of convenience, Table 3.8 concisely lists some of the possible uses that can be made of the algorithms proposed in this work.

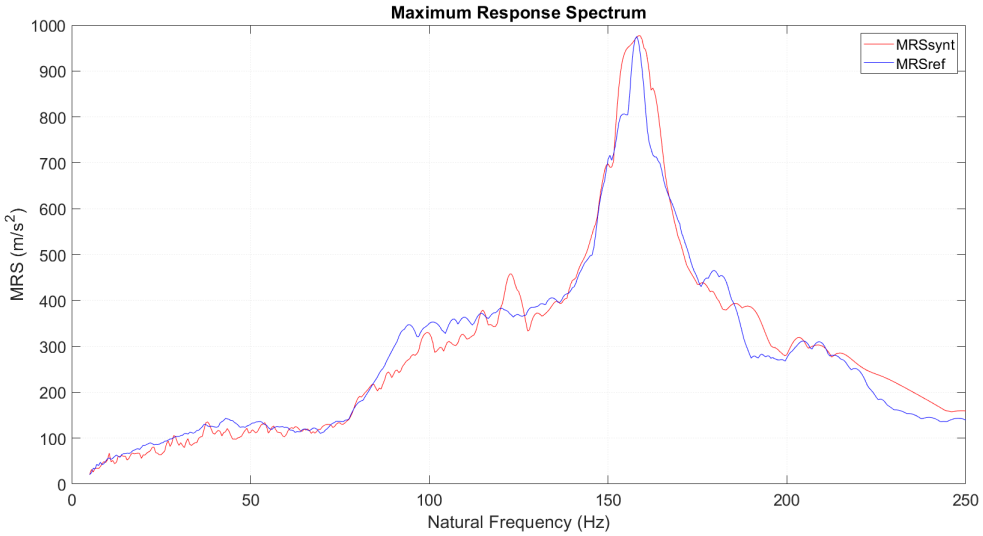

Fig.3.22: *MRS* curves of a signal synthesized by the *kFDS* algorithm compared with that of the reference signal. No time reduction is applied: the duration of the synthesized signal is the same as that of the reference signal

Table 3.8: some of the possible uses that could be made of both the kurtosis control algorithms and of those aimed at durability tests.

Kurtosis control	*PM*	Suitable for: (i) qualification tests, (ii) maximizing randomness for the entire test duration by avoiding signal replications. In fact, even if the waveform replication mode is used, the algorithm can synthesize a signal having any desired duration in principle. Not suitable for: (i) durability tests, (ii) properly transferring input kurtosis through to the output, since easily affected by Papoulis' Rule.
	MLV	Suitable for: (i) qualification tests, (ii) maximizing randomness for the entire test duration by avoiding signal replications, (iii) controlling the output burst level. Not suitable for durability tests.
	VSD	Suitable for: (i) qualification tests, (ii) maximizing randomness for the entire test duration by avoiding signal replications, (iii) a wise employment of the shaker by minimizing the current intensity level required (possible resonance effects) to achieve high kurtosis at the output. Not suitable for durability tests.
Extension to durability tests	*MLV* after filtering	Suitable for: (i) durability tests with Leptokurtic signals, (ii) controlling the output burst level.
	VSD after filtering	Suitable for: (i) durability tests with Leptokurtic signals, (ii) minimizing the current intensity level of the shaker to match a prescribed *FDS*.
Algorithms aimed at durability tests	*kFDS, RF, PF* and *PSF*	Suitable for durability tests with Leptokurtic signals thanks to a more precise *FDS* match than the extended kurtosis control algorithms.

4 Experimental tests

The purpose of this chapter is to describe (more specifically in sections 4.1 and 4.2) how the experimental test rig was set up, in terms of: choice of the material used, design of the specimens and the fixture, characteristics of the shaker and software, choice of relevant synthesis parameters such as the coefficients ζ and b. The experimental campaign is finally addressed in section 4.3, in which non-accelerated tests are treated, whereas accelerated tests are handled in section 4.4. The ultimate aim of this work is to verify whether the novel algorithms presented might constitute a tangible improvement of the already available standard procedure. Therefore, sections 4.3 and 4.4 represent the core of the chapter.

4.1 Design of experiment

The design of experiment (*DOE*) considered a series of factors, among which:

- the choice of one reference profile to be used as the benchmark in all synthesis procedures;
- the choice of the material, the geometry and dimensions of the specimen;
- the fixture to be used to fix the specimens to the shaker.

4.1.1 Reference profile

The measured signal shown in Fig.3.11, adopted as reference profile in Section 3.2, was targeted as particularly appropriate to cast light onto the possible critical aspects of the standard Mission Synthesis, mainly due to its non-stationary spectrum. In addition, its *PSD* presents the highest values in a bandwidth (about 155-160 Hz) which is not very narrow. However, two significant alterations were required for the experimental testing feasibility. Firstly, in spite of the real sampling frequency and duration of the measured signal (500 Hz and 287 s, respectively) the profile considered as reference for the experimental campaign was artificially assumed to be sampled at 130 Hz (for a corresponding duration of 1105 s, approximately), thus bringing the maximum values of the *PSD* down in the range 40-42 Hz. This was necessary in order to have a reasonable time to failure (*TTF*) of the specimens, by taking advantage of the increase in the damage at lower frequencies due to higher relative displacements. Another reason for this choice to bring the frequency spectrum in the range 40-42 Hz was to avoid the possible disturbance caused by the utility frequency of 50 Hz and its integer multiples. In addition, the profile was scaled down to 16% the original signal after some initial tests performed on the specimens (as designed in the next subsections) served to target a reasonable *TTF*. The reference profile is re-plotted in Fig.4.1 with its new duration, whereas its main statistical properties are shown in Table 4.1.

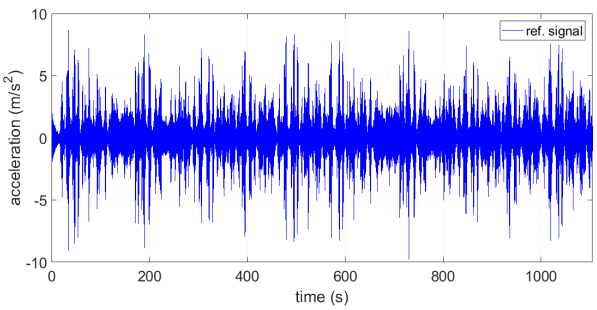

Fig.4.1: reference signal for experiments

Table 4.1: statistical properties of the reference signal

RMS $[\boldsymbol{m/s^2}]$	1.35
Kurtosis [-]	6.52
Crest factor [-]	7.26

4.1.2 Material

The aluminum alloy 7075 (also known by the trade name Ergal) was chosen to carry out the experimental tests. Its main mechanical properties were calculated to be the following:

- $\sigma_y = 518\ MPa$ (yield strength)
- $\sigma_b = 554\ MPa$ (ultimate tensile strength)
- $E = 82200\ MPa$ (Young modulus)

The mechanical properties were computed from the stress-strain curves obtained by tensile testing; some of these curves are plotted in Fig.4.2. Several specimens were subjected to a controlled tension until failure and the three values reported in this subsection come from an averaging process over all samples.

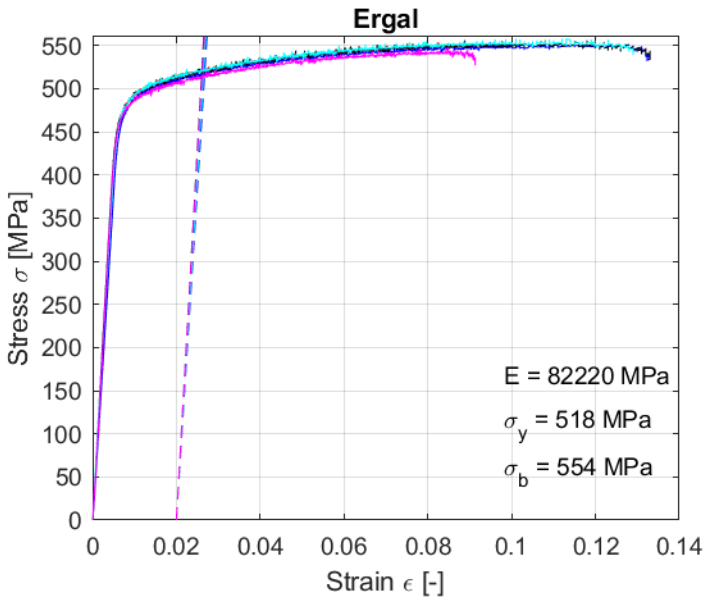

Fig.4.2: Stress-strain curves

4.1.3 Specimen geometry

The main target of the specimen design was to locate the first natural frequency in the band where the maxima of the reference signal's *PSD* occurred. Therefore, the target frequency was chosen to be 41 Hz, so that after the specimens get damaged during the tests, their subsequent decrease in frequency still corresponded to the highest values of the *PSD*. When the specimens were fixed to the shaker through the fixture (described in subsection 4.1.4), their disposition was horizontal and conceptually identical to cantilever beams subjected to bending. The presence of a rounded notch allowed for both shorter *TTF* and localization of failure. The geometry and size of the specimens are illustrated in Fig. 4.3.

Besides, additional masses were located near the tip of the specimens to get closer to the target natural frequency of 41 Hz. A thorough description of these masses and their arrangement on the specimens is given in section 4.2.

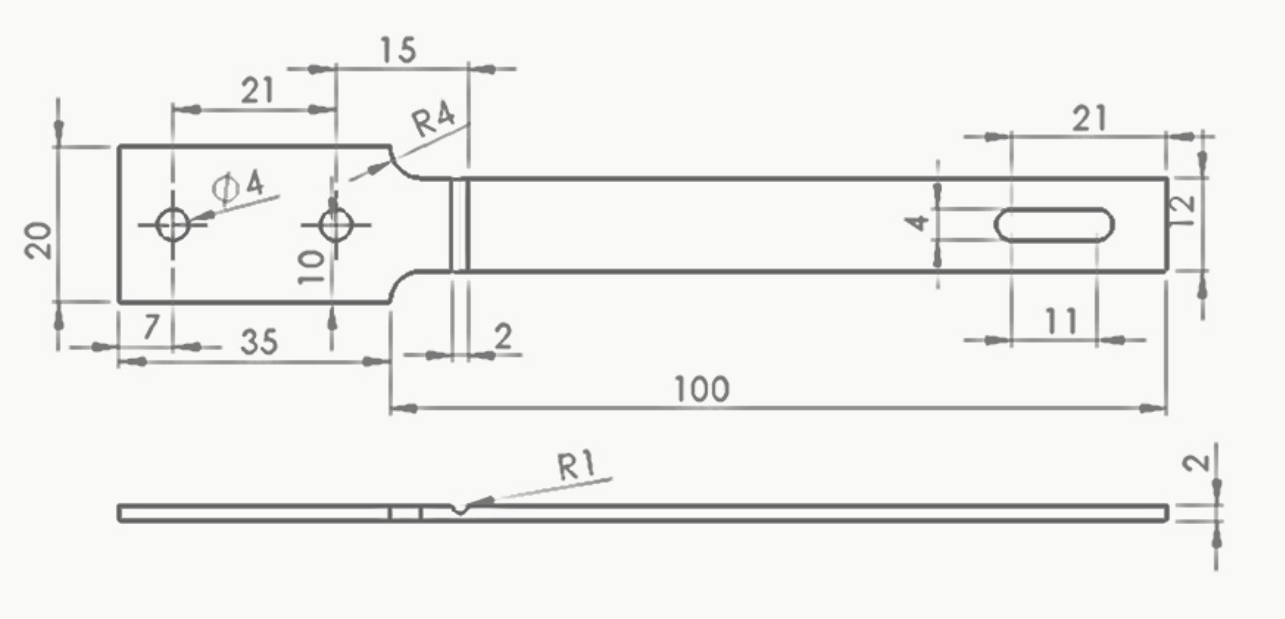

Fig.4.3: illustration of the specimens' geometry and dimensions

4.1.4 Fixture

The fixture was designed such that the specimens could be positioned horizontally. Its most important requirement had to be high stiffness so that the high frequency modes would be far from the natural frequency of the specimens, located at 41 Hz. It would allow five specimens to be fixed at a time due to the same number of slots available. However, as explained in the next section (section 4.2), only three slots at a time were used during the tests. An illustration of the fixture is shown in Fig.4.4.

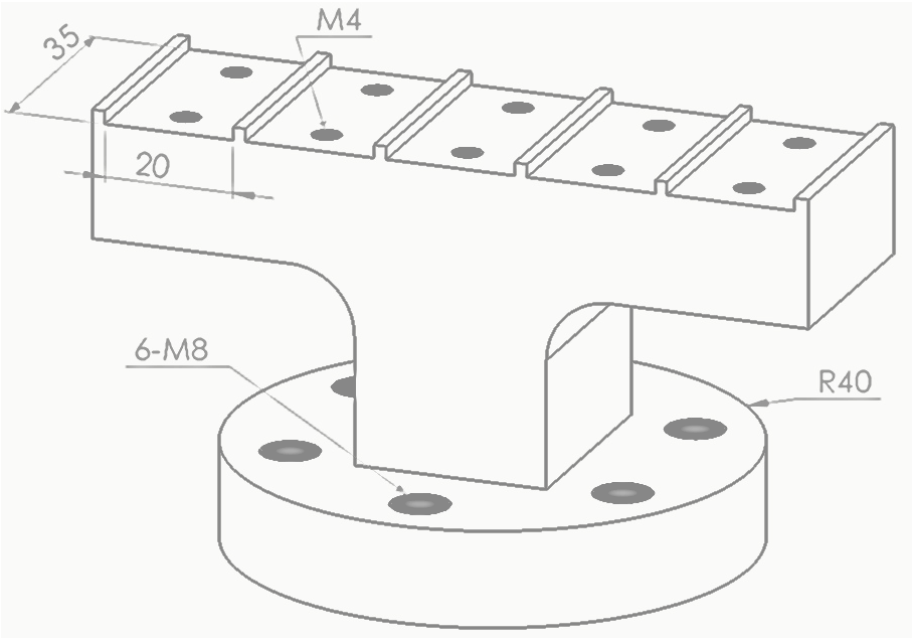

Fig.4.4: illustration of the fixture's geometry and dimensions

4.2 Setup and test procedures

The vibration signals were measured by means of four mono-axial accelerometers. Since the shaker's acquisition system only allowed measuring four signals at a time, the accelerometer measuring the shaker's base acceleration was placed on the fixture, whereas the other three accelerometers were placed on the specimens. The three specimens were arranged symmetrically on three out of the five slots of the fixture, with additional masses located near the tip to get closer to the target natural frequency of 41 Hz. The masses added to each of the specimens consisted of: two bolts glued to each other and also to the tip of the specimens, plus a parallelepiped-shaped iron mass of about 18 gr. The parallelepiped-shaped iron mass had a threaded hole which would allow its fastening to the specimens via the slotted hole. The latter would constitute a further possibility of adjusting the natural frequency of the specimens. The specimens, the fixture, the additional masses, and the accelerometers' arrangement are shown in Fig.4.5.
Besides, in order to comply with the shaker's operative conditions, a high-pass filter with 5 Hz cutoff frequency was used because displacements at low frequencies are too extreme for the shaker to handle. The characteristics of the latter are shown in Table 4.2, whereas a picture of the shaker (Dongling ES-2-150/DA-2) is shown in Fig.4.6.

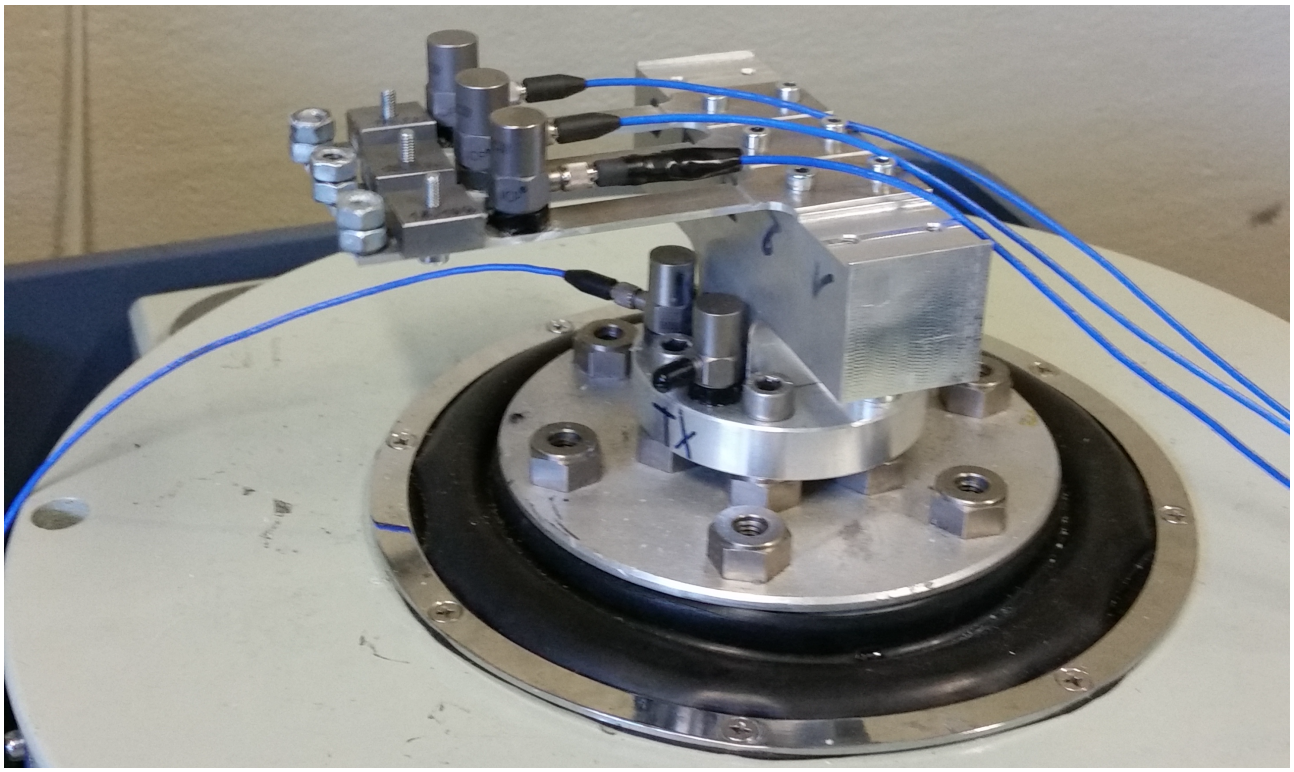

Fig.4.5: a picture of the setup showing: the head of the shaker, the fixture, the three specimens, the additional masses, the four accelerometers (three for the specimens, one for base acceleration)

Fig.4.6: Shaker Dongling ES-2-150/DA-2

Table 4.2: functional constraints of the shaker

Maximum frequency	4000 Hz
Resonance frequency	3621 Hz
Maximum displacement	12.5 mm
Maximum velocity	200 cm/s
Maximum acceleration	100 g
Maximum mass applicable to the armature	70 kg

4.3 Non-accelerated tests

Before starting the experimental campaign to test the results presented in this work, it was essential to determine the parameters involved in the synthesis procedure such as the coefficient b related to Wohler's curve slope and damping coefficient ζ. The former was calculated to be approximately equal to 9.00 thanks to ad-hoc random tests performed with different *RMS* levels as explained in Appendix G, whereas the latter was estimated to be about 1% by comparing numerical *SDOF* system responses with actual ones measured by accelerometers (Fig.4.7). In the case of non-stationary signals with narrow-banded blocks such as the reference signal chosen in subsection 4.1.1 (Fig. 4.1), the damping coefficient may play an important role in the synthesis procedure because sinusoids cause a greater damage if damping is smaller. Therefore, since the synthesis procedure starts from the *FDS* of the signal, it is of great import not to overestimate ζ, because it could lead to undertesting if the usual *PSD* is synthesized (this issue is better addressed in section 4.5).
The tests were performed by using three different acceleration profiles: (i) the reference signal chosen in subsection 4.1.1, (ii) a Gaussian signal synthesized according to the standard Mission Synthesis procedure, (iii) a Leptokurtic signal synthesized according to the *kFDS* algorithm. For each of the three profiles, three runs were performed; therefore, the total number of specimens to be analyzed was equal to nine (three specimens for each run). The nine times to failure were calculated to be those times at which the natural frequency of the specimens dropped by 5 % its initial value, which was approximately 41 Hz. The value of 41 Hz was the target value for the natural frequencies of all specimens, but the real experiments' setup led to unavoidable but acceptable fluctuations/errors in the initial value (the slotted hole in the specimens helped greatly to reduce this error, with the natural frequency always being in the range 40-42 Hz). In principle, these fluctuations might affect the definition of the *TTF* of each specimen if the value of its initial frequency is set to 41 Hz a priori and the frequency at which failure occurs is defined to be 5% of 41 Hz, which is approximately 39 Hz. In order to test the robustness of the conclusions that could be drawn from just one definition, the results were verified using two different *TTF* definitions. The first definition, hereinafter referred to as definition 1, was that failure occurs at the frequency 39 Hz for each specimen, whereas the second definition, hereinafter referred to as definition 2, was taken to be that failure occurs when the actual initial frequency drops by 5%. The natural frequencies were computed in this way: the time interval that defined the total life of the specimen was split into several blocks over which the frequency response function (*FRF)* of the system was computed and the frequency at which the *FRF* reached its maximum was taken to be the natural frequency of the specimen. The *FRF* is a transmissibility function which was calculated by using input and output acceleration signals. In Appendix G, failure

is defined as the time at which the tangent to the specimens' natural frequency curve (which was obtained by polynomial interpolation) reached a certain (negative) slope. In the following tests, this definition was not appropriate because the behavior of the natural frequency over time happened to be more irregular. This irregularity might be due to the shape of the *PSD* (no longer constant/flat as the one used in Appendix G), as well as the non-Gaussianity of the vibration profiles used. Since the frequency drop occurred in a much shorter amount of time compared to the lifetime of the specimens, the tests performed in Appendix G would not have been affected severely by the different possible definitions of failure. However, the accelerated tests that are performed in subsection 4.4 have shorter times to failure.

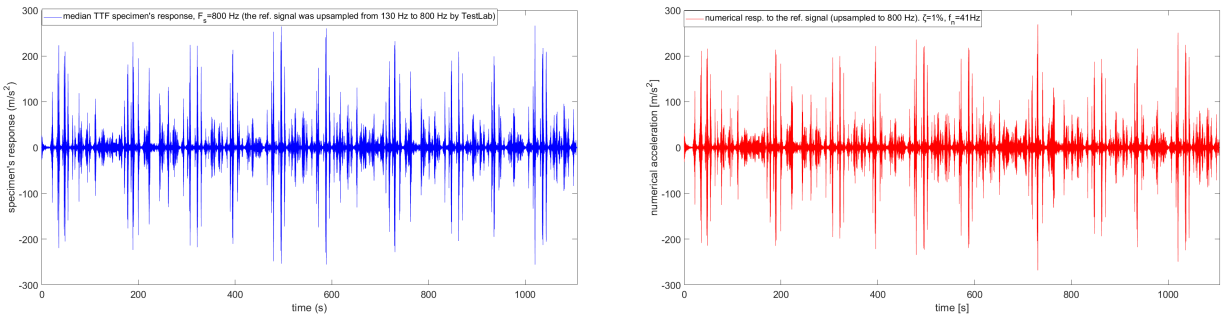

(a) (b)

Fig.4.7: (a) one of the specimens' measured response to the reference profile of Subsection 4.3.1, (b) *SDOF* system's numerical response to the same reference profile. The *SDOF* system's damping coefficient was set to 1%, whereas its natural frequency was set to 41 Hz. The reference signal used in the experimental tests, whose initial sampling frequency was equal to 130 Hz, was upsampled by the software to the sampling frequency of 800 Hz. Therefore, also the numerical response was calculated with $F_s = 800\ Hz$.

4.3.1 Reference profile

The reference profile shown in Fig.4.1 was replicated by means of the waveform replication mode, until all specimens reached failure. The signal, having sampling frequency equal to 130 Hz, was upsampled by the software to the sampling frequency of 800 Hz. A high-pass filter removed the first 5 Hz from the signal. The nine times to failure, calculated by using the two different definitions of failure, are reported in Tables 4.3 and 4.4. One of the replays of the signal executed by the shaker is displayed in Fig. 4.8, whereas its statistical parameters are reported in Table 4.5. By comparing Table 4.5 with Table 4.1, it is clear that the shaker is capable of reproducing the reference signal accurately with negligible error. This is even more so if the *FDS* and *MRS* of both the reference signal and the one reproduced by the shaker are compared (Fig.4.10). The specimen's response to one of the replays of the reference signal generated by the shaker is shown in Fig.4.9. The response shown is related to the signal which led to the mean *TTF* according to definition 1. The statistical parameters of the response are shown in Table 4.6.

Table 4.3: *TTF*'s and meaningful statistical parameters of the nine specimens calculated according to definition 1

Definition 1 of failure	**Run #1**	**Run #2**	**Run #3**
Specimen #1	1.82 h	1.07 h	2.70 h
Specimen #3	2.65 h	1.72 h	1.06 h
Specimen #5	0.91 h	0.93 h	2.06 h
Mean *TTF*: 1.66 h Median *TTF*: 1.72 h Standard deviation of *TTF's*: 0.712 h			

Table 4.4: *TTF*'s and meaningful statistical parameters of the nine specimens calculated according to definition 2

Definition 2 of failure	**Run #1**	**Run #2**	**Run #3**
Specimen #1	1.80 h	1.07 h	2.54 h
Specimen #3	2.76 h	1.70 h	1.06 h
Specimen #5	1.11 h	0.936 h	2.04 h
Mean *TTF*: 1.67 h Median *TTF*: 1.70 h Standard deviation of *TTF's*: 0.679 h			

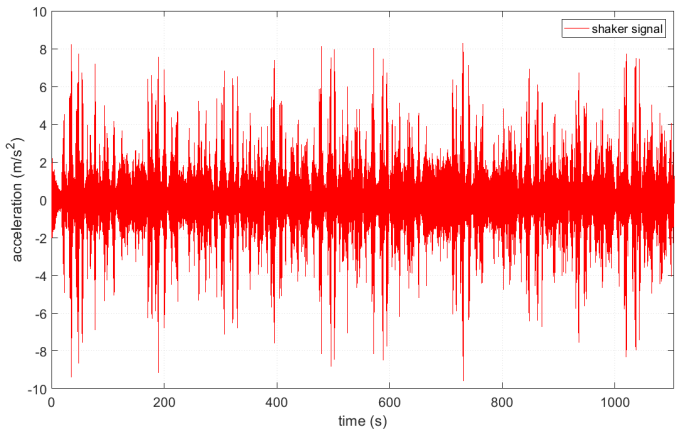

Fig.4.8: one of the replays of the reference signal generated by the shaker

Table 4.5: statistical properties of the reference signal

RMS $[\boldsymbol{m/s^2}]$	1.33
Kurtosis [-]	6.79
Crest factor [-]	7.22

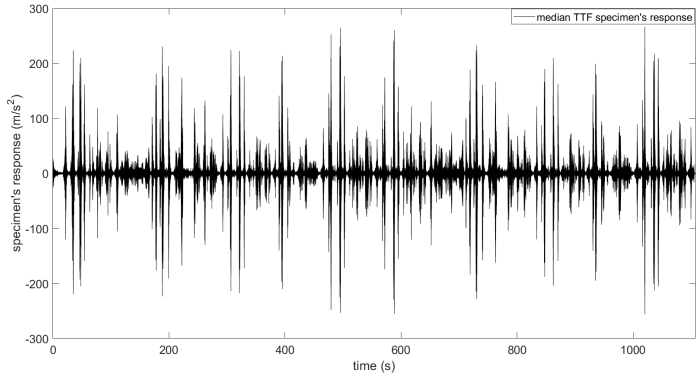

Fig.4.9: response to one of the replays of the reference signal generated by the shaker. The response shown here is related to the signal which led to the mean *TTF* according to definition 1.

Table 4.6: statistical properties of the response to one of the replays of the reference signal

RMS $[\boldsymbol{m/s^2}]$	27.4
Kurtosis [-]	19.2
Crest factor [-]	9.72

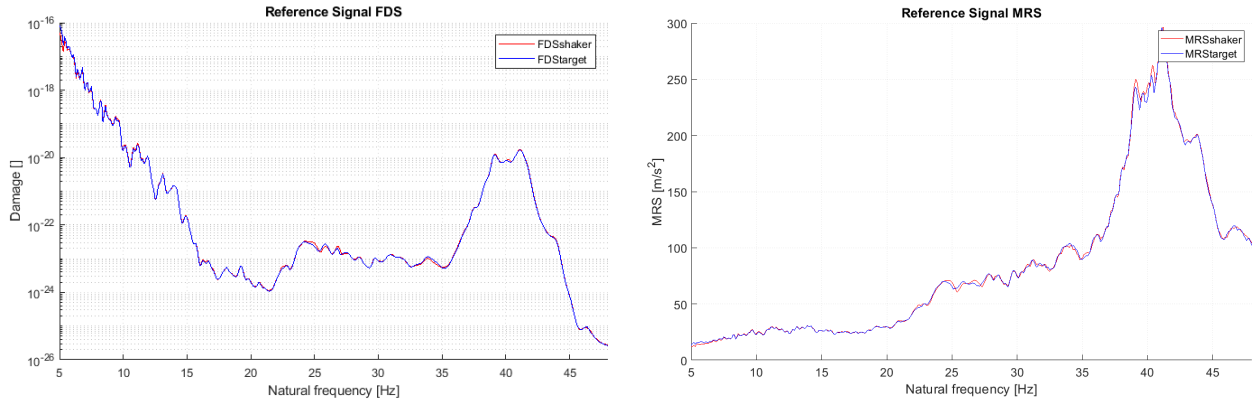

(a) (b)

Fig.4.10: comparison between the target reference signal and the one reproduced by the shaker in terms of: a) *FDS*, b) *MRS*. The curves are calculated by considering the parameters of the model to be: $b = 9, \zeta = 0.01$

4.3.2 Gaussian profile #1

In order to test the standard Mission Synthesis procedure, a Gaussian signal having the same duration (approximately 1105 seconds) and *FDS* as the reference signal was synthesized. The *FDS* equivalence was imposed over the mean *TTF* displayed in Table 4.3, namely 1.66 hours. Also in this case the waveform replication mode was used, so that the signal would be repeated until failure occurred. The nine times to failure, calculated by using the two different definitions of failure, are reported in Tables 4.7 and 4.8. Since the shaker was capable of reproducing the signals accurately with negligible error as shown in subsection 4.3.1, in this and the following subsections only the signals synthesized by the algorithms are displayed. The Gaussian signal synthesized is shown in Fig. 4.11, whereas its statistical parameters are reported in Table 4.9. The *FDS* and *MRS* of both the reference and the synthesized Gaussian signals are compared in Fig.4.13. The specimen's response to one of the replays of the reference signal generated by the shaker is shown in Fig.4.12. The response shown is related to the signal which led to the mean *TTF* according to definition 1. The statistical parameters of the response are shown in Table 4.10.

Table 4.7: *TTF*'s and meaningful statistical parameters of the nine specimens calculated according to definition 1

Definition 1 of failure	**Run #1**	**Run #2**	**Run #3**
Specimen #1	1.46 h	0.84 h	0.29 h
Specimen #3	2.00 h	1.44 h	1.49 h
Specimen #5	1.12 h	0.88 h	0.59 h
Mean *TTF*: 1.12 h Median *TTF*: 1.12 h Standard deviation of *TTF's*: 0.529 h			

Table 4.8: *TTF*'s and meaningful statistical parameters of the nine specimens calculated according to definition 2

Definition 2 of failure	**Run #1**	**Run #2**	**Run #3**
Specimen #1	1.46 h	0.840 h	0.281 h
Specimen #3	1.97 h	1.44 h	1.49 h
Specimen #5	1.12 h	0.877 h	0.592 h
Mean *TTF*: 1.12 h Median *TTF*: 1.12 h Standard deviation of *TTF's*: 0.524 h			

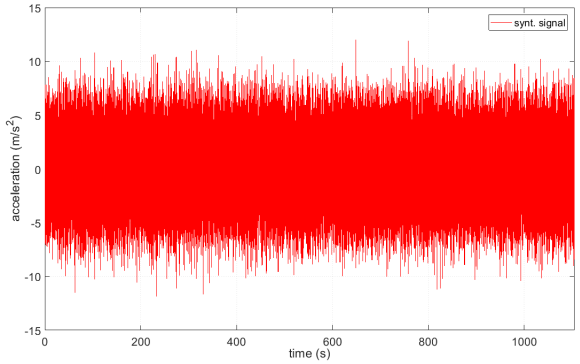

Fig.4.11: signal synthesized according to the Standard Mission Synthesis procedure

Table 4.9: statistical properties of the Gaussian signal

RMS $[\boldsymbol{m/s^2}]$	2.70
Kurtosis [-]	3.01
Crest factor [-]	4.40

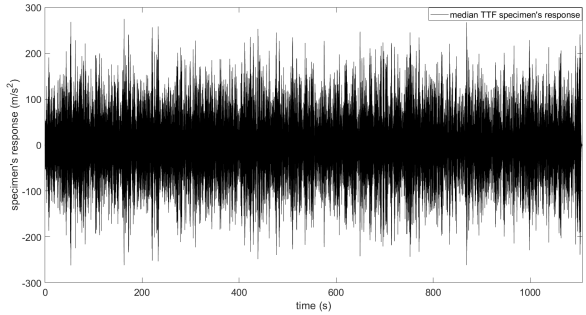

Fig.4.12: response to one of the replays of the signal generated by the shaker. The response shown here is related to the signal which led to the mean *TTF* according to definition 1.

Table 4.10: statistical properties of the response to one of the replays of the signal

RMS $[\boldsymbol{m/s^2}]$	66.6
Kurtosis [-]	3.09
Crest factor [-]	4.12

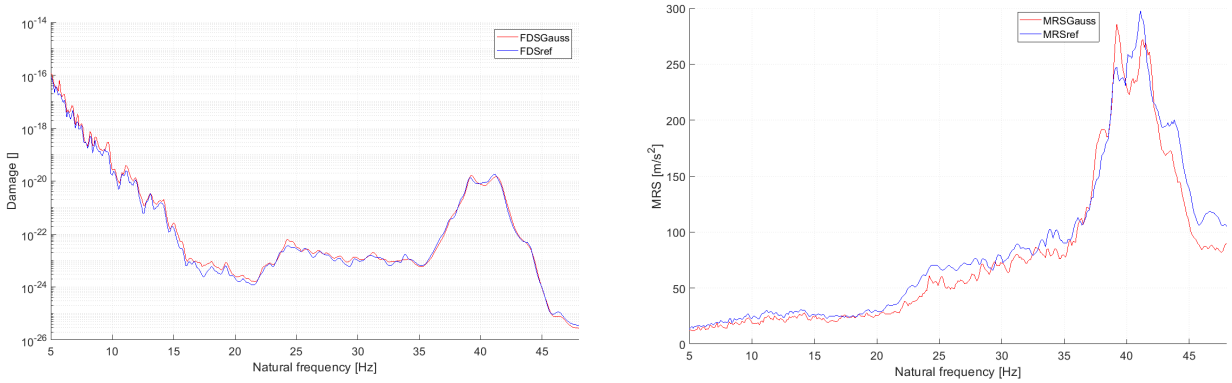

(a) (b)

Fig.4.13: comparison between the target reference signal and the Gaussian one in terms of: a) *FDS*, b) *MRS*. The curves are calculated by considering the parameters of the model to be: $b = 9, \zeta = 0.01$

4.3.3 *kFDS* profile #1

The *kFDS* algorithm, described in subsection 2.2.1, was selected among the algorithms proposed in chapter 2. The signal synthesized by this algorithm had the same duration (approximately 1105 seconds) and *FDS* as the reference signal. The *FDS* equivalence was imposed over the mean *TTF* displayed in Table 4.3, namely 1.66 hours. The waveform replication mode was used, so that the signal would be repeated until failure occurred. The nine times to failure, calculated by using the two different definitions of failure, are reported in Tables 4.11 and 4.12. The signal synthesized by the *kFDS* algorithm is shown in Fig. 4.14, whereas its statistical parameters are reported in Table 4.13. The specimen's response to one of the replays of the reference signal generated by the shaker is shown in Fig.4.15. The response shown is related to the signal which led to the mean *TTF* according to definition 1. The statistical parameters of the response are shown in Table 4.14

The *FDS* and *MRS* of both the reference and the synthesized Gaussian signals are compared in Fig.4.16.

Table 4.11: *TTF*'s and meaningful statistical parameters of the nine specimens calculated according to definition 1

Definition 1 of failure	**Run #1**	**Run #2**	**Run #3**
Specimen #1	2.00 h	1.64 h	1.68 h
Specimen #3	2.74 h	2.25 h	1.60 h
Specimen #5	1.00 h	0.871 h	1.82 h
Mean *TTF*: 1.73 h Median *TTF*: 1.68 h Standard deviation of *TTF's*: 0.578 h			

Table 4.12: *TTF*'s and meaningful statistical parameters of the nine specimens calculated according to definition 2

Definition 2 of failure	**Run #1**	**Run #2**	**Run #3**
Specimen #1	2.00 h	1.71 h	1.69 h
Specimen #3	2.74 h	2.25 h	1.60 h
Specimen #5	1.08 h	0.871 h	1.82 h
Mean *TTF*: 1.75 h Median *TTF*: 1.71 h Standard deviation of *TTF's*: 0.564 h			

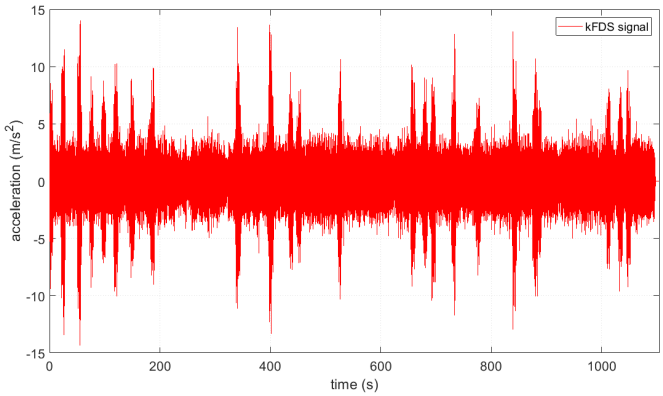

Fig.4.14: signal synthesized by the *kFDS* algorithm

Table 4.13: statistical properties of the signal synthesized by the *kFDS* algorithm

RMS $[\boldsymbol{m/s^2}]$	1.67
Kurtosis [-]	6.55
Crest factor [-]	8.82

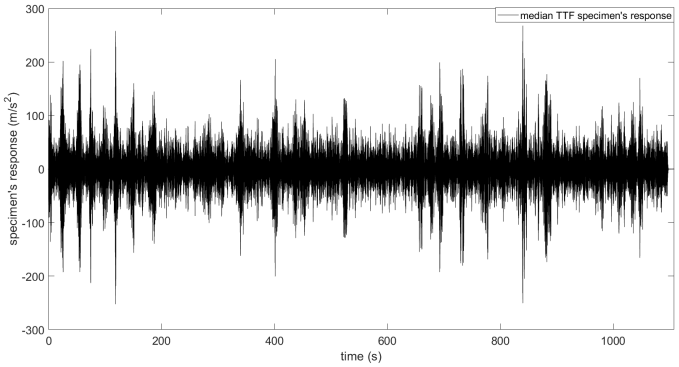

Fig.4.15: response to one of the replays of the signal generated by the shaker. The response shown here is related to the signal which led to the mean *TTF* according to definition 1.

Table 4.14: statistical properties of the response to one of the replays of the signal

RMS $[\boldsymbol{m/s^2}]$	35.0
Kurtosis [-]	6.11
Crest factor [-]	7.66

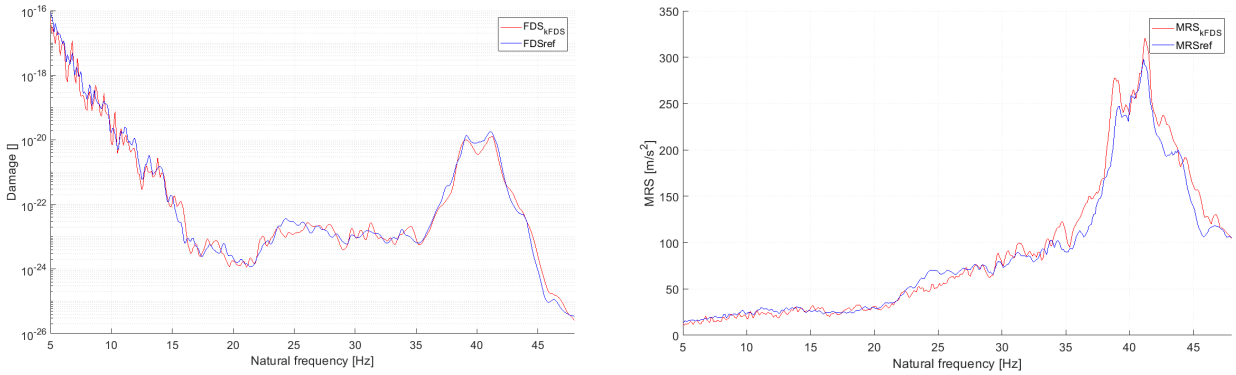

(a) (b)

Fig.4.16: comparison between the target reference signal and the one synthesized by the *kFDS* algorithm in terms of: a) *FDS*, b) *MRS*. The curves are calculated by considering the parameters of the model to be: $b = 9, \zeta = 0.01$

4.3.4 Discussion

The results show that the difference between the two definitions of failure, in terms of mean and median *TTF's,* is at the most 0.03 hours (i.e. less than 2 minutes). The Gaussian synthesis led to overtesting the specimens, because the mean *TTF* was about 32 % less than the expected 1.66 hours. This could be expected by looking at the *RMS* level of tables 4.9 and 4.10 and comparing them to the other profiles; nevertheless, those values are the product of the synthesis procedure, which is also affected by the choice of the parameters b and ζ. Besides, in order to compensate for the lack of high peaks which are present in the non-Gaussian reference signal, the only possibility for the Gaussian synthesis is to increase the overall energy level (*RMS*) in order to match the *FDS*. On the other hand, the *kFDS* algorithm's mean *TTF* is much closer: in fact, the estimation is off by approximately 5%. This better match might be due to such factors as the small amplitudes' contribution in the reference signal, which are below the fatigue limit of the material. In fact, these low amplitudes are still damaging according to the model, even if to a small degree, still contributing to the *FDS* and therefore possibly leading to overtesting the material when the Gaussian signal is synthesized from the *FDS*. On the other hand, the *kFDS* algorithm synthesizes a signal with the same kurtosis value and *FDS* as the reference signal, thus characterized approximately by the same amount of downtime, possibly 'cancelling' the effect of damage overestimation that may occur when Gaussian tests are performed.

4.4 Accelerated tests

In this section accelerated tests are addressed. In analogy with section 4.3, the tests were performed by using three different acceleration profiles: the reference signal shown in Fig. 4.1 was scaled up by a factor of 1.25 and the test results were used to determine the new mean *TTF* in subsection 4.4.1. This mean *TTF* so obtained was then used to synthesize a Gaussian signal according to the standard Mission Synthesis procedure, which is described in subsection 4.4.2, whereas a Leptokurtic signal was synthesized according to the *kFDS* algorithm and the resulting test results described in subsection 4.4.3. For each of the three profiles, three tests were performed; therefore, the total number of specimens to be analyzed was equal to nine (three specimens for each test). The nine times to failure were calculated according to the two different definitions given in section 4.3.

4.4.1 Amplified reference profile

The reference profile shown in fig.4.1, was multiplied by a factor of 1.25 and replicated by means of the waveform replication mode, until all specimens reached failure. The signal, sampled at 130 Hz, was upsampled by the software to the sampling frequency of 800 Hz. A high-pass filter removed the first 5 Hz from the signal. The nine times to failure, calculated by using the two different definitions, are reported in Tables 4.15 and 4.16. Due to the scaling factor, the standard deviation is also scaled accordingly (i.e. the one reported in Table 4.5 is multiplied by 1.25), whereas the crest factor and kurtosis value remain unaffected. The *FDS* is simply scaled by a factor exactly equal to 1.25^b and the *MRS* by a factor of 1.25. The measured response to one of the replays of the reference signal generated by the shaker is shown in Fig.4.17, and its statistical parameters in Table 4.17.

Table 4.15: *TTF*'s and meaningful statistical parameters of the nine specimens calculated according to definition 1

Definition 1 of failure	**Run #1**	**Run #2**	**Run #3**
Specimen #1	0.381 h	0.503 h	0.684
Specimen #3	0.379 h	0.431 h	0.441
Specimen #5	0.534 h	0.585 h	0.295
Mean *TTF*: 0.470 h Median *TTF*: 0.441 h Standard deviation of *TTF's*: 0.119 h			

Table 4.16: *TTF*'s and meaningful statistical parameters of the nine specimens calculated according to definition 2

Definition 2 of failure	**Run #1**	**Run #2**	**Run #3**
Specimen #1	0.421 h	0.503 h	0.684
Specimen #3	0.472 h	0.464 h	0.443
Specimen #5	0.569 h	0.662 h	0.319
Mean *TTF*: 0.504 h Median *TTF*: 0.472 h Standard deviation of *TTF's*: 0.117 h			

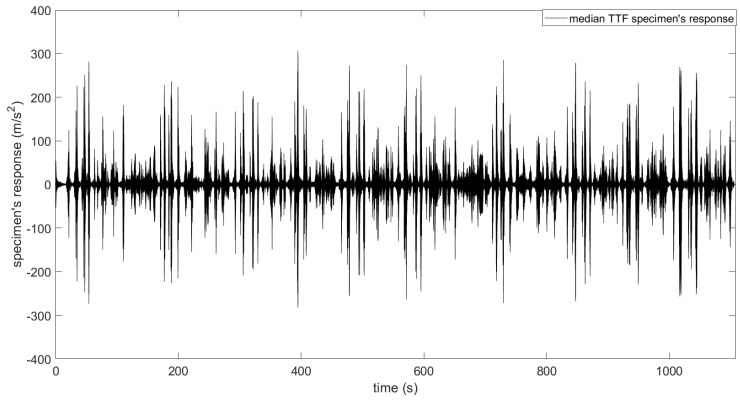

Fig.4.17: response to one of the replays of the reference signal generated by the shaker. The response shown here is related to the signal which led to the mean *TTF* according to definition 1.

Table 4.17: statistical properties of the response to one of the replays of the signal

RMS $[\boldsymbol{m/s^2}]$	37.05
Kurtosis [-]	13.6
Crest factor [-]	8.28

4.4.2 Gaussian profile #2

In order to test the standard Mission Synthesis procedure while performing accelerated tests, a Gaussian signal having a duration of 0.470 hours and same *FDS* as the reference signal (the one described in subsection 4.1.1) was synthesized. The *FDS* equivalence was imposed over the mean *TTF* displayed in Table 4.15, namely 0.470 hours[18]. Also in this case, the waveform replication mode was used, so that the signal would be repeated until failure occurred, still taking into account that failure was expected to occur (ideally) near the final part of the first replay. The nine times to failure, calculated by using the two different definitions of failure, are reported in Tables 4.18 and 4.19. Since the shaker was capable of reproducing the signals accurately with negligible error as shown in subsection 4.3.1, in this and the following subsection only the signals synthesized by the algorithms are displayed. The synthesized Gaussian signal is shown in Fig. 4.18, whereas its statistical parameters are reported in Table 4.20. The measured response to one of the replays of the reference signal generated by the shaker is shown in Fig.4.19, and its statistical parameters in Table 4.21.
The *FDS* and *MRS* of both the amplified reference signal and the synthesized Gaussian signal are compared in Fig.4.20. It should be noted that the equivalence between the two *FDS* curves in Fig.4.20 is not to be taken for granted in this case, unlike it was in section 4.3. This is because the *TTF* (0.470 h) related to the amplified reference signal of subsection 4.4.1 is experimental, whereas the *TTF* (0.470 h) associated with the synthesized signal is theoretical and contingent on the model employed to estimate damage accumulation, whose assumptions lead to the definition of the *FDS*. In fact, the model is characterized by uncertainties, especially in the parameter b (assumed to be equal to 9), which could lead to different results than expected. The scaling factor of 1.25 used to amplify the reference signal of subsection 4.4.1, together with the experimental *TTF*'s of 0.470 h and 1.66 h, are theoretically relatable to the parameter b of the model. In particular, by imposing the equivalence between the unamplified reference signal's *FDS,* computed over a duration of 1.66 h, and the amplified reference signal's *FDS,* computed over a duration of 0.470 h, from Eqs.(2.11, 2.12) it can be easily inferred that b must satisfy:

[18] In this case, the duration of the synthesized signal coincides with the theoretical *TTF*, but it might be useful to recall that this might not always necessarily be the case, as suggested by section 4.3.

$$\frac{1.66}{0.470} = 1.25^{b} \tag{4.1}$$

The solution of Eq.(4.1) in terms of b, gives about 5.6, instead of the value 9 used by the model. This calculation is only meant to highlight that it might be challenging to attribute a sound numerical value to parameter b; the value of 9 is retained in the synthesis procedure both in section 4.4.2 and 4.4.3. Therefore, with the assumption that $b = 9$ and $\zeta = 0.01$, it is granted that the *FDS* of the (unamplified) reference signal, computed over a duration of 1.66 hours, is (approximately) the same as that of the synthesized signal, computed over a duration of 0.470 hours. However, it is not granted that the same would hold for the *FDS* of the amplified signal, calculated over a duration of 0.470 hours and compared with that of the signal synthesized in this subsection (still calculated over a duration of 0.470 hours), because the uncertainties in the model, especially in the parameter b, could lead to different results as mentioned.
In fact, the *FDS* mismatch is slightly more noticeable in this case, but still acceptable[19], with the *FDS* of the Gaussian signal lying slightly below the one of the amplified reference profile. Nevertheless, the mean *TTF's* in Tables 4.13 and 4.14 are still lower by an amount respectively equal to 41.9 % and 41.7 % than the theoretical 0.470 hours. This excessive overtesting suggests that this standard Mission Synthesis procedure might not be accurate in this situation, with the synthesis starting from this particular type of reference signals.

Table 4.18: *TTF*'s and meaningful statistical parameters of the nine specimens calculated according to definition 1

Definition 1 of failure	**Run #1**	**Run #2**	**Run #3**
Specimen #1	0.210 h	0.215 h	0.437
Specimen #3	0.186 h	0.177 h	0.157
Specimen #5	0.461 h	0.274 h	0.337
Mean *TTF*: 0.273 h Median *TTF*: 0.215 h Standard deviation of *TTF's*: 0.114 h			

Table 4.19: *TTF*'s and meaningful statistical parameters of the nine specimens calculated according to definition 2

Definition 2 of failure	**Run #1**	**Run #2**	**Run #3**
Specimen #1	0.210 h	0.205 h	0.460
Specimen #3	0.186 h	0.177 h	0.165
Specimen #5	0.457 h	0.250 h	0.354
Mean *TTF*: 0.274 h Median *TTF*: 0.210 h Standard deviation of *TTF's*: 0.119 h			

[19] It is worth recalling that the *FDS* curve represents the *mean* value of the damage (at a certain frequency), which implies the damage also has a standard deviation associated with it. This standard deviation, together with the assumptions at the basis of the simplistic model adopted, allows a margin of error in reaching a target *FDS.* C. Lalanne [13] provides more details in quantifying fatigue damage's standard deviation.

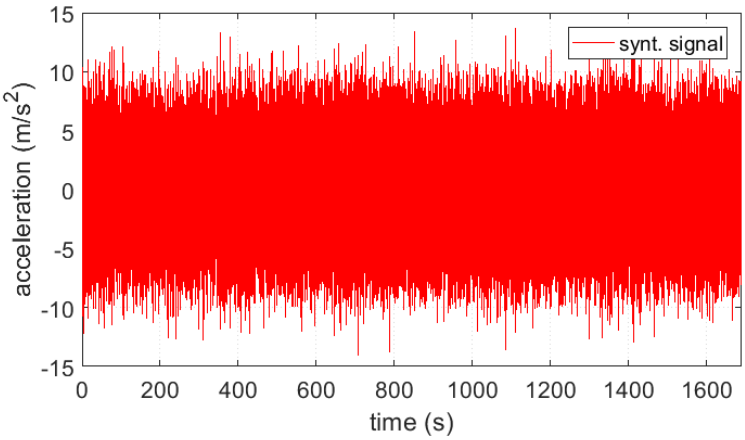

Fig.4.18: signal synthesized according to the Standard Mission Synthesis procedure for accelerated tests

Table 4.20: statistical properties of the Gaussian signal

RMS $[\boldsymbol{m/s^2}]$	3.08
Kurtosis [-]	2.99
Crest factor [-]	4.57

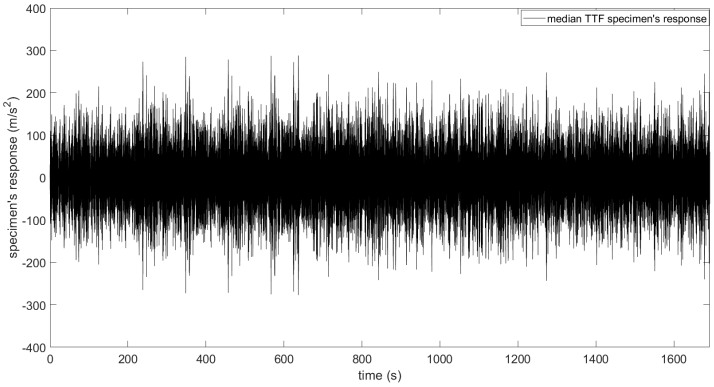

Fig.4.19: response to one of the replays of the signal generated by the shaker. The response shown here is related to the signal which led to the mean *TTF* according to definition 1.

Table 4.21: statistical properties of the response to one of the replays of the signal

RMS $[\boldsymbol{m/s^2}]$	62.2
Kurtosis [-]	3.15
Crest factor [-]	4.63

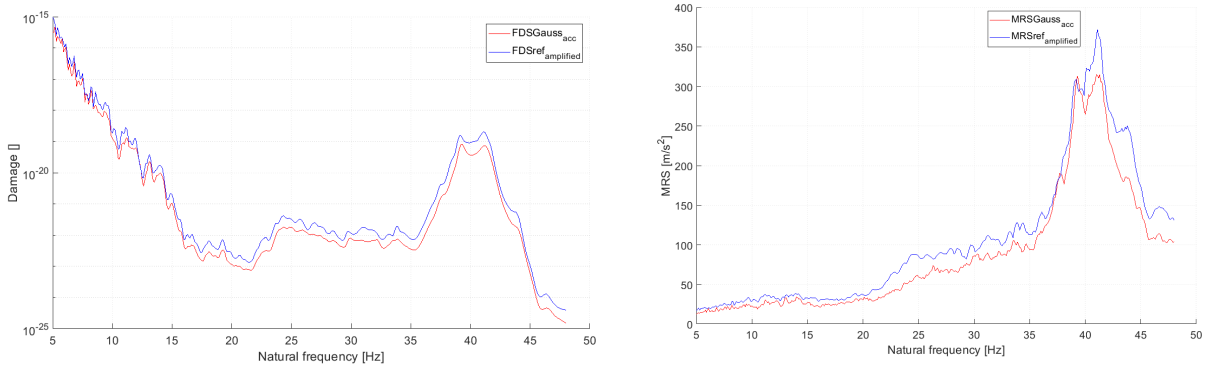

(a) (b)

Fig.4.20: comparison between the amplified reference signal and the Gaussian one: a) *FDS*, b) *MRS*. The curves are calculated by considering the parameters of the model to be: $b = 9, \zeta = 0.01$

4.4.3 *kFDS* profile #2

The *kFDS* algorithm was used to synthesize a signal having a duration of 0.470 hours and the same *FDS* as the reference signal described in subsection 4.1.1. The *FDS* equivalence was imposed over the mean *TTF* displayed in Table 4.15, namely 0.470 hours. Also in this case, the waveform replication mode was used, so that the signal would be repeated until failure occurred, still taking into account that failure was expected to occur (ideally) at the final part of the first replay. The nine times to failure, calculated by using the two different definitions of failure, are reported in Tables 4.22 and 4.23. The synthesized signal is shown in Fig. 4.21, whereas its statistical parameters are reported in Table 4.24. The measured response to one of the replays of the reference signal generated by the shaker is shown in Fig.4.22, and its statistical parameters in Table 4.25.
The *FDS* and *MRS* of both the amplified reference signal and the synthesized signal are compared in Fig.4.23. It should be noted that the comparison between the *FDS* curves in Fig.4.23 is not to be taken for granted in this case, for the exact same reason explained in subsection 4.4.2. The *FDS* curves are sufficiently close to each other, even though the synthesized signal's *FDS* is still slightly below the reference one. However, unlike the mean *TTF's* shown in subsection 4.4.2, the mean *TTF's* values presented in Tables 4.22 and 4.23 are much closer to the target value of 0.470 h; in fact, the maximum error is approximately 3.2 %, suggesting a greater accuracy on the part of the *kFDS* algorithm.

Table 4.22: *TTF*'s and meaningful statistical parameters of the nine specimens calculated according to definition 1

Definition 1 of failure	**Run #1**	**Run #2**	**Run #3**
Specimen #1	0.487 h	0.373 h	0.558
Specimen #3	0.652 h	0.319 h	0.511
Specimen #5	0.589 h	0.515 h	0.357
Mean *TTF*: 0.485 h Median *TTF*: 0.511 h Standard deviation of *TTF's*: 0.113 h			

Table 4.23: *TTF*'s and meaningful statistical parameters of the nine specimens calculated according to definition 2

Definition 2 of failure	**Run #1**	**Run #2**	**Run #3**
Specimen #1	0.490 h	0.360 h	0.558
Specimen #3	0.654 h	0.326 h	0.502
Specimen #5	0.599 h	0.521 h	0.363
Mean *TTF*: 0.486 h Median *TTF*: 0.502 h Standard deviation of *TTF's*: 0.114 h			

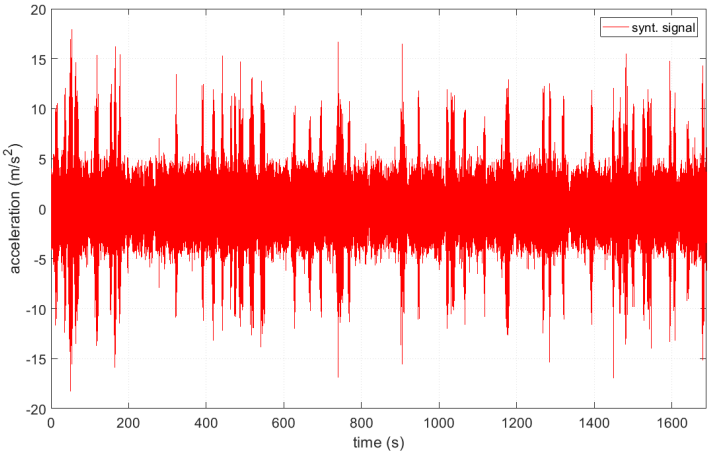

Fig.4.21: signal synthesized by the *kFDS* algorithm

Table 4.24: statistical properties of the signal synthesized by the *kFDS* algorithm

RMS $[\boldsymbol{m/s^2}]$	2.15
Kurtosis [-]	6.47
Crest factor [-]	8.61

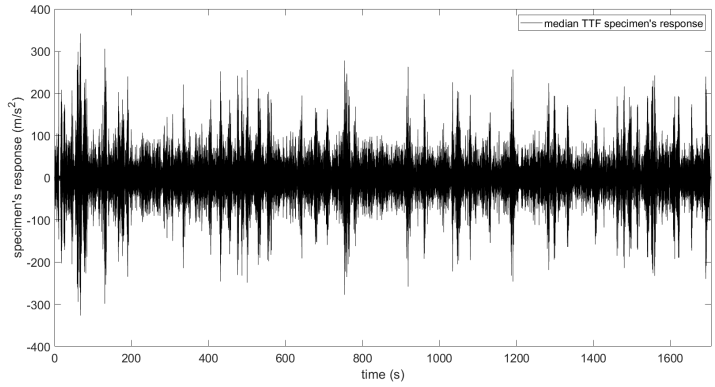

Fig.4.22: response to one of the replays of the signal generated by the shaker. The response shown here is related to the signal which led to the mean *TTF* according to definition 1.

Table 4.25: statistical properties of the response to one of the replays of the signal

RMS $[\boldsymbol{m/s^2}]$	44.9
Kurtosis [-]	6.09
Crest factor [-]	7.61

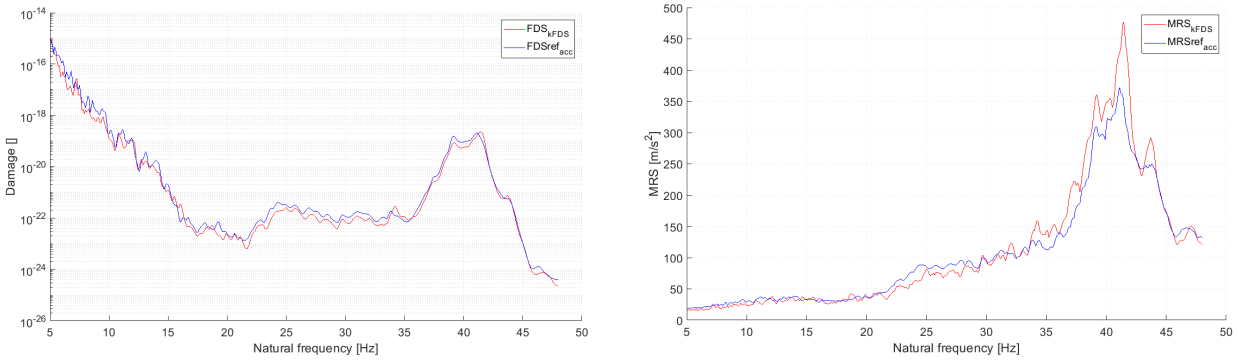

(a) (b)

Fig.4.23: comparison between the amplified reference signal and the one synthesized by the kFDS algorithm: a) *FDS*, b) *MRS*. The curves are calculated by considering the parameters of the model to be: $b = 9, \zeta = 0.01$

4.4.4 Discussion

The results show that the difference between the two definitions of failure, in terms of mean and median *TTF's,* is at the most 0.034 hours (i.e. approximately 2 minutes). The Gaussian synthesis led to overtesting the specimens, because the mean *TTF* was about 42 % less than the expected 0.470 hours. The *kFDS* algorithm's mean *TTF* is much closer: in fact, the estimation is off by about 3 %. This standard method's mismatch might be due to the overestimation of the small amplitudes' contribution to damage that are present in the reference signal, as already described in subsection 4.3.4.

4.5 Influence of damping ratio and Wohler's curve slope

The most influential parameters in the fatigue model used are the coefficient related to Wohler's curve slope and damping coefficient, denoted as usual by b and ζ respectively. In the system considered in chapter 4, parameter ζ was not difficult to evaluate, because the *SDOF* system model accurately approximated the specimens. In practice this might not always be the case for complicated *DUT*'s, but for *SDOF* systems the evaluation of ζ is straightforward. Even though in the literature it is recommended to set this coefficient ζ to a standard 5% [40], it might be useful to show that this choice is not uninfluential in all cases. In fact, as already mentioned in section 4.3, in the case of non-stationary signals with narrow-banded blocks such as the reference signal chosen in subsection 4.1.1, the damping coefficient may play an important role in the synthesis procedure because sinusoids cause a greater damage if damping is smaller. Therefore, since the synthesis procedure starts from the *FDS* of the signal, it is of great import not to overestimate ζ, because it could lead to undertesting if the usual *PSD* is synthesized[20].

In order to show an example of the influence of ζ, two acceleration profiles were synthesized with the same procedure used in section 4.3, that is, the profiles have the same *FDS* as that of the reference signal of subsection 4.1.1 computed over 1.66 hours. However, in this case the parameter ζ was set to 5% instead of 1%, whereas the same value of b was preserved, therefore the value of 9.00 was used in the synthesis. The first of the two profiles was synthesized according to the standard procedure, leading to the Gaussian signal shown in Fig. 4.24, whose main statistical characteristics are reported in Table 4.26. The second one was synthesized by the *VSD* algorithm and the Kihm's filtering technique (discussed in section 2.1) was applied a posteriori in order to match the *FDS* curves over a duration of 1.66 hours. The *VSD* signal is shown in Fig.4.25 and its statistical properties in Table 4.27.

In order to see how the two signals would fare in real experiments, for each of the two profiles, one test was performed with the setup already described in chapter 4 (where ζ is approximately equal to 1%). Therefore, the total number of specimens to be analyzed was equal to three (three specimens for each test). The number of tests was chosen to be the bare minimum because this was not the major focus of the work; rather, the only test was used as a way of possibly corroborating what should already be known theoretically, namely the influence of an overestimation of parameter ζ. The three times to failure were calculated and are shown in Table 4.28. The results show that the overestimation of ζ lead to an underestimation of the mean *TTF* (which was expected to be close to 1.66 hours theoretically if parameter ζ were approximately equal to 1%). The test performed with the Gaussian signal leads to a greater underestimation of the damage (i.e. the mean *TTF*), whereas the signal

[20] if ζ is unknown, its underestimation would be more appropriate since it would cause an overestimation of the damage, thus leading to more conservative results.

generated by the *VSD* algorithm and a posteriori application of Kihm's filtering technique (with $\zeta = 5\%$) leads to a less conspicuous underestimation of the damage.

As regards parameter b, its estimation is more difficult to make than in the case of ζ without performing experiments. Besides, even if experiments are done, an accurate estimation is unlikely due to the intrinsic indeterministic nature of fatigue-related phenomena, as well as the simplifying assumption that Wohler's curve accurately describes the behavior of the material. In fact, Wohler's curve parameters can be influenced by many factors such as: the type of load (sinusoidal, Gaussian, etc.), temperature, corrosion, residual stresses, the presence of notches, etc. All these factors combined account for the great number of different values of b given in the literature [36], even for the same material. In order to test the robustness of the algorithms presented in this work, the *FDS* of the two acceleration profiles shown in subsections 4.3.2 and 4.3.3 are calculated with a different value for the parameter b[21]. In particular, the value of b was set equal to 4, whereas ζ was maintained at 1%; with this value of b, the *FDS* of the signal of Fig.4.11 is displayed in Fig.4.26a, together with that of the reference signal of Fig.4.1. The *FDS* of the signal of Fig.4.14 is shown in Fig.4.26b, together with that of the reference signal of Fig.4.1. It is clear how the *kFDS* algorithm is not affected as much as the standard Mission Synthesis; in fact, the *FDS* is still close to the target one in the former case, whereas not the same can be said in the latter. Something similar could be said if, instead of setting b equal to 4, the latter is set to a value greater than 9. In Fig.4.27 the two *FDS* curves are plotted in a similar fashion to the one described for Fig.4.26, with the only difference being the value of parameter b, which is set to 14. In this case it is harder to appreciate the difference between the curves because the y-axis spans a larger range than in the case where b was equal to 4, nevertheless the *FDS* of the profile synthesized by the *kFDS* algorithm is closer to that of the reference profile especially in the bandwidth of interest (near 40 Hz).

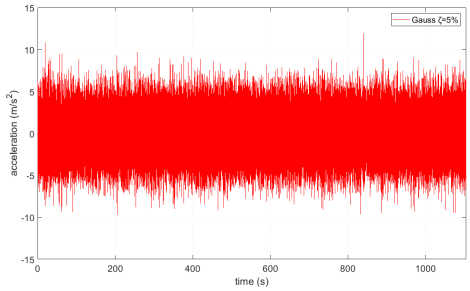

Fig.4.24: signal synthesized by the standard Mission Synthesis procedure with $\zeta = 5\%$

Table 4.26: statistical properties of the Gaussian signal synthesized with ζ =5%

RMS $[\boldsymbol{m/s^2}]$	2.30
Kurtosis [-]	3.01
Crest factor [-]	6.24

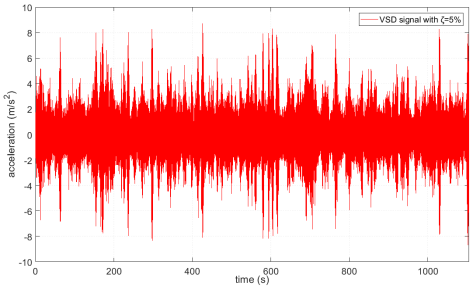

Fig.4.25: signal synthesized by the *VSD* algorithm with $\zeta = 5\%$

Table 4.27: statistical properties of the signal synthesized by the *VSD* algorithm with ζ =5%

RMS $[\boldsymbol{m/s^2}]$	1.44
Kurtosis [-]	5.21
Crest factor [-]	5.99

[21] It should be recalled that the profiles were synthesized with $b = 9$.

Table 4.28: *TTF*'s and meaningful statistical parameters of the Gaussian and *VSD* test calculated according to definition 2

Definition 2 of failure	**Gaussian Test**	**VSD Test**
Specimen #1	3.53 h	2.78 h
Specimen #3	4.39 h	2.20 h
Specimen #5	10.1 h	3.61 h
	Mean *TTF*: 6.01 h Median *TTF*: 4.39 h Standard deviation of *TTF's*: 3.57 h	Mean *TTF*: 2.86 h Median *TTF*: 2.78 h Standard deviation of *TTF's*: 0.709 h

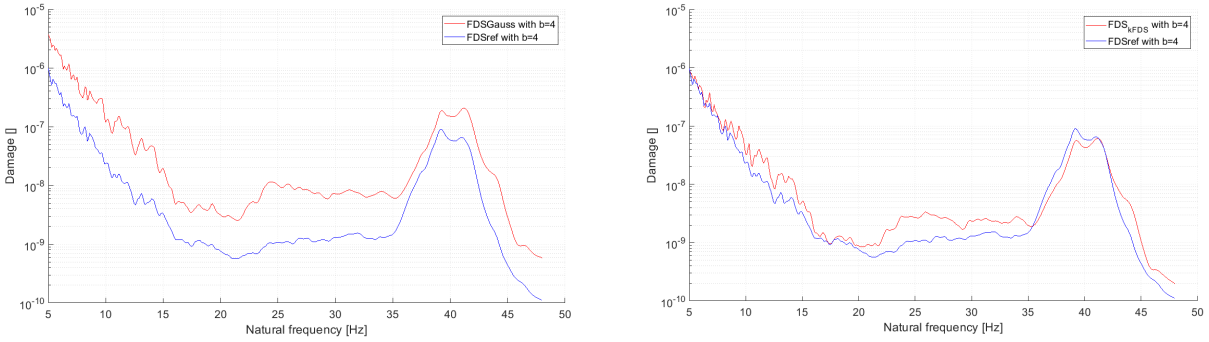

(a) (b)

Fig.4.26: comparison between the *FDS* of the reference signal of subsection 4.1.1 and that of the signal synthesized by a) the standard practice as described in subsection 4.3.2 b) the *kFDS* algorithm as described in subsection 4.3.3. The curves are calculated by considering the parameters of the model to be: $b = 4, \zeta = 0.01$

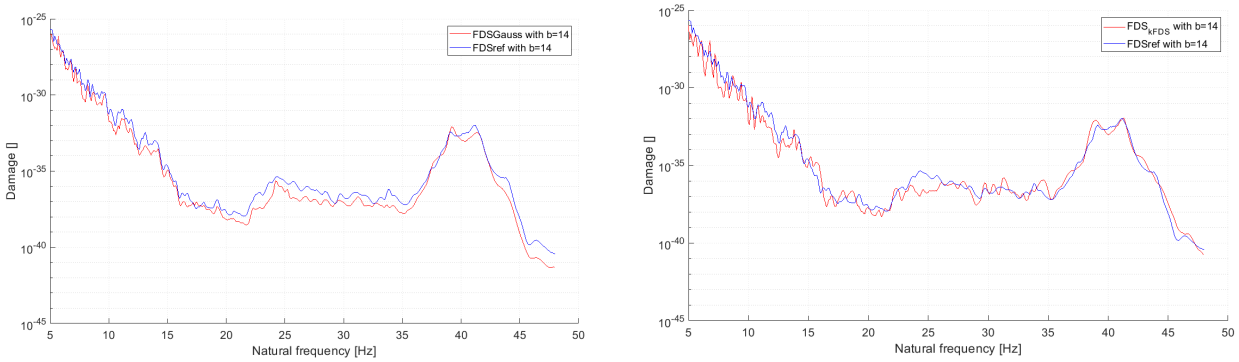

(a) (b)

Fig.4.27: comparison between the *FDS* of the reference signal of subsection 4.1.1 and that of the signal synthesized by a) the standard practice as described in subsection 4.3.2 b) the *kFDS* algorithm as described in subsection 4.3.3. The curves are calculated by considering the parameters of the model to be: $b = 14, \zeta = 0.01$

5 Conclusions

In this work kurtosis control algorithms were first revised. As is, kurtosis control does not take into account a signal's damage potential, which is estimated via the *FDS*, but only controls the *PSD* and kurtosis value; therefore, different signals with same kurtosis value and *PSD* may have a different *FDS*. In fact, it was shown that this is usually the case. However, this difference could be corrected, by using a filter described in the literature, therefore extending kurtosis control to durability tests (or fatigue life tests). The profiles so obtained not only had a target *FDS*, but also similar probability distributions to those generated by kurtosis control algorithms. The *PSD* and the statistical parameters changed to some extent but in return, the *FDS* was closer to that of the application.

In addition, four novel Mission Synthesis algorithms were proposed, which achieved to control the *FDS* (a priori, without filtering) and other parameters specific to the particular algorithm selected. Their commonality was the synthesis of leptokurtic signals, thus extending the Standard Procedure and the other methodology based on the filtering technique described in the literature.

A first algorithm, named *kFDS*, managed to control both the *FDS* and kurtosis value of a signal to be synthesized. Other three algorithms were devised and proposed: an algorithm named *RF* complied with a prescribed *FDS* and *RMS* value of a synthesized signal, irrespective of the possible time reduction factor applied to the test. Next, the *PF* algorithm was introduced, which added the possibility of controlling the *PSD* shape in addition to the *FDS* and *RMS* value. Finally, the *PSF* algorithm was a modified version of the *PF* algorithm, which omitted to control the *RMS* value and complied only with an *FDS* and a *PSD* shape specification.

The simulation results showed that the algorithms complied with the constraints they were designed to satisfy.

The main advantages of the methodologies are related both to their effectiveness and to the computational efficiency due to the simple mathematical formulae required, with the time-domain calculations being performed only to generate the time-series at the end of the procedure and calculate the *FDS*.

Another important aspect to highlight is the randomness of the synthesized profiles; in fact, the generation of Gaussian blocks implied that the phases were randomly selected. In addition, other features adding to the randomness of the profiles were: the modulation coefficients v_j in the *kFDS* and *RF* algorithms, selected randomly as well, and the random permutation of the blocks which are then concatenated and smoothed.

A possible limitation is related to the maximum values of the system response, which are greater than those reached in Gaussian tests. This problem becomes more and more evident when the duration of the test is reduced, especially for those algorithms that control the *RMS* value (*RF* and *PF*), therefore before performing the actual tests it is essential to check whether the type of failure does not change from fatigue related to yield strength related. In general, there is certainly less room to reduce the test duration with respect to Gaussian tests, but one must also consider reliability of the tests, which may be increased if the distribution of signals measured from real applications (often non-Gaussian) is preserved. The possible increase in reliability was exemplified by the experimental tests described, where an extensive experimental campaign was conducted to test the validity of one of the algorithms in actual experiments. In particular, the *kFDS* algorithm was selected for the tests. The Gaussian synthesis led to overtesting the specimens, because the mean *TTF* was about 32 % less than the expected theoretical value. On the other hand, the *kFDS* algorithm's mean *TTF* was much closer: in fact, the estimation was off by 5% approximately. This better match might be due to such factors as the small amplitudes' contribution in the reference signal, which were possibly below the fatigue limit

of the material. In fact, these low amplitudes are still damaging according to the model, even if to a small degree, therefore still contributing to the *FDS* and possibly leading to overtesting the material when the Gaussian signal is synthesized from the *FDS*. On the other hand, the *kFDS* algorithm synthesizes a signal with the same kurtosis value and *FDS* as the reference signal, thus characterized approximately by the same amount of downtime, possibly 'cancelling' the effect of damage overestimation that may occur when Gaussian tests are performed. The experimental results were promising, therefore supporting the idea that the preservation of the reference signal's nature and damage potential can make accelerated tests increasingly realistic and reliable.

The *kFDS* algorithm was chosen for the experimental tests because among the algorithms presented, it is the one which has the lowest probability of generating signals having exceedingly high *MRS* levels (especially when tests are accelerated). Besides, very high peaks may not only change the failure mechanism, but also render the synthesis procedure more sensitive to the accuracy of Wohler's curve parameters, due to the exponential relation between the signals and the damage according to the theory adopted.

Notwithstanding the hope that the results presented in this work might be helpful to the current state of the art, there are still several algorithms presented in this work which can be experimentally tested. The possibility of optimizing the synthesis procedure, by considering both the algorithms and the sensitivity to the synthesis parameters, is a tangible and foreseeable possibility.

Another important result obtained in this work was a novel time-domain method for the estimation of the fatigue damage (Appendix F). It aimed to bridge the gap between time-domain and frequency-domain approaches, in order to exploit the advantages of the frequency-domain approach (i.e. fast computations) in the time-domain, which, on its part, has the advantage of being more reliable and boasts a greater range of applicability.
The results proved to be satisfactory both in terms of precision and computational requirements, improving the speed with respect to the standard methodology, with the improvement being emphasized for long time-series.

6 References

[1] J.M Hu, D. Baker, A. Dasgupta, A. Arora, *Role of Failure-Mechanism Identification in Accelerated Testing*, Journal of the lES. Vol. XXXVI, No. 4, pp. 39-45 (1993)

[2] W. Nelson, *Accelerated Testing*, Wiley, New York (1990)

[3] Y.-L. Lee, H.-T. Kang, *Vibration Fatigue Testing and Analysis*, Ch. 9 in Y.-L. Lee, M.E. Barkey, H.-T. Kang, Eds., Metal Fatigue Analysis Handbook: Practical Problem-Solving Techniques for Computer-Aided Engineering, Waltham, MA, USA, Butterworth-Heinemann/Elsevier (2011)

[4] US Department of Defense, *MIL-STD-810G*, Test Method Standard for Environmental Engineering Considerations and Laboratory Tests (2008)

[5] E.A. Sloane, C.L. Heizman, *Vibration Control System*, US Patent 3,848,115 (1974)

[6] K. Ueno, K. Imoto, *Vibration Control System*, US Patent 5,012,428 (1991)

[7] W.H. Connon, *Comments on Kurtosis of Military Vehicle Vibration Data,* Journal of the Institute of Environmental Sciences, September/October (1991)

[8] D. Charles, *Derivation of environment descriptions and test severities from measured road transportation data,* Environmental Engineering (1992)

[9] J. Giacomin, S. Steinwolf, W.J. Staszewski, *Application of mildly nonstationary mission synthesis (MNMS) to automotive road data*, Engineering Integrity, vol. 7, pp. 44-56 (2000)

[10] A. Steinwolf, *Random Vibration Testing Beyond PSD Limitations*, Sound and Vibration, Vol. 40 (2006)

[11] A. Steinwolf, *Approximation and simulation of probability distributions with a variable kurtosis value,* Computational Statistics and Data Analysis,21 (2),163-180 (1996)

[12] A. Steinwolf, W.H. Connon, *Limitations on the use of Fourier Transform Approach to Describe Test Course Profiles*, Sound And Vibration (2005)

[13] A. Steinwolf, *Two methods for random shaker testing with low kurtosis*, Sound and Vibration, Vol.42, No. 10, pp 18-22, (2008)

[14] A. Steinwolf, *Vibration testing of vehicle components by random excitations with increased kurtosis*, Int. J. Vehicle Noise and Vibration (2015)

[15] A. Steinwolf, B. Peeters, H. Van der Auweraer, *Two methods of generating random excitations with increased kurtosis for in-house testing of vehicle components*, Proceedings of The 22nd International Congress on Sound and Vibration, Florence, Italy, (2015)

[16] E. Pesaresi, *Leptokurtic signals in random control vibration testing,* MSc Thesis in Mechanical Engineering, University of Bologna *(2017)*

[17] E. Pesaresi, M. Troncossi, *'Synthesis of vibration signals with prescribed power spectral density and kurtosis value'*, Proceedings of ISMA2018, September 17-19, Leuven, Belgium, (2018)

[18] J. Minderhoud, P. Van Baren, *Using Kurtosion® to Accelerate Structural Life Testing,* Sound And Vibration, Vol.44 (2010)

[19] F. Kihm, N. S. Ferguson, J. Antoni, *Fatigue life from kurtosis controlled excitations,* 6th Fatigue Design conference, Fatigue Design (2015)

[20] J. Zhang, B. Cornelis, B. Peeters, K. Janssens, P. Guillaume, *A new practical and intuitive method for kurtosis control in random vibration testing,* ISMA 2016 Conference, Leuven, Belgium (2016)

[21] S.R. Winterstein, *Nonlinear vibration models for extremes and fatigue,* ASCE Journal of Engineering Mechanics, Vol.114, No. 10 (1988)

[22] R.G. Merritt, *A stochastic model for the pulse method – Part 2: random part,* in Proceedings of the 43rd IEST Annual Technical Meeting, Los Angeles (1997)

[23] D.O. Smallwood, *Generating non-Gaussian vibration for testing purposes,* Sound and Vibrations, Vol.39, No. 10 (2005)

[24] R.P. Hamernik, K.D. Hsueh, *A generalized approach to random noise synthesis: theory and computer simulation*, Journal of the Acoustical Society of America, Vol.87 No.3, pp- 1207-1217 (1990)

[25] B. Cornelis, A. Steinwolf, M. Troncossi, A. Rivola, *Shaker testing simulation of non-Gaussian random excitations with the fatigue damage spectrum as a criterion of mission signal synthesis,* Proceedings of the 2015 International Conference on Engineering, Ljubljana, Slovenia *(2015)*

[26] A. Papoulis, *Narrow-Band systems and Gaussianity,* IEEE Trans. On Information Theory, Vol.18, No.1 *(1972)*

[27] F. Kihm, S. A. Rizzi, N.S. Ferguson, A. Halfpenny, *Understanding how kurtosis is transferred from input acceleration to stress response and its influence on fatigue life,* in Proceedings of 11th International Conference *RASD*, Pisa (Italy), July 1-3 (2013)

[28] S. Rizzi, M.N. Behnke, and A. Przekop, *The effect of a non-Gaussian random loading on high-cycle fatigue of a thermally post-buckled structure*, Structural Dynamics: Recent Advances, Proceedings of the 10th International Conference, Paper 26, Southampton, UK, July 12-14 (2010)

[29] A. Steinwolf, and S.A Rizzi, *Non-gaussian analysis of turbulent boundary layer fluctuating pressure on aircraft skin panels*, AIAA Journal of Aircraft, Vol. 43, No. 6, pp. 1662-1675 (2006)

[30] S. Rizzi, A. Przekop, T. Turner, *On the Response of a Nonlinear Structure to High Kurtosis Non-Gaussian Random Loadings,* Proceedings of The 8th International Conference on Structural Dynamics (EURODYN), Leuven, Belgium (2011)

[31] M. Troncossi, A. Rivola, *Response analysis of specimens excited with non-Gaussian acceleration profiles,* Proc. 26th Int. Conf. Noise and Vibration Engineering – ISMA2014, Leuven (Belgium), pp. 799-808, September 15-17 (2014)

[32] J. J. Van Baren, P. Van Baren, *Kurtosion*tm*-getting the kurtosis into the resonances,* SAVIAC (2007)

[33] A. Papoulis, *Probability, Random Variables, and Stochastic Processes,* McGraw-Hill, 3rd ed. *(1991)*

[34] F. Kihm, A. Halfpenny and K. Munson, *Synthesis of Accelerated and More Realistic Vibration Endurance Tests Using Kurtosis*, SAE Technical Paper 2016-01-0275, (2016)

[35] M. Troncossi, R. Cipollini, A. Rivola, *Experimental Evaluation of the FDS-based Equivalence Approach for the Mission Synthesis in Accelerated Life Tests,* Proc. International Conference on Sound & Vibration (ICSV), Bangkok (Thailand), Jul. 7-11 (2013)

[36] C. Lalanne, *Mechanical Vibration and Shock Analysis-Volume 4: Fatigue Damage,* John Wiley & Sons, Inc-ISTE, London (2009)

[37] T. Svensson, H.O. Torstensson, *Utilization of fatigue damage response spectrum in the evaluation of transport stresses*. Proceedings, Annual Technical Meeting - Institute of Environmental Sciences 2, 191-194 (1993)

[38] G. R. Henderson, A. G. Piersol, *Fatigue Damage Related Descriptor for Random Vibration Test Environments*, Sound & Vibration, p. 21, October (1995)

[39] S. I. McNeill 2008 *Implementing the Fatigue Damage Spectrum and Fatigue Damage Equivalent Vibration Testing* 79th Shock & Vibration Symposium Orlando Florida October 26-30

[40] C. Lalanne, *Mechanical Vibration and Shock Analysis-Volume 5: Specification Development,* John Wiley & Sons, Inc-ISTE, London (2009)

[41] C. Lalanne, *Mechanical Vibration and Shock Analysis-Volume 3: Random Vibration,* John Wiley & Sons, Inc-ISTE, London (2009)

[42] A.G. Piersol, Accelerated Vibration Testing - Proceed with caution, Tustin Training News (1993)

[43] G.M. Hieber, *Use and Abuse of Test Time Exaggeration Factors*, TEST Engineering and Management, pp. 14-16, Apr/May (1999)

[44] D. Benasciutti and R. Tovo Spectral methods for lifetime prediction under wide-band stationary random processes *Int. J. Fatigue* **27** (2005)

[45] M. Mrsnik, J. Slavic and M. Boltezar Frequency-domain methods for a vibration-fatigue-life estimation -Application to real data *International Journal of Fatigue* **47** pp 8-17 DOI: 10.1016/j.ijfatigue.2012.07.005 (2013)

[46] F. Cianetti, M. Palmieri, C. Braccesi and G. Morettini *Correction formula approach to evaluate fatigue damage induced by non-Gaussian stress state,* AIAS International Conference on Stress Analysis (2017)

[47] D. Benasciutti, and R. Tovo *Fatigue life assessment in non-Gaussian random loadings*. *International Journal of Fatigue* **28** pp 733-746 (2006)

[48] C. Braccesi, F. Cianetti, G. Lori and D. Pioli, *The frequency domain approach in virtual fatigue estimation of non-linear systems: The problem of non-Gaussian states of stress*. International Journal of Fatigue **31** pp 766-775 (2009)

[49] A. Niesłony, M. Böhm, T. Łagoda and F. Cianetti The use of spectral methods for fatigue life assessment for non-Gaussian random loads. *Acta mechanica et automatica* **10** pp 100-103 (2016)

[50] K. Ahlin, *Shock Response Spectrum Calculation – An Improvement of the Smallwood Algorithm* 70th Shock and Vibration Symposium, Albuquerque, NM, November 15-19, (1999)

[51] J. Antoni, R.B. Randall *The spectral kurtosis: application to the vibratory surveillance and diagnostics of rotating machines* Mechanical Systems and Signal Processing, Elsevier (2006)

[52] R.F. Dwyer, *Detection of non-Gaussian signals by frequency domain kurtosis estimation*, in: International Conference on Acoustic, Speech, and Signal Processing, Boston, pp. 607–610 (1983)

[53] M. Troncossi, E. Pesaresi, "Analysis of synthesized non-Gaussian excitations for vibration-based fatigue life testing", *Proceedings of RASD2019*, April 15-17, Lyon, France (2019)

[54] J. Antoni, *Fast computation of the kurtogram for the detection of transient faults,* Mechanical Systems and Signal Processing, Elsevier (2007)

[55] L. Capponi, M. Česnik, J. Slavič, F. Cianetti, M. Boltežar. *Non-stationarity index in vibration fatigue: Theoretical and experimental research*. International Journal of Fatigue (104):221-230 (2017)

[56] M.A. Miner, *Cumulative Damage in Fatigue*, J. Applied Mechanics, Vol. 67, A159-A164 (1945)

[57] W. Mendenhall, R.J. Beaver and B. M. Beaver *Introduction to Probability and Statistics* Thomson Brooks/Cole p 159 (2005)

[58] M. J. Schervish *Theory of Statistics* Springer (1995)

[59] J. J. Schiller and S. Lipschutz *Schaum's Outline of Probability, Second Edition*, McGraw–Hill Professional, p 89 (2010)

[60] H. C. Tijms *A First Course in Stochastic Models*, John Wiley and Sons, pp 431–432 (2003)

[61] A. Gut *An Intermediate Course in Probability* Springer, pp 5–6 (1995)

[62] W. Zhao and M. J. Baker On the probability density function of rainflow stress range for stationary Gaussian processes. *International Journal of Fatigue* **14** pp 121-135 (1992)

[63] M. Matsuishi, T. Endo, *Fatigue of metals subjected to varying stress*, Japan Society of Mechanical Engineers, Fukuoka, Japan (1968)

[64] A. Seçil, *Fatigue Life Calculation by Rainflow Cycle Counting Method*, thesis submitted to the Graduate School of Natural and Applied Sciences of Middle East Technical University, December (2004)

[65] A. Nieslony Rainflow Counting Algorithm (https://www.mathworks.com/matlabcentral/fileexchange/3026-rainflow-counting-algorithm), MATLAB Central File Exchange. Retrieved September 2, (2020)

[66] J.M. Barsom, and S.T. Rolfe, *Fracture and Fatigue Control in Structures*, 2nd edition , Prentice-Hall. Englewood Cliffs , NJ (1987)

[67] S.R. Boyer, *Atlas of Fatigue Curves*, American Society of Metals, Metals Park, OH (1986)

[68] J. Symonds, *Mechanical Properties of Materials* Ch.5, Mark's Standard Handbook for Mechanical Engineers (editors: E. A. Avallone and T. Baumeister III). 9th edition. McGraw-Hill, New York, pp. 5 – 9 (1987)

Appendix A: formulae for moments

Every periodic signal $x(t)$ can be expanded in a Fourier series:

$$x(t) = \frac{a_0}{2} + \sum_{n=1}^{\infty} (a_n \cos\omega_n t + b_n sin\omega_n t) \quad (A.1)$$

or if the series is truncated to N terms, as for shaker drive signals:

$$x(t) = \frac{a_0}{2} + \sum_{n=1}^{N} (a_n \cos\omega_n t + b_n sin\omega_n t) \quad (A.2)$$

$$\omega_n = 2\pi\Delta f n = \frac{2\pi n}{T} \quad (A.3)$$

where $\Delta f = \frac{1}{T}$ is the frequency resolution and T is the duration of the signal, which is considered to be extended periodically outside the interval $[0, T]$.

The coefficients are expressible in terms of the signal $x(t)$ according to the relations:

$$\frac{a_n}{2} = \frac{1}{T}\int_0^T x(t)\cos\omega_n t \, dt \quad (A.4)$$

$$\frac{b_n}{2} = \frac{1}{T}\int_0^T x(t)\sin\omega_n t \, dt \quad (A.5)$$

$$n \in \{k \in \mathbb{N} \,|0 \leq k \leq N\}$$

If other coefficients A_n, φ_n are defined such that:

$$a_n = A_n \cos\varphi_n \quad (A.6)$$

$$b_n = -A_n \sin\varphi_n \quad (A.7)$$

the series can be easily written as:

$$x(t) = \frac{a_0}{2} + \sum_{n=1}^{N} A_n \cos(\omega_n t + \varphi_n) \tag{A.8}$$

Besides, it can be written in complex form as well:

$$a_n \cos\omega_n t + b_n sin\omega_n t = a_n \frac{e^{j\omega_n t} + e^{-j\omega_n t}}{2} + b_n \frac{e^{j\omega_n t} - e^{-j\omega_n t}}{2j}$$
$$= \frac{a_n - jb_n}{2} e^{j\omega_n t} + \frac{a_n + jb_n}{2} e^{-j\omega_n t} = c_n e^{j\omega_n t} + {c^*}_n e^{-j\omega_n t}$$

where:

$$c_n = \frac{a_n - jb_n}{2} \tag{A.9}$$

and ${c^*}_n$ is its complex conjugate, which is also equal to c_{-n} because for a real-valued signal $x(t)$:

$$a_{-n} = a_n \tag{A.10}$$

$$b_{-n} = -b_n \tag{A.11}$$

$$A_{-n} = A_n \tag{A.12}$$

$$\varphi_{-n} = -\varphi_n \tag{A.13}$$

With the above definition of c_n, the series can be written as:

$$\frac{a_0}{2} + \sum_{n=1}^{N} (a_n \cos\omega_n t + b_n sin\omega_n t) = c_0 + \sum_{n=1}^{N} (c_n e^{j\omega_n t} + {c^*}_n e^{-j\omega_n t})$$
$$= c_0 + \sum_{n=1}^{N} c_n e^{j\omega_n t} + \sum_{n=1}^{N} c_{-n} e^{-j\omega_n t} = c_0 + \sum_{n=1}^{N} c_n e^{j\omega_n t} + \sum_{n=-N}^{-1} c_n e^{j\omega_n t}$$
$$= \sum_{n=-N}^{N} c_n e^{j\omega_n t}$$

Hence:

$$x(t) = \sum_{n=-N}^{N} c_n \mathrm{e}^{j\omega_n t} \tag{A.14}$$

where:

$$c_0 = \frac{a_0}{2} = \frac{A_0}{2} \tag{A.15}$$

$$\varphi_0 = 0, b_0 = 0 \tag{A.16}$$

$$c_n = \frac{1}{T}\int_0^T x(t)\mathrm{e}^{-j\omega_n t}\, dt = \frac{A_n}{2} e^{j\varphi_n} \tag{A.17}$$

It should be noted that the indices could be defined either to assume both negative and positive values as in Eq.(A.14) or only positive values Eq.(A.1).
In the time domain the central moment of order q (where q is a non-negative integer) is:

$$\mathrm{M}_q = \frac{1}{T}\int_0^T (x(t) - c_0)^q \, dt \tag{A.18}$$

Its calculation in terms of the amplitudes and phases of the signal yields:

$$\mathrm{M}_q = \frac{1}{T}\int_0^T (x(t) - c_0)^q \, dt = \frac{1}{T}\int_0^T \prod_{k=1}^{q} \sum_{n_k \neq 0} c_{n_k} \mathrm{e}^{j\omega_{n_k} t} \, dt =$$

$$= \frac{1}{T}\int_0^T \sum_{n_1 \neq 0, n_2 \neq 0, \ldots, n_q \neq 0} \left(\prod_{k=1}^{q} c_{n_k} \right) \mathrm{e}^{j\sum_{k=1}^{q} \omega_{n_k} t} \, dt =$$

$$\sum_{n_1 \neq 0, n_2 \neq 0, \ldots, n_q \neq 0} \left(\prod_{k=1}^{q} c_{n_k} \right) \frac{1}{T}\int_0^T \mathrm{e}^{j\sum_{l=1}^{q} \omega_{n_l} t} dt$$

which, for the periodicity of the complex exponentials and after substituting the expressions for ω_{n_l} becomes:

$$\mathrm{M}_q = \sum_{\substack{n_1+n_2+\cdots+n_q=0 \\ n_1 \neq 0, n_2 \neq 0, \ldots, n_q \neq 0}} \prod_{k=1}^{q} c_{n_k} = \sum_{\substack{n_1+n_2+\cdots+n_q=0 \\ n_1 \neq 0, n_2 \neq 0, \ldots, n_q \neq 0}} \prod_{k=1}^{q} \left(\frac{A_{n_k}}{2} e^{j\varphi_{n_k}} \right) =$$

$$= \sum_{\substack{n_1+n_2+\cdots+n_q=0 \\ n_1 \neq 0, n_2 \neq 0, \ldots, n_q \neq 0}} \left(\prod_{k=1}^{q} \frac{A_{n_k}}{2} \right) e^{j\sum_{l=1}^{q} \varphi_{n_l}} =$$

$$= \sum_{\substack{n_1+n_2+\cdots+n_q=0 \\ n_1 \neq 0, n_2 \neq 0, \ldots, n_q \neq 0}} \left(\prod_{k=1}^{q} \frac{A_{n_k}}{2} \right) \Re\left(e^{j\sum_{l=1}^{q} \varphi_{n_l}} \right) =$$

$$= \sum_{\substack{n_1+n_2+\cdots+n_q=0 \\ n_1\neq 0, n_2\neq 0, \ldots, n_q\neq 0}} \frac{1}{2^q}\left(\prod_{k=1}^{q} A_{n_k}\right)\cos\left(\sum_{l=1}^{q}\varphi_{n_l}\right) =$$

$$= \sum_{\substack{n_1+n_2+\cdots+n_q=0 \\ n_1\neq 0, n_2\neq 0, \ldots, n_q\neq 0}} \frac{1}{2^q} A_{n_1}A_{n_2}\ldots A_{n_q}\cos\left(\varphi_{n_1}+\varphi_{n_2}+\cdots+\varphi_{n_q}\right)$$

Hence:

$$\mathrm{M}_q = \sum_{\substack{n_1+n_2+\cdots+n_q=0 \\ n_1\neq 0, n_2\neq 0, \ldots, n_q\neq 0}} \frac{1}{2^q} A_{n_1}A_{n_2}\ldots A_{n_q}\cos\left(\varphi_{n_1}+\varphi_{n_2}+\cdots+\varphi_{n_q}\right) \qquad (A.19)$$

If $q = 2$:

$$\mathrm{M}_2 = \frac{1}{4}\sum_{\substack{n+k=0 \\ n\neq 0}} A_n A_k \cos(\varphi_n+\varphi_k) = \frac{1}{4}\sum_{\substack{n \\ n\neq 0}} {A_n}^2 = \frac{1}{4}\sum_{n>0} {A_n}^2 + \frac{1}{4}\sum_{n<0} {A_n}^2 =$$

$$= \frac{1}{2}\sum_{n>0} {A_n}^2 \qquad (A.20)$$

If $q = 4$ one obtains:

$$\mathrm{M}_4 = \frac{1}{16}\sum_{\substack{n+k+l+m=0 \\ n\neq 0, k\neq 0, l\neq 0, m\neq 0}} A_n A_k A_l A_m \cos(\varphi_n+\varphi_k+\varphi_l+\varphi_m) \qquad (A.21)$$

In Eq.(A.21) the sum of the indices can give zero only if: (i) two indices are positive and the other two negative, (ii) three are positive and one negative, (iii) three are negative and one positive. Depending on which indices are positive and which are negative there are different combinations of signs: condition (i) contains $\binom{4}{2} = \frac{4!}{2!\,2!} = 6$ such combinations, whereas conditions (ii) and (iii) considered together (in fact, they lead to the same expression) give $\binom{4}{1} + \binom{4}{3} = 2\binom{4}{1} = 8$ different possibilities. Hence:

$$\sum_{\substack{n+k+l+m=0 \\ n\neq 0, k\neq 0, l\neq 0, m\neq 0}} \ldots = 8 \sum_{\substack{n+k+l+m=0 \\ n>0, k>0, l>0, m<0}} \ldots + 6 \sum_{\substack{n+k+l+m=0 \\ n>0, k>0, l<0, m<0}} \ldots \qquad (A.22)$$

$$\mathrm{M}_4 = \sum_{\substack{n+k+l=m \\ n>0, k>0, l>0, m>0}} \frac{1}{2} A_n A_k A_l A_m \cos(\varphi_n+\varphi_k+\varphi_l-\varphi_m) +$$

$$+ \sum_{\substack{n+k=l+m \\ n>0, k>0, l>0, m>0}} \frac{3}{8} A_n A_k A_l A_m \cos(\varphi_n+\varphi_k-\varphi_l-\varphi_m) \qquad (A.23)$$

In Eq.(A.23), the indices can only assume positive values, for this reason the condition $n > 0, k > 0, l > 0, m > 0$ under every summation symbol will be omitted in order to lighten the notation, but it will remain valid henceforth in this appendix.
The summation symbols in Eq.(A.23) can be manipulated further. It can be proved that the following relations hold:

$$\sum_{n+k=l+m} \ldots = 2 \sum_{\substack{n+k=l+m \\ n=m}} \ldots - \sum_{\substack{n+k=l+m \\ n=k=l=m}} \ldots + 4 \sum_{\substack{n+k=2m \\ n<k}} \ldots + 8 \sum_{\substack{l+m=n+k \\ l<m,n<k,n<l}} \ldots \qquad (A.24)$$

$$\sum_{n+k+l=m} \ldots = \sum_{3k=m} \ldots + 3 \sum_{\substack{2n+l=m \\ n\neq l}} \ldots + 6 \sum_{\substack{n+k+l=m \\ n<l<k}} \ldots \qquad (A.25)$$

The following mathematical steps can be used to prove Eq.(A.24):

$$\sum_{n+k=l+m} \ldots = \sum_{\substack{n+k=l+m \\ n=m \\ (k=l)}} \ldots + \sum_{\substack{n+k=l+m \\ n\neq m \\ (k\neq l)}} \ldots = 2 \sum_{\substack{n+k=l+m \\ n=m \\ (k=l)}} \ldots - \sum_{\substack{n+k=l+m \\ n=m \\ (k=l)}} \ldots + \sum_{\substack{n+k=l+m \\ n\neq m \\ (k\neq l)}} \ldots =$$

$$= 2 \sum_{\substack{n+k=l+m \\ n=m \\ (k=l)}} \ldots - \sum_{\substack{n+k=l+m \\ n=m \\ k=l=m}} \ldots - \sum_{\substack{n+k=l+m \\ n=m \\ k=l\neq m}} \ldots + \sum_{\substack{n+k=l+m \\ n\neq m \\ (k\neq l)}} \ldots =$$

$$= 2 \sum_{\substack{n+k=l+m \\ n=m \\ (k=l)}} \ldots - \sum_{\substack{n+k=l+m \\ n=m \\ k=l=m}} \ldots - \sum_{\substack{n+k=l+m \\ n=m \\ k=l\neq m}} \ldots + \sum_{\substack{n+k=l+m \\ n\neq m \\ n\neq l \\ (k\neq l)}} \ldots + \sum_{\substack{n+k=l+m \\ n\neq m \\ n=l \\ (k\neq l,\ k=m)}} \ldots =$$

$$= 2 \sum_{\substack{n+k=l+m \\ n=m \\ (k=l)}} \ldots - \sum_{\substack{n+k=l+m \\ n=m \\ k=l=m}} \ldots + \sum_{\substack{n+k=l+m \\ n\neq m \\ n\neq l \\ (k\neq l)}} \ldots =$$

$$= 2 \sum_{\substack{n+k=l+m \\ n=m \\ (k=l)}} \ldots - \sum_{\substack{n+k=l+m \\ n=m \\ k=l=m}} \ldots + \sum_{\substack{n+k=l+m \\ n\neq m \\ n\neq l \\ n=k \\ (k\neq l)}} \ldots + \sum_{\substack{n+k=l+m \\ n\neq m \\ n\neq l \\ n\neq k \\ (k\neq l)}} \ldots =$$

$$= 2 \sum_{\substack{n+k=l+m \\ n=m \\ (k=l)}} \ldots - \sum_{\substack{n+k=l+m \\ n=m \\ k=l=m}} \ldots + \sum_{\substack{2n=l+m \\ n\neq m \\ (n\neq l,\ l\neq m)}} \ldots + \sum_{\substack{n+k=l+m \\ n\neq m \\ n\neq l \\ n\neq k \\ l=m \\ (k\neq l)}} \ldots + \sum_{\substack{n+k=l+m \\ n\neq m \\ n\neq l \\ n\neq k \\ l\neq m \\ (k\neq l)}} \ldots =$$

$$= 2 \sum_{\substack{n+k=l+m \\ n=m \\ (k=l)}} \ldots - \sum_{\substack{n+k=l+m \\ n=m \\ k=l=m}} \ldots + \sum_{\substack{2n=l+m \\ n\neq m \\ (n\neq l,\ l\neq m)}} \ldots + \sum_{\substack{n+k=2m \\ n\neq m \\ (k\neq m,\ n\neq k)}} \ldots + \sum_{\substack{n+k=l+m \\ n\neq m \\ n\neq k \\ l\neq m \\ (k\neq l,\ n\neq l,\ k\neq m)}} \ldots =$$

$$= 2 \sum_{\substack{n+k=l+m \\ n=m \\ (k=l)}} \ldots - \sum_{\substack{n+k=l+m \\ n=m \\ k=l=m}} \ldots + 2 \sum_{\substack{2n=l+m \\ n\neq m \\ (n\neq l,\ l\neq m)}} \ldots + \sum_{\substack{n+k=l+m \\ n\neq m \\ n\neq k \\ l\neq m \\ (k\neq l,\ n\neq l,\ k\neq m)}} \ldots =$$

$$= 2 \sum_{\substack{n+k=l+m \\ n=m}} \ldots - \sum_{\substack{n+k=l+m \\ n=m=l=k}} \ldots + 2 \sum_{\substack{2n=l+m \\ n<m}} \ldots + 2 \sum_{\substack{2n=l+m \\ n>m}} \ldots + \sum_{\substack{n+k=l+m \\ n\neq m \\ n\neq k \\ l\neq m \\ (k\neq l,\ n\neq l,\ k\neq m)}} \ldots =$$

$$= 2 \sum_{\substack{n+k=l+m \\ n=m}} \ldots - \sum_{\substack{n+k=l+m \\ n=m=l=k}} \ldots + 4 \sum_{\substack{2n=l+m \\ n<m}} \ldots + 8 \sum_{\substack{n+k=l+m \\ n<l<m<k}} \ldots =$$

$$= 2 \sum_{\substack{n+k=l+m \\ n=m}} \ldots - \sum_{\substack{n+k=l+m \\ n=m=l=k}} \ldots + 4 \sum_{\substack{2n=l+m \\ l<m}} \ldots + 8 \sum_{\substack{n+k=l+m \\ l<m,\ n<k,\ n<l}} \ldots =$$

$$= 2 \sum_{\substack{n+k=l+m \\ n=m}} \ldots - \sum_{\substack{n+k=l+m \\ n=m=l=k}} \ldots + 4 \sum_{\substack{2m=k+n \\ n<k}} \ldots + 8 \sum_{\substack{n+k=l+m \\ l<m,\ n<k,\ n<l}} \ldots \quad (\text{Q. E. D})$$

The following mathematical steps can be used to prove Eq.(A.25):

$$\sum_{n+k+l=m} \ldots = \sum_{\substack{n+k+l=m \\ n=k}} \ldots + \sum_{\substack{n+k+l=m \\ n\neq k}} \ldots =$$

$$= \sum_{\substack{n+k+l=m \\ n=k \\ k=l}} \ldots + \sum_{\substack{n+k+l=m \\ n=k \\ k\neq l}} \ldots + \sum_{\substack{n+k+l=m \\ n\neq k \\ k=l}} \ldots + \sum_{\substack{n+k+l=m \\ n\neq k \\ k\neq l}} \ldots =$$

$$= \sum_{\substack{n+k+l=m \\ n=k \\ k=l}} \ldots + 2 \sum_{\substack{n+k+l=m \\ n=k \\ k\neq l}} \ldots + \sum_{\substack{n+k+l=m \\ n\neq k \\ k\neq l}} \ldots =$$

$$= \sum_{\substack{n+k+l=m \\ n=k \\ k=l}} \ldots + 2 \sum_{\substack{n+k+l=m \\ n=k \\ k\neq l \\ (n\neq l)}} \ldots + \sum_{\substack{n+k+l=m \\ n\neq k \\ k\neq l \\ n=l}} \ldots + \sum_{\substack{n+k+l=m \\ n\neq k \\ k\neq l \\ n\neq l}} \ldots =$$

$$= \sum_{\substack{n+k+l=m \\ n=k \\ k=l}} \ldots + 3 \sum_{\substack{n+k+l=m \\ n=k \\ k\neq l \\ (n\neq l)}} \ldots + \sum_{\substack{n+k+l=m \\ n\neq k \\ k\neq l \\ n\neq l}} \ldots =$$

$$= \sum_{3k=m} \ldots + 3 \sum_{\substack{2k+l=m \\ k\neq l}} \ldots + \sum_{\substack{n+k+l=m \\ n\neq k \\ k\neq l \\ n\neq l}} \ldots =$$

$$= \sum_{3k=m} \ldots + 3 \sum_{\substack{2k+l=m \\ k\neq l}} \ldots + 3! \sum_{\substack{n+k+l=m \\ n<l<k}} \ldots =$$

$$= \sum_{3k=m} \ldots + 3 \sum_{\substack{2n+l=m \\ n\neq l}} \ldots + 6 \sum_{\substack{n+k+l=m \\ n<l<k}} \ldots \quad \text{(Q. E. D)}$$

Substituting Eqs.(A.24, A.25) into Eq.(A.23):

$$\begin{aligned} \mathrm{M}_4 = 3{M_2}^2 - \frac{3}{8}\sum_n {A_n}^4 + 3 \sum_{\substack{l+m=n+k \\ l<m, n<k, n<l}} A_n A_k A_l A_m \cos(\varphi_n + \varphi_k - \varphi_l - \varphi_m) \\ + 3 \sum_{\substack{n+k+l=m \\ n<l<k}} A_n A_k A_l A_m \cos(\varphi_n + \varphi_k + \varphi_l - \varphi_m) \\ + \frac{1}{2} \sum_{3k=m} {A_k}^3 A_m \cos(3\varphi_k - \varphi_m) \\ + \frac{3}{2} \sum_{\substack{2n+l=m \\ n\neq l}} {A_n}^2 A_l A_m \cos(2\varphi_n + \varphi_l - \varphi_m) \\ + \frac{3}{2} \sum_{\substack{n+k=2m \\ n<k}} A_n A_k {A_m}^2 \cos(\varphi_n + \varphi_k - 2\varphi_m) \end{aligned} \qquad (A.26)$$

which is equivalent to Eqs.(A.21, A.23).
One should remember that in Eq.(A.21) the indices range from $-N$ to N while in Eqs.(A.23, A.26) from 1 to N.

Appendix B: Gaussian distribution from its moments

The probability density function can be recovered from the knowledge of its moments, according to Eq.(1.21), recalled in the following for convenience:

$$p(x) = \frac{1}{2\pi}\int_{-\infty}^{+\infty}\sum_{q=0}^{\infty}(-j\omega)^q\frac{M_q}{q!}e^{j\omega(x-c_0)}d\omega$$

If the moments are given by Eqs.(1.16, 1.18), namely:

$$\begin{cases} M_q = (q-1)!!\,{M_2}^{\frac{q}{2}} & if\ q\ even \\ M_q = 0 & if\ q\ odd \end{cases}$$

then, the calculation of $p(x)$ yields:

$$p(x) = \frac{1}{2\pi}\int_{-\infty}^{+\infty}\sum_{q=0}^{\infty}(-j\omega)^q\frac{M_q}{q!}e^{j\omega(x-c_0)}d\omega =$$

$$= \frac{1}{2\pi}\int_{-\infty}^{+\infty}\sum_{q\ even}(-\omega^2)^{\frac{q}{2}}\frac{(q-1)!!\,{M_2}^{\frac{q}{2}}}{q!}e^{j\omega(x-c_0)}d\omega$$

For well-known properties of the double factorial:

$$(q-1)!! = \frac{q!}{2^{\frac{q}{2}}\left(\frac{q}{2}\right)!} \qquad if\ q\ even$$

The former relation is trivial to prove, in fact:

$$(q-1)!! = (q-1)(q-3)(q-5)\dots 3\cdot 1 = \frac{q(q-1)(q-2)(q-3)(q-4)(q-5)\dots 3\cdot 2\cdot 1}{q(q-2)(q-4)\dots 2} =$$

$$= \frac{q!}{2\cdot\frac{q}{2}\cdot 2\cdot\left(\frac{q}{2}-1\right)\cdot 2\cdot\left(\frac{q}{2}-2\right)\dots 2\cdot 1} = \frac{q!}{2^{\frac{q}{2}}\frac{q}{2}\left(\frac{q}{2}-1\right)\left(\frac{q}{2}-2\right)\dots 1} = \frac{q!}{2^{\frac{q}{2}}\left(\frac{q}{2}\right)!}\ (Q.E.D)$$

Hence:

$$p(x) = \frac{1}{2\pi}\int_{-\infty}^{+\infty}\sum_{q\ even}\frac{\left(\frac{-\omega^2 M_2}{2}\right)^{\frac{q}{2}}}{\left(\frac{q}{2}\right)!}e^{j\omega(x-c_0)}d\omega =$$

$$= \frac{1}{2\pi}\int_{-\infty}^{+\infty}e^{\frac{-\omega^2 M_2}{2}}e^{j\omega(x-c_0)}d\omega =$$

$$= \frac{1}{2\pi}\int_{-\infty}^{+\infty}e^{-\left[\omega\sqrt{\frac{M_2}{2}}-\frac{j(x-c_0)}{\sqrt{2M_2}}\right]^2-\frac{(x-c_0)^2}{2M_2}}d\omega =$$

$$= \frac{1}{2\pi}\sqrt{\frac{2}{M_2}}e^{-\frac{(x-c_0)^2}{2M_2}}\int_{-\infty}^{+\infty} e^{-\chi^2}\, d\chi$$

The last integral is known to be equal to $\sqrt{\pi}$, in fact:

$$\int_{-\infty}^{+\infty} e^{-\chi^2} d\chi = \left(\int_{-\infty}^{+\infty} e^{-t^2} dt\right)^{1/2}\left(\int_{-\infty}^{+\infty} e^{-z^2} dz\right)^{1/2}$$

$$= \left(\int_{-\infty}^{+\infty}\int_{-\infty}^{+\infty} e^{-(z^2+t^2)}\, dzdt\right)^{1/2} = \left(\int_0^{2\pi}\int_0^{+\infty} e^{-\rho^2}\,\rho d\rho d\theta\right)^{1/2} =$$

$$= \left(\int_0^{2\pi}\left[\frac{e^{-\rho^2}}{-2}\right]_0^{+\infty} d\theta\right)^{1/2} = \sqrt{\pi}$$

Hence:

$$p(x) = \frac{1}{\sqrt{2\pi M_2}}e^{-\frac{(x-c_0)^2}{2M_2}}$$

which is the well-known Gaussian probability density function.

Appendix C: distribution of a sinusoid from its moments

The probability density function of a sinusoid can be recovered from the knowledge of its moments, given by Eqs,(1.22, 1.23), recalled in the following for convenience:

$$\begin{cases} M_q = \binom{q}{q/2}\frac{A^q}{2^q} & if\ q\ even \\ M_q = 0 & if\ q\ odd \end{cases}$$

and by using Eq.(1.21) with $c_0 = 0$, $p(x)$ is given by:

$$p(x) = \frac{1}{2\pi}\int_{-\infty}^{+\infty}\sum_{q=0}^{\infty}(-j\omega)^q\frac{M_q}{q!}e^{j\omega x}d\omega$$

The calculation of $p(x)$ yields:

$$p(x) = \frac{1}{2\pi}\int_{-\infty}^{+\infty}\sum_{q\ even}(-j\omega)^q\frac{\binom{q}{q/2}\frac{A^q}{2^q}}{q!}e^{j\omega x}d\omega =$$

$$= \frac{1}{2\pi}\int_{-\infty}^{+\infty}\sum_{q\ even}(-j\omega)^q\frac{A^q}{\left((q/2)!\right)^2 2^q}e^{j\omega x}d\omega =$$

$$= \frac{1}{2\pi}\int_{-\infty}^{+\infty}\sum_{q\ even}\frac{\left(-\frac{\omega^2A^2}{4}\right)^{q/2}}{\left((q/2)!\right)^2}e^{j\omega x}d\omega$$

The series inside the integral is related to the Bessel function of order zero, in particular:

$$J_0(A\omega) \triangleq \sum_{q\ even}\frac{\left(-\frac{(A\omega)^2}{4}\right)^{\frac{q}{2}}}{\left(\left(\frac{q}{2}\right)!\right)^2} = \sum_{q=0}^{\infty}\frac{\left(-\frac{(A\omega)^2}{4}\right)^q}{(q!)^2} \qquad (C.1)$$

The Bessel function of order zero also has a useful integral representation:

$$J_0(A\omega) \triangleq \int_{-A}^{A}\frac{1}{\pi}\frac{e^{-j\omega x}}{\sqrt{A^2 - x^2}}dx \qquad (C.2)$$

It can be proved that Eq.$(C.2)$ coincides with the series representation given by Eq.$(C.1)$; in fact, by making the substitution $x = A\ cos(t)$:

$$J_0(A\omega) = \int_{\pi}^{0} -\frac{1}{\pi}\frac{e^{-j\omega A\ cos(t)}}{A\ sin(t)}A\ sin(t)dt =$$

$$= \frac{1}{\pi}\int_0^{\pi}e^{-j\omega A\ cos(t)}\,dt \qquad (C.3)$$

Then, by expanding the integrand $e^{-j\omega A\cos(t)}$ according to the theory of complex variables:

$$J_0(A\omega) = \frac{1}{\pi}\int_0^{\pi} e^{-j\omega A\cos(t)}\,dt = \frac{1}{\pi}\int_0^{\pi}\sum_{q=0}^{\infty}\frac{(-j\omega A\,cos(t))^q}{q!}dt =$$

$$= \sum_{q=0}^{\infty}\left[\frac{(-j\omega A)^q}{q!}\left(\frac{1}{\pi}\int_0^{\pi} cos^q(t)\,dt\right)\right] \qquad (C.4)$$

The integral is zero when q is odd because the negative contribution in the interval $[\pi/2, \pi]$ cancels the positive one in the interval $[0, \pi/2]$. For even values of q the function $cos^q(t)$ is definitely periodic with period π, therefore the integral of $cos^q(t)$, which is none other than the moment of order q of $\cos(t)$, can be evaluated by using Eq.(A.19). In fact, the integral is the same as the one given by Eq.(A.18) with $T = \pi$ and only one harmonic contained in the signal given by Eq.(A.8) (with $a_0 = 0$ and the amplitude of the harmonic being equal to 1). It can be evaluated by using the same reasoning as in section 1.1: in fact, since there is only one sinusoid, the indices of the amplitudes and phases appearing in Eq.(A.19) can only assume the values $\pm l$ where l is an integer, implying that $q/2$ indices should be equal to l and the other $q/2$ equal to $-l$. The number of choices to achieve that is obviously given by the binomial coefficient $\binom{q}{q/2}$, hence:

$$\frac{1}{\pi}\int_0^{\pi} cos^q(t)\,dt = \binom{q}{q/2}\frac{1}{2^q} \qquad \text{where} \quad q = 0,2,4,6,\ldots \qquad (C.5)$$

Eq.$(C.5)$ may as well be simply obtained by replacing the amplitude of the sinusoid A with the value 1 in Eq.(1.1.16). Hence, Eq.(C.4) becomes:

$$J_0(A\omega) = \sum_{q\ even}\frac{(-j\omega A)^q}{q!}\binom{q}{q/2}\frac{1}{2^q} = \sum_{q\ even}\frac{(-j\omega A)^q}{\left((q/2)!\right)^2 2^q} =$$

$$= \sum_{q\ even}\frac{\left(-\frac{(\omega A)^2}{4}\right)^{q/2}}{\left((q/2)!\right)^2} \qquad (C.6)$$

Eq.(C.6) coincides with Eq.(C.1), thus Eqs.(C.2-C.3) are equivalent to Eq.(C.1). Therefore, returning to the computation of $p(x)$:

$$p(x) = \frac{1}{2\pi}\int_{-\infty}^{+\infty}\sum_{q\ even}\frac{\left(-\frac{\omega^2 A^2}{4}\right)^{\frac{q}{2}}}{\left(\left(\frac{q}{2}\right)!\right)^2}e^{j\omega x}d\omega =$$

$$= \frac{1}{2\pi}\int_{-\infty}^{+\infty}\int_{-A}^{A}\frac{1}{\pi}\frac{e^{-j\omega t}}{\sqrt{A^2 - t^2}}dt\,e^{j\omega x}d\omega =$$

$$= \frac{1}{2\pi}\int_{-A}^{+A}\left(\int_{-\infty}^{\infty} e^{j\omega(x-t)}\,d\omega\right)\frac{1}{\pi}\frac{1}{\sqrt{A^2 - t^2}}dt$$

As is well known, the integral $\int_{-\infty}^{\infty} e^{j\omega(x-t)}\,d\omega$ is proportional to the Dirac delta function $\delta(x-t)$. More specifically:

$$\int_{-\infty}^{\infty} e^{j\omega(x-t)}\, d\omega = 2\pi\delta(x-t) \qquad (C.7)$$

Therefore:

$$\frac{1}{2\pi}\int_{-A}^{+A}\left(\int_{-\infty}^{\infty} e^{j\omega(x-t)}\, d\omega\right)\frac{1}{\pi}\frac{1}{\sqrt{A^2-t^2}}dt =$$

$$= \frac{1}{2\pi}\int_{-A}^{+A} 2\pi\delta(x-t)\frac{1}{\pi}\frac{1}{\sqrt{A^2-t^2}}dt =$$

$$= \int_{-A}^{+A}\delta(x-t)\, dt\,\frac{1}{\pi}\frac{1}{\sqrt{A^2-x^2}} = \begin{cases}\frac{1}{\pi}\frac{1}{\sqrt{A^2-x^2}} & if\ x\in\,]-A,A[\\ 0 & otherwise\end{cases}$$

The final expression for the probability density function $p(x)$ is:

$$p(x) = \begin{cases}\frac{1}{\pi}\frac{1}{\sqrt{A^2-x^2}} & if\ x\in\,]-A,A[\\ 0 & otherwise\end{cases} \qquad (C.8)$$

which is the correct result for a sinusoid.

Appendix D: proof of Eqs.(1.33,1.35)

The Formulae for kurtosis and variance of a time-series that is considered to be composed of n blocks can be written in the following forms:

$$k_{tot} = \frac{\sum_{j=1}^{n} k_j \cdot T_j \cdot {\sigma_j}^4}{T \cdot {\sigma_{tot}}^4} \qquad (D.1)$$

$${\sigma_{tot}}^2 = \frac{\sum_{j=1}^{n} T_j \cdot {\sigma_j}^2}{T} \qquad (D.2)$$

These formulae are a generalization of Eqs.(1.33, 1.35); in that case the blocks had the same duration. The proof of Eqs.$(D.1, D.2)$ is given next.

Proof:
Without loss of generality, the assumption is made that a discrete signal x_j has zero mean. From the definition of the s^{th} statistical moment $M_{s_{tot}}$ of the signal x_j:

$$M_{s_{tot}} = \frac{\sum_{j=1}^{N_{tot}} {x_j}^s}{N_{tot}}$$

Eq.$(D.1)$ can be derived from the following equalities:

$$M_{4_{tot}} = \frac{\sum_{j=1}^{N_{tot}} {x_j}^4}{N_{tot}} = \frac{\sum_{s=1}^{n} \sum_{j=N_{s-1}+1}^{N_{s-1}+n_s} {x_j}^4}{N_{tot}} = \sum_{s=1}^{n} \frac{n_s}{N_{tot}} \sum_{j=N_{s-1}+1}^{N_{s-1}+n_s} \frac{{x_j}^4}{n_s} = \sum_{s=1}^{n} \frac{T_s}{T} \left(\sum_{j=N_{s-1}+1}^{N_{s-1}+n_s} \frac{{x_j}^4}{n_s} \right) =$$

$$= \sum_{s=1}^{n} \frac{T_s}{T} M_{4_s}$$

In the last step, M_{4_s} represents the 4^{th} statistical moment of the s^{th} block. By substituting the definition for kurtosis:

$$\begin{cases} M_{4_s} = k_s \cdot {\sigma_s}^4 \\ M_{4_{tot}} = k_{tot} \cdot {\sigma_{tot}}^4 \end{cases}$$

Eq.$(D.1)$ is found.
Similarly, Eq.$(D.2)$ can be derived in the following way:

$$M_{2_{tot}} = \frac{\sum_{j=1}^{N_{tot}} {x_j}^2}{N_{tot}} = \frac{\sum_{s=1}^{n} \sum_{j=N_{s-1}+1}^{N_{s-1}+n_s} {x_j}^2}{N_{tot}} = \sum_{s=1}^{n} \frac{n_s}{N_{tot}} \sum_{j=N_{s-1}+1}^{N_{s-1}+n_s} \frac{{x_j}^2}{n_s} = \sum_{k=1}^{n} \frac{T_s}{T} \left(\sum_{j=N_{s-1}+1}^{N_{s-1}+n_s} \frac{{x_j}^2}{n_s} \right) =$$

$$= \sum_{s=1}^{n} \frac{T_s}{T} M_{2_s}$$

By substituting the definition for the second order moments:

$$\begin{cases} M_{2_s} = {\sigma_s}^2 \\ M_{2_{tot}} = {\sigma_{tot}}^2 \end{cases}$$

Eq.$(D.2)$ is found.

Appendix E: equivalence of Eqs.(2.1, 2.11)

This appendix serves to show how one can formally prove the equivalence between Eq.(2.1) and Eq.(2.11). Uppercase letters will be used to indicate *RV*s (e.g. T_1, T_2), whereas lowercase ones to refer to some specific values they assume (e.g. t_1, t_2).
Eqs. (2.1, 2.11) are rewritten in the following, only for the sake of convenience:

$$D(f_n) = \frac{N_p T K^b}{C} \int_0^{+\infty} \Delta z^b \; f_{\Delta Z}(\Delta z) d\Delta z \qquad (E.1)$$

$$D(f_n) = \frac{N_p T K^b}{C} \int_{-\infty}^{\infty} \int_{-\infty}^{\infty} (z(t_2) - z(t_1))^b \; f_{T_1 T_2}(t_1, t_2)\, dt_1 dt_2 \qquad (E.2)$$

In Eq.(E.2), the function $p(t_1, t_2)$ of Eq.(2.11) is rewritten as $f_{T_1 T_2}(t_1, t_2)$ just to make it clear that it represents the joint probability density of the *RV*s T_1, T_2.
It is worth mentioning that the function $f_{T_1 T_2}$ has to comply with some constraints. In particular, a simple property of the function $f_{T_1 T_2}(t_1, t_2)$ is such that $f_{T_1 T_2}(t_1, t_2) = 0$ when $t_1 > t_2$. This property holds because a valley always occurs at an earlier time than its corresponding peak by definition. Besides, the function $f_{T_1 T_2}(t_1, t_2)$ should be equal to 0 also when $z(t_1) > z(t_2)$, because a valley should never exceed the value of its corresponding peak.
It is convenient to define the following two new *RV*s:

$$Z_v = z(T_1) \qquad (E.3)$$

$$Z_p = z(T_2) \qquad (E.4)$$

In Eqs.(E.3, E.4), Z_v, Z_p are the *RV*s corresponding to the relative displacement valleys and peaks. According to these two equations, the joint probability density of the variables T_1 and T_2 can be written in terms of the joint probability density of Z_p, Z_v [33]:

$$f_{T_1 T_2}(t_1, t_2) = \left|\frac{\partial(z_p, z_v)}{\partial(t_1, t_2)}\right| \; f_{Z_p Z_v}(z(t_2), z(t_1)) \qquad (E.5)$$

where $\left|\frac{\partial(z_p, z_v)}{\partial(t_1, t_2)}\right|$ is the absolute value of the Jacobian of the transformation which maps the variables T_1, T_2 into Z_v, Z_p. Eqs.(E.3-E.5) lead to:

$$f_{T_1 T_2}(t_1, t_2) = \left|\frac{d}{dt_2}(z(t_2)) \frac{d}{dt_1}(z(t_1))\right| \; f_{Z_p Z_v}(z(t_2), z(t_1)) \qquad (E.6)$$

If Eq.(E.6) is substituted into Eq.(E.2), one obtains:

$$D(f_n) = \frac{N_p T K^b}{C} \int_{-\infty}^{\infty} \int_{-\infty}^{\infty} (z(t_2) - z(t_1))^b \quad f_{T_1 T_2}(t_1, t_2)\, dt_1 dt_2 =$$
$$= \frac{N_p T K^b}{C} \int_{-\infty}^{\infty} \int_{-\infty}^{\infty} (z(t_2) - z(t_1))^b \quad f_{Z_p Z_v}(z(t_2), z(t_1)) \, |dz(t_2) dz(t_1)| =$$
$$= \frac{N_p T K^b}{C} \int_{-\infty}^{\infty} \int_{-\infty}^{\infty} (z_p - z_v)^b \quad f_{Z_p Z_v}(z_p, z_v)\, dz_p dz_v \qquad (E.7)$$

If the substitution $z_p = z_v + \Delta z$ is made[22] in one of the two integrals contained in Eq.(E.7), one obtains:

$$D(f_n) = \frac{N_p T K^b}{C} \int_{-\infty}^{\infty} \int_{-\infty}^{\infty} \Delta z^b \quad f_{Z_p Z_v}(z_v + \Delta z, z_v)\, d\Delta z dz_v \qquad (E.8)$$

Eq.(E.8) may be rewritten more conveniently as:

$$D(f_n) = \frac{N_p T K^b}{C} \int_{-\infty}^{\infty} \Delta z^b \left(\int_{-\infty}^{\infty} f_{Z_p Z_v}(z_v + \Delta z, z_v)\, dz_v \right) d\Delta z \qquad (E.9)$$

The term contained in the parentheses of Eq.(E.9) has the following three properties:

1) it is a function of Δz;

2) it is positive for any Δz;

3) integrates to 1 over all possible values of Δz, that is:

$$\int_{-\infty}^{\infty} \left(\int_{-\infty}^{\infty} f_{Z_p Z_v}(z_v + \Delta z, z_v)\, dz_v \right) d\Delta z = 1 \qquad (E.10)$$

The second and third property hold because the function $f_{Z_p Z_v}$ is a joint probability density. These properties imply that the distribution $f_{\Delta Z}$ of Δz may be defined as:

$$f_{\Delta Z}(\Delta z) = \int_{-\infty}^{\infty} f_{Z_p Z_v}(x + \Delta z, x)\, dx \qquad (E.11)$$

Eqs.(E.9, E.11) lead to:

$$D(f_n) = \frac{N_p T K^b}{C} \int_{-\infty}^{+\infty} \Delta z^b \; f_{\Delta Z}(\Delta z) d\Delta z \qquad (E.12)$$

It should be noted that the region of integration extends over all $\mathbb{R}$ in Eq.(E.12), whereas it extends over $\mathbb{R}^+$ in Eq.(E.1). However, because $f_{T_1 T_2}(t_1, t_2)$ is zero when $t_1 > t_2$, from Eq.(E.6) it is clear that $f_{Z_p Z_v}(z_p, z_v)$ is zero when $z_v > z_p$, and therefore Eq.(E.11) implies that $f_{\Delta Z}(\Delta z)$ is zero when $\Delta z < 0$. Eq.(E.12) and these considerations prove that Eq.(E.1) is equivalent to Eq.(E.2).

[22] In the substitution $z_p = z_v + \Delta z$, z_v should be considered fixed, because z_p and z_v are independent. Therefore, the differential dz_p is equal to dΔz, and the new set of independent variables becomes z_v and Δz.

Appendix F: novel method for the calculation of the *FDS*

In those applications where it is necessary to assess whether a component can withstand variable loads throughout its expected lifetime, the fatigue damage must be evaluated. The latter is usually estimated by means of the *FDS* spectral function. The *DUT* is identified with *SDOF* systems, independently excited and characterized by different natural frequencies f_n and same damping coefficient ζ. According to the time-domain approach, a representative sample of the load measured from the application (i.e. reference signal) is considered an excitation applied to each *SDOF* system; then, each *SDOF* system generates a response that can be computed in terms of relative displacement. Subsequently, each relative displacement is: (i) analyzed in the time domain in order to extract the peaks and valleys and (ii) the resulting peaks and valleys are employed to compute the amplitudes and number of cycles to estimate the damage. The alternative to this time-domain methodology is the standard frequency domain-approach [44,45], which estimates the damage in terms of a *PSD* with the assumption that the distribution of the reference signal is stationary and Gaussian.
The latter is faster than the time-domain approach computational-wise, because the time-series may be worth of millions of points, whereas the *PSD* is usually composed of hundreds of them.
In order to exploit the advantages of the spectral-domain methods, several authors [46-49] directed their efforts towards extending the latter to non-Gaussian loads, which are more frequent in practical applications.
F. Cianetti et al. [46] empirically proposed useful correction coefficients to evaluate the damage caused by a non-Gaussian signal. These coefficients are given both for stationary and non-stationary applications and depend on the skewness and kurtosis of the system's output.
The range of applicability of these coefficients depends on the values of kurtosis and skewness, as well as the "degree" of non-stationarity [55] of the signals considered. In general, in assessing the damage at different natural frequencies in the time-domain, the response (expressed in terms of relative displacement) changes its distribution. Hence, these parameters could be affected by the natural frequency of the *SDOF* system as well. Besides, the computational time required by the calculation of kurtosis and skewness of the system's output is not negligible.
As far as both time and frequency domain methods are concerned, other important factors to keep into consideration are the assumptions of: linear accumulation of the damage [56], linear proportionality between stress and relative displacement and the linearity of the system. The linearity assumption is considered a staple throughout this work and will not be abandoned; however, one should be aware that non-linearities may play an important role in applications and possibly affect the results if disregarded.
The aim of this appendix is to bridge the gap between time-domain and frequency-domain approaches in the computation of the *FDS*, by moving towards the advantageous computational speed of the frequency-domain approach, still using a time-domain approach; the latter has the advantage of being more reliable and boasts a greater range of applicability.
A novel methodology in the time-domain is proposed in the following; then, some numerical results are shown in terms of precision and speed.

As described in chapter 2, the calculation of the *FDS* in the time-domain starts from the computation of the relative displacement response of the first *SDOF* system. To this end, a fast and accurate ramp-invariant filtering technique is usually adopted [39,50], whose output is indeed the relative displacement signal computed at the *SDOF* system's natural frequency. Then, the peaks and valleys

(i.e. extrema) are extracted from the relative displacement, which are then input to a time-counting algorithm (usually the Rainflow counting) in order to find the amplitudes and number of damaging cycles.
This procedure is then looped through all the *SDOF* systems' natural frequencies.
A methodology that avoids the extraction of the peaks and valleys and the subsequent time-counting technique is introduced next. As it will be motivated both by theoretical and numerical inquiries, the methodology does not affect the precision of the damage estimation sensibly.
Let the *RV*s Z_p, Z_v represent the relative displacement peak and corresponding valley respectively, which are related to the (peak-to-peak) amplitude ΔZ by means of the following equation:

$$\Delta Z = Z_p - Z_v \tag{F.1}$$

The peaks and valleys are counted from the *SDOF* system's response to a reference signal and their stochasticity depends on the randomness of the reference signal.
In the following, uppercase letters will be used to indicate *RV*s (e.g. Z_p), whereas lowercase ones to refer to some specific values they assume (e.g. z_p).
The probability density $f_{\Delta Z}(\Delta z)$ of ΔZ can be related to the joint probability density $f_{Z_p\, Z_v}(z_p, z_v)$. To that end, let A be an auxiliary *RV* defined as:

$$A = Z_p + Z_v \tag{F.2}$$

Then, according to Eqs.(F.1, F.2), the joint probability density of the variables A and ΔZ can be written in terms of the joint probability density of Z_p, Z_v [33]:

$$f_{\Delta Z\, A}(\Delta z, a) = \left|\frac{\partial(z_p, z_v)}{\partial(\Delta z, A)}\right| f_{Z_p\, Z_v}\left(z_p(\Delta z, a), z_v(\Delta z, a)\right) \tag{F.3}$$

where $\left|\frac{\partial(z_p, z_v)}{\partial(\Delta z, A)}\right|$ is the absolute value of the Jacobian of the linear transformation which maps the variables Z_p, Z_v into ΔZ and A. Eqs.(F.1-F.3) lead to:

$$f_{\Delta Z\, A}(\Delta z, a) = \frac{1}{2} f_{Z_p\, Z_v}\left(z_p(\Delta z, a), z_v(\Delta z, a)\right) \tag{F.4}$$

Hence, $f_{\Delta Z}(\Delta z)$ is obtained as a marginal density from $f_{\Delta Z\, A}(\Delta z, a)$:

$$f_{\Delta Z}(\Delta z) = \int_{-\infty}^{+\infty} f_{\Delta Z\, A}(\Delta z, a) da = \frac{1}{2}\int_{-\infty}^{+\infty} f_{Z_p\, Z_v}\left(z_p(\Delta z, a), z_v(\Delta z, a)\right) da \tag{F.5}$$

Eq.(F.5) may then be rewritten as:

$$f_{\Delta Z}(\Delta z) = \frac{1}{2}\int_{-\infty}^{+\infty} f_{Z_p\, Z_v}\left(\frac{a+\Delta z}{2}, \frac{a-\Delta z}{2}\right) da \tag{F.6}$$

By setting $z_p = \frac{a+\Delta z}{2}$, from Eq.(F.6) one obtains:

$$f_{\Delta Z}(\Delta z) = \int_{-\infty}^{+\infty} f_{Z_p\, Z_v}(z_p, z_p - \Delta z) dz_p \tag{F.7}$$

By the definition of conditional probability [33, 57-61], Eq.(F.7) can also be written in the following form:

$$f_{\Delta Z}(\Delta z) = \int_{-\infty}^{+\infty} f_{Z_p|Z_v}(z_p|z_p - \Delta z)\, f_{Z_v}(z_p - \Delta z) dz_p \tag{F.8}$$

where $f_{Z_{p|Z_v}}(z_p|z_v)$ indicates the conditional probability density that the *RV* Z_p takes the value z_p given the variable Z_v assumes the value z_v.
Alternatively, an equally valid form is still obtained using conditional probabilities:

$$f_{\Delta Z}(\Delta z) = \int_{-\infty}^{+\infty} f_{Z_v|Z_p}(z_p - \Delta z|z_p)\, f_{Z_p}(z_p) dz_p \qquad (F.9)$$

Eqs.(F.8,F.9) serve to show the relations between the probability densities given by: $f_{\Delta Z}, f_{Z_p}, f_{Z_v}$.
According to some preliminary numerical results, the integral in Eq.(2.1), which is used to evaluate the *FDS,* yielded satisfactory results if it was approximated as in the following expression:

$$\int_0^{+\infty} \Delta z^b \; f_{\Delta Z}(\Delta z) d\Delta z \approx \int_0^{+\infty} {z_p}^b \; f_{Z_p}(z_p) dz_p \qquad (F.10)$$

From the assumption of ergodicity, one could also write:

$$\int_0^{+\infty} {z_p}^b \; f_{Z_p}(z_p) dz_p = \frac{1}{N_p} \sum_{j=1}^{N_p} z_p[j]^b \qquad (F.11)$$

where $z_p[\cdot]$ is the discrete signal containing the peaks (all supposed to be positive for simplicity) obtained by time-domain counting methods. The possibility of replacing the integral in Eq.(2.1) by the sum on the right-hand side of Eq.(F.11) allows bypassing the step at which the amplitudes Δz are computed via a counting method, starting from the peaks z_p and valleys z_v obtained from the time history. Another obvious advantage is that only the peaks are required, not the valleys.
As a step further, in order to avoid searching for the peaks by using ad-hoc functions that store the peaks and troughs in floating-point vectors, an alternative faster and precise method is now explained, which allows finding the peaks using vectors of binary numbers, more sparing in terms of memory allocations.
Without knowing precisely where the peaks are located, only the maximum value z_{max} of the signal is extracted from the *SDOF* system's output $z[\cdot]$ (i.e. the signal that contains the peaks $z_p[\cdot]$ and $z_v[\cdot]$ and other points in between). All the other peaks are contained between this upper value and another lower value, considered a percentage p of the maximum value of the signal; its choice will be empirical and shown in the results. It is assumed (and later motivated) that only the values of the time-series $z[\cdot]$ contained in the range $[\, p \cdot z_{max}, z_{max}]$ contribute to the damage; therefore the summations will be performed only over those values. Obviously, the parameter $p \cdot z_{max}$ should be set to low enough values in order that all the relevant peaks be included in the computations, but also as high as possible in order to reduce the number of computations.
The points of the time-series $z[\cdot]$ included in the interval: $[\, p \cdot z_{max}, z_{max}]$ are assumed to contain all the peaks $z_p[\cdot]$ and, in the neighborhood of each peak, it is assumed that the non-negligible terms $(z_p[j]^b)$ are symmetric with respect to the peak, with the latter being the maximum value in that neighborhood. Therefore, according to this hypothesis, the non-negligible terms start from a lower value, increase till the maximum, then decrease till the same lower value is reached; the number of points contained between the lower value and the peak where the signal $z[\cdot]$ is increasing is denoted by the number N_z. N_z is considered to be independent from the peak considered and another simplifying assumption is the following: the $z[\cdot]$ values in the neighborhood of the j^{th} peak $z_p[j]$ differ by integer multiples of Δ_j (i.e. the signal grows linearly[23] in the left neighborhood of the peak

[23] Because Δ_j does not depend on the index k, the signal is assumed to behave linearly in the neighborhood of the peak. This assumption is convenient for the sake of simplicity, but the subsequent considerations can be extended to the more general case where Δ_j also depends on k.

and then decreases symmetrically). Δ_j is to be considered "small" with respect to N_z and the product $N_z\Delta_j$ is negligible with respect to the peaks z_p.

To summarize, the complete set of assumptions is the following:

1) Only the values of $z[\cdot]$ contained in the range $[\,p \cdot z_{max}, z_{max}]$ will appear in the summations of terms of the kind: $z[j]^b$, assumed to be positive and related to the damage.
2) Around each peak z_p contained in the interval $[\,p \cdot z_{max}, z_{max}]$, there are $2N_z$ values symmetrically distributed between the peak's left (where the signal $z[\cdot]$ increases till it reaches the peak) and right (where the signal $z[\cdot]$ decreases symmetrically with respect to the increasing part).
3) The N_z values of $z[\cdot]$ in the left neighborhood of the j^{th} peak $z_p[j]$ differ by integer multiples of Δ_j.
4) The sampling frequency is high enough for the signal $z[j]$ to be considered continuous (i.e. N_z is "large" and Δ_j is "small"). The product $N_z\Delta_j$ can be finite but considered negligible with respect to the peaks z_p.

A graphical representation of the assumptions is shown in Fig.F.1, where the points of the *SDOF* system output $z[\cdot]$ above the threshold value $p \cdot z_{max}$, on the left of the peaks $z_p[j]$ and $z_p[j+1]$, are plotted to emphasize their comparison. Both the points close to $z_p[j]$ and the points close to $z_p[j+1]$ amount to the same number of points N_z (for sake of visual simplicity N_z was set equal to 5). According to the assumptions, those points lie on two lines whose slope is proportional to Δ_j and Δ_{j+1}.

Under assumptions 1, 2 and 3, the summations performed which are related to the damage are the following:

$$\gamma = \sum_{k=0}^{N_z} \sum_{j=1}^{N_p} \left(z_p[j] - k\Delta_j\right)^b \qquad (F.12)$$

In order to motivate it, according to assumption 4, the summation over index k may be replaced by an integral:

$$\gamma \approx \int_0^{N_z} \sum_{j=1}^{N_p} \left(z_p[j] - \xi\Delta_j\right)^b d\xi \qquad (F.13)$$

Eq.(F.13) yields:

$$\gamma \approx \sum_{j=1}^{N_p} \frac{z_p[j]^{b+1} - \left(z_p[j] - N_z\Delta_j\right)^{b+1}}{\Delta_j(b+1)} \qquad (F.14)$$

Since $N_z\Delta_j$ is small compared to $z_p[j]$, a Taylor series expansion of the numerator truncated after two terms gives:

$$\gamma \approx N_z \sum_{j=1}^{N_p} \left(z_p[j]^b - b z_p[j]^{b-1} \frac{N_z\Delta_j}{2}\right) \qquad (F.15)$$

By assuming: $z_p[j] \gg b\frac{N_z\Delta_j}{2}$ ($N_z\Delta_j$ is small with respect to $z_p[j]$), one obtains:

$$\gamma \approx N_z \sum_{j=1}^{N_p} z_p[j]^b \qquad (F.16)$$

After denominating by N the total number of points of the system's output $z[\cdot]$ and defining the parameter $h[f_n]$ as in the following expression:

$$h[f_n] \stackrel{\text{def}}{=} \frac{N}{N_z N_p} \qquad (F.17)$$

Eq.(F.16) can be rewritten as:

$$\frac{1}{N_p} \sum_{j=1}^{N_p} z_p[j]^b \approx \frac{1}{N} h[f_n] \gamma \qquad (F.18)$$

It must be highlighted that $h[f_n]$ is a function "reasonably" independent of the particular time-series $z[\cdot]$. In fact, N_z is related to the density of points around any peak, which is assumed to be constant; this is strictly true if the signal $z[\cdot]$ reaches any peak $z_p[j]$ from the value $p \cdot z_{max}$ in a fixed amount of time equal to N_z/F_s. In Eq.(F.17) the ratio N_p/N is also "reasonably" independent of the time-series $z[\cdot]$, because the larger the number of points N of the time-series, the proportionally larger N_p. Rather, $h[f_n]$ depends on the natural frequency of the *SDOF* system, since that affects the parameter N_p: in fact, as f_n increases, it is intuitive to hypothesize that the number of peaks N_p will increase as well. This would lead $h[f_n]$ to have a tendency to decrease with f_n. A more detailed motivation will be given in the last part of this appendix dedicated to simulation results; in fact, the validity of the assumptions altogether can only be inferred from simulation results.
Instead of using the definition of Eq.(F.17), $h[f_n]$ will be computed numerically only one time, by taking advantage of its independence from the time-series.
The integral in Eq.(2.1) can finally be written as:

$$\int_0^{+\infty} \Delta z^b \; f_{\Delta Z}(\Delta z) d\Delta z \approx \frac{1}{N} h[f_n] \, \gamma \qquad (F.19)$$

Hence, the approximated value of the Fatigue Damage $\mathrm{D_a}[f_n]$ can be computed as in the following:

$$D_a[f_n] = \frac{K^b}{C} n_p \, h[f_n] \frac{T}{N} \sum_{k=0}^{N_z} \sum_{j=1}^{N_p} \left(z_p[j] - k\Delta_j \right)^b \qquad (F.20)$$

Knowing that the sampling frequency F_s is equal to $N \cdot T^{-1}$, the expression can also be formulated as:

$$D_a[f_n] = \frac{K^b}{C} n_p \, h[f_n] \frac{1}{F_s} \sum_{k=0}^{N_z} \sum_{j=1}^{N_p} \left(z_p[j] - k\Delta_j \right)^b \qquad (F.21)$$

The strategy that will be used to calculate $h[f_n]$ will be the following:

1) After choosing a reference profile, set $h[f_n] = 1$ for every f_n and compute the damage $D_a[f_n]$ as in Eq.(F.21);
2) compute the damage $D[f_n]$ with the "standard" time domain procedure;
3) set $h[f_n] = \frac{D[f_n]}{D_a[f_n]}$ for every f_n.

As already highlighted, $h[f_n]$ should not "strongly" depend on the particular reference profile chosen. Once it is known, it can be used in every other application, with the only (possible) additive step being the interpolation of its values in case the *FDS* of another application had a different number of points from the one used to calculate $h[f_n]$. In any case, the latter operation would not be troublesome since it could be done outside the main loop. The reference profile chosen to calculate $h[f_n]$ should have a sampling frequency high enough to span all the frequencies of interest of any other application.

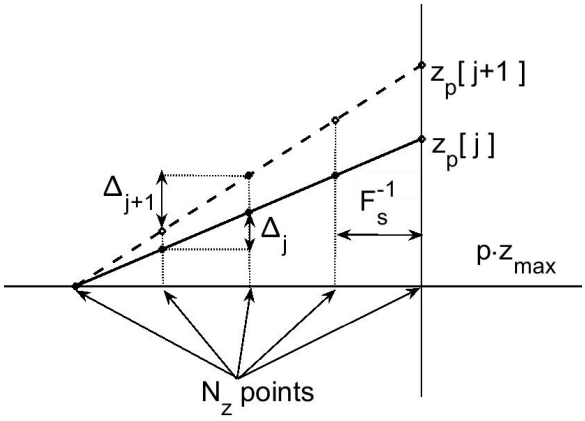

Fig. F.1. Graphical representation of the points of time-series $z[\cdot]$ on the left of peak $z_p[j]$ (continuous line) and $z_p[j+1]$ (dashed line). On the y-axis relative displacements are plotted, whereas on the x-axis one could represent either time or number of points

The theoretical considerations presented in this appendix are now tested. The standard time-domain procedure accepted in the literature will be compared in terms of speed and precision to the proposed method.

The selected platform to do the required computations to display the results is Matlab®. The time counting technique adopted is the Rainflow algorithm, considered as the most reliable [62-64].

The algorithms implemented in the standard procedure are optimized to achieve fast computations in order to make fair comparisons with the novel method. To the author's knowledge, one of the most used Matlab® implementations of the Rainflow algorithm can be found on the Matlab® Central File Exchange [65], which boasts more than 39000 downloads as of October 2020.

Before the comparison, the first step is to compute the function $h[f_n]$, by choosing a reference signal. The starting reference signal, here denoted as ***RS1***, represents field data sampled at 8192 Hz, with a duration of 23.3 seconds. Fig.F.2 shows its plot, whereas some statistical parameters are listed in Table F.1, in particular: standard deviation, kurtosis, crest factor. It can be observed that the reference signal is Leptokurtic, i.e. its kurtosis is greater than 3.0 as numerous peaks and/or bursts are present in the time-series.

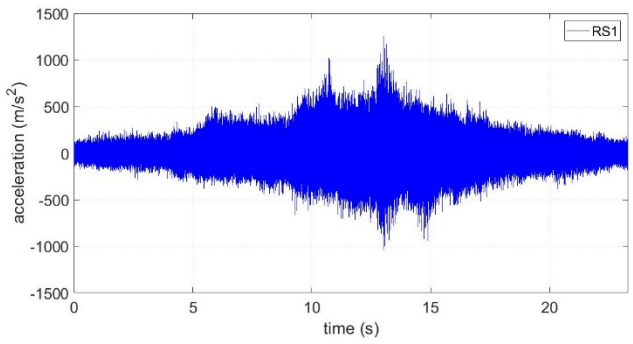

Fig. F.2. Reference signal used for the computation of $h[f_n]$

Table F.1. Statistical parameters of the reference signal ***RS1***

Statistical parameters of the reference signal	***RS1***
RMS $[\boldsymbol{m/s^2}]$	139
Kurtosis [-]	5.73
Crest factor [-]	9.02

In order to perform the computation of Eq.(F.20) (or Eq.(F.21)), the percentage p of the maximum value of the relative displacement time-series $z[\cdot]$ should be set. The choice, after a trial and error procedure, was made to set $p = 400^{-1/b}$. The exponent $-1/b$ is present because the lower b, the less

negligible terms there are in the neighborhood of the peaks (damage is proportional to the values $z_p[j]^b$). Vice versa, the higher the Wohler's curve slope b, the (usually) lower number of points can be used in the computation of the damage via Eq.(F.21), because more of them become negligible with respect to the highest peaks (in absolute value), which are raised to the b^{th} power. The summations in Eq.(F.21) are performed by using the Matlab command: *sum(z(z>p*zmax).^b)*, where z is the output of the *SDOF* system and *zmax* its maximum value. The operation has to be looped through each frequency f_n.

As expounded at the beginning of this appendix, the advantages should be: (i) the time-consuming extraction of the peaks and valleys stored in a floating point vector and the subsequent time-counting are avoided, (ii) the number of points over which the summation is carried out is minimized.

The floating point vector of the standard procedure computed in every loop is replaced by the logical operation *z>p*zmax,* which is a vector containing either zeroes or ones and consequently allows faster computations.

The most important parameters involved in the computation of the damage, b and ζ, are set to the values of 5 and 2.5% respectively. The other parameters, namely the expected lifetime T and the constants C and K, are chosen respectively equal to one in their corresponding units of measurement. C and K are often set to the value of one because usually unknown [40]. Nevertheless, what is essential is not the magnitude of the damage, rather the *relative* difference between the *FDS* of different applications. This led the term "damage" to be usually replaced by "pseudo-damage".

The resolution in the calculation of the *FDS* was set to 4 Hz, with the natural frequencies of the *SDOF* systems ranging from 4 Hz to the Nyquist frequency 4096 Hz.

With the input to the *SDOF* systems being the reference signal ***RS1***, the parameter $h[f_n]$ results as in Fig.F.3. From an inspection of the curve, it has a tendency to decrease when the natural frequency increases, the more so at lower frequencies; this behavior was expected as previously discussed.

The calculation of $h[f_n]$ is used to compute the *FDS* of another reference signal. The latter, here denoted as ***RS2***, represents field data sampled at 8192 Hz, with a duration of 660 seconds. Fig.F.4 contains its plot, whereas some statistical parameters are listed in Table F.2, in particular: standard deviation, kurtosis, crest factor.

The *FDS* of the signal of Fig.F.4 is computed with the following new set of parameters, in order to test the theoretical results in different conditions: b=9, ζ=4%, T=1 h. The *FDS* curves are calculated by both the novel method and the standard procedure (by means of Eqs.(2.10,F.21) respectively as the last step) and are displayed in Fig.F.5. It can be observed that the matching of the curves is precise, and the computational time required by the method proposed in this appendix proved to be more than 13 times faster as shown in Table F.3.

In the case of other profiles the results are similar; it may be worth showing another example.

The starting reference signal, here denoted as ***RS3***, represents field data sampled at 500 Hz, with a duration of 1200 seconds. Fig.F.6 contains its plot, whereas some statistical parameters are listed in Table F.4.

The *FDS* of the signal of Fig.F.6 is computed with the following new set of parameters, in order to test the theoretical results in yet different conditions: b=4.5, ζ=1.5%, T=10 h. The *FDS* curves are calculated by both the novel method and the standard procedure and are displayed in Fig.F.7. It can be observed that the matching of the curves is precise, and the computational time required by the method proposed in this appendix proved to be 12 times faster as shown in Table F.5.

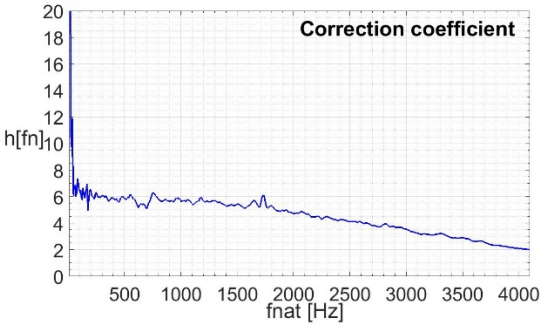

Fig. F.3. $h[f_n]$ calculated by setting: $b = 5$, ζ=2.5%

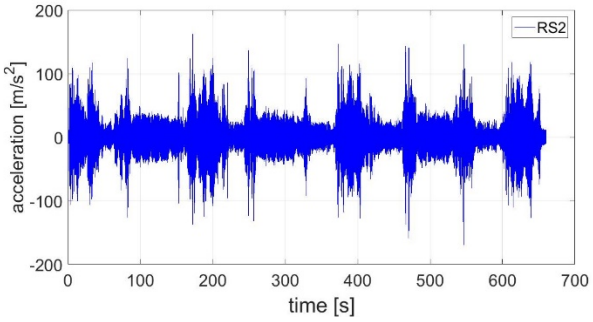

Fig.F.4. Reference signal ***RS2***

Table F.2**.** Statistical parameters of the reference signal ***RS2***

	RMS (ms^{-2})	Kurtosis (-)	Crest factor (-)
Ref.	14.3	7.05	11.9

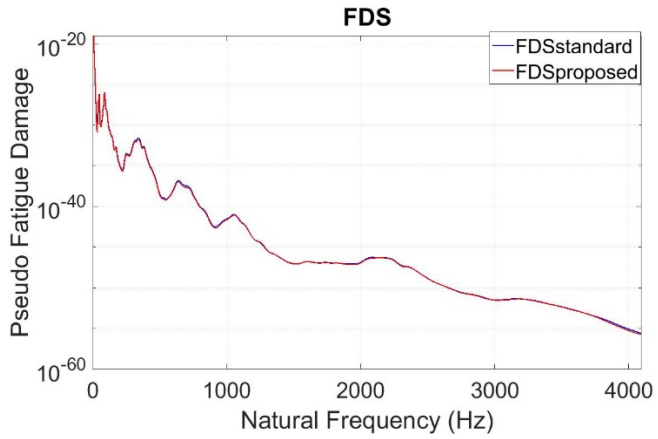

Fig. F.5. *FDS* of the signal ***RS2*** calculated by the two different methods

Table F.3. Computational time required by the two methods to compute the *FDS* of the signal ***RS2.*** ***(****Processor: AMD A6-5200 APU with Radeon (TM) HD graphics 2 GHz)*

Computation Time	[***s***]
Standard method	2093
Proposed method	153

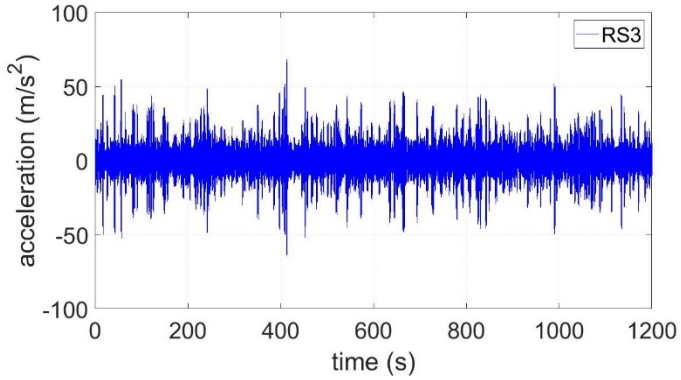

Fig. F.6. Reference signal ***RS3***

Table F.4. Statistical parameters of the reference signal ***RS3***

Statistical parameters of the reference signal	***RS1***
Std deviation $[m/s^2]$	8.42
Kurtosis [-]	6.42
Crest factor [-]	8.12

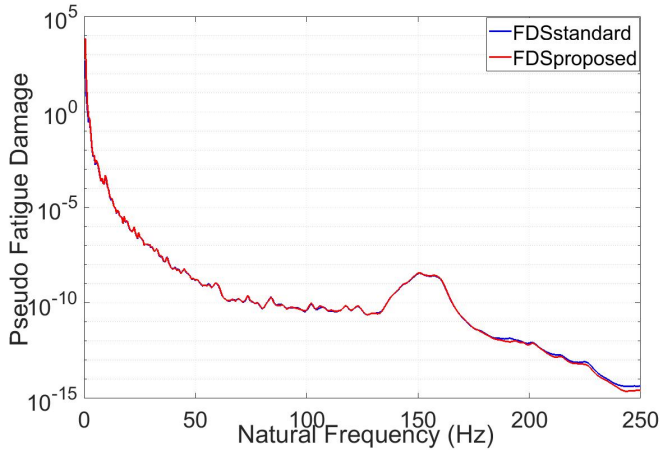

Fig. F.7. *FDS* of the signal ***RS3*** calculated by the two different methods

Table F.5. Computational time required by the two methods to compute the *FDS* of the signal ***RS3*** ***(****Processor: AMD A6-5200 APU with Radeon (TM) HD graphics 2 GHz)*

Computation Time	[***s***]
Standard method	120
Proposed method	10

Appendix G: determination of b

The value of Wohler's curve slope (related to parameter b) was determined by performing random tests with different *RMS* levels and flat *PSD*. As is well known, if N_f is the number of cycles with sinusoidal stress amplitude σ that lead the DUT to failure, Wohler's curve (also known as S-N curve[24] or Basquin's law) has the form:

$$\sigma^b N_f = C \tag{G.1}$$

In case of non-sinusoidal stress histories, stress amplitudes can still be obtained from counting techniques as explained in chapter 2, where it is assumed that each of those amplitudes satisfies Eq.(G.1). If the stresses are lower than the material's yield strength, the relationship between stresses and relative displacements (function $z(t)$ in chapter 2) may be considered linear. The relative displacement $z(t)$ is simply the difference between the system's output $y(t)$ (i.e. response of the *DUT* excited by the shaker's physical motion) and the input $x(t)$ (i.e. physical motion of the shaker), where both $y(t)$ and $x(t)$ are displacements. From Eq.(2.6), if the *SDOF* system has a natural frequency f_n and the (acceleration) signal $\ddot{x}(t)$ has a flat *PSD* denoted by G, it is easy to see that the square of the *RMS* of $z(t)$ is proportional to the *PSD,* that is:

$$z_{rms}(f_n)^2 = L(f_n, \zeta) \cdot G \tag{G.2}$$

In Eq.(G.2) L is simply a proportionality constant which depends on both the frequency and damping coefficient of the system, given by the relationship:

$$L(f_n, \zeta) = \frac{1}{2\pi(2\pi f_n)^3} \int_0^\infty \frac{1}{(h^2-1)^2 + (2\zeta h)^2} dh \tag{G.3}$$

Due to the assumed linearity between stress and relative displacements, the square of the *RMS* of the stress time history is then proportional to the *PSD* G, which, on its part, is proportional to the square of the *RMS* of the input signal $\ddot{x}(t)$ due to the constancy of *G.* Therefore:

$$\sigma_{rms} = const \cdot \ddot{x}_{rms} \tag{G.4}$$

Eq.(G.4) would also hold in the particular case the stress signal is a sinusoid (in this case the *PSD* of the signal would be a Dirac delta function), therefore in principle the stress σ in Eq.(G.1) could be replaced by $\ddot{x}_{rms}$ and the constant C would simply be replaced by a different constant $\tilde{C}$. It is worth mentioning that the "constant" would depend on the natural frequency of the system as it should be evident from Eq.(G.3) (which leads to Eq.(G.4)), therefore it is not actually a constant if f_n is not fixed (as in the case of the *FDS* concept). Nevertheless, the *FDS* of every signal would be affected by the same factor, meaning that the concept of relative damage would still be preserved[25] if, for sake of simplicity, it is assumed that the constant in Eq.(G.4) remains constant regardless of any possible change in f_n. If the signal $\ddot{x}(t)$ were not sinusoidal, by analogy with stresses, Eq.(G.1) could be still considered a relationship satisfied by each of its amplitudes extracted by time-counting methods. Besides, if it is assumed that the number of cycles to failure N_f is proportional to the time to failure (denoted by T) of the *DUT* subjected to the acceleration $\ddot{x}(t)$, Eq.(G.1) may be rewritten as:

[24] This type of curve is widely plotted for many different materials, e.g. [66-68].

[25] In fact, the ratio of *FDS* curves is unaffected by the factor.

$$(\ddot{x}_{rms})^b\, T = \tilde{C} \qquad (G.5)$$

Since the relation between the amplitudes extracted by time-counting methods and the overall *RMS* of the signal $\ddot{x}_{rms}$ is simply linear if other conditions are fixed (such as the shape of the *PSD* is flat and the signal's distribution is Gaussian), then in Eq.(G.5) $\ddot{x}_{rms}$ could simply be considered as the overall *RMS* of the signal. Scaling the *RMS* would simply imply scaling the amplitudes if the distribution is fixed. In fact, if two random signals are generated from a *PSD* (i.e. their distribution is Gaussian) with two different *RMS* levels, their amplitudes will have the same distribution and their values will differ approximately by a factor equal to the ratio of the two different *RMS* values.

The purpose of the tests mentioned at the beginning of this appendix was to determine a value for parameter b through the use of Eq.(G.5). When experimental tests were performed, points with coordinates $(log(T), log(\ddot{x}_{rms}))$ were drawn and, since Wohler's curve is simply a line in log-log scale, the slope of the line was determined according to the Least Squares method.
Considering that the natural frequency of a specimen decreases as damage accumulates, failure was defined to occur at the time T where the tangent to the curve f_n reached a certain (negative) slope. It is worth mentioning that since the curves defining natural frequencies were obtained numerically from real measurements, adequate polynomials were used to interpolate the curves and properly define tangents. This approach was used because of its simple numerical automation. It was made simple by the fact that curves had the same shape in all tests: frequency remained constant (up to small unavoidable numerical fluctuations) until it suddenly started decreasing when close to the point of failure. This regularity pattern did not occur when non-Gaussian tests were performed, as explained in sections 4.3 and 4.4, so the definition of failure was different in that case. However, it should be highlighted, especially in this case where the decrease in frequency is steep, that any reasonable definition of failure should lead to similar results. An example of the curves mentioned above is shown in Fig.G.1: this particular test was performed at 0.4 g on specimen number 3.

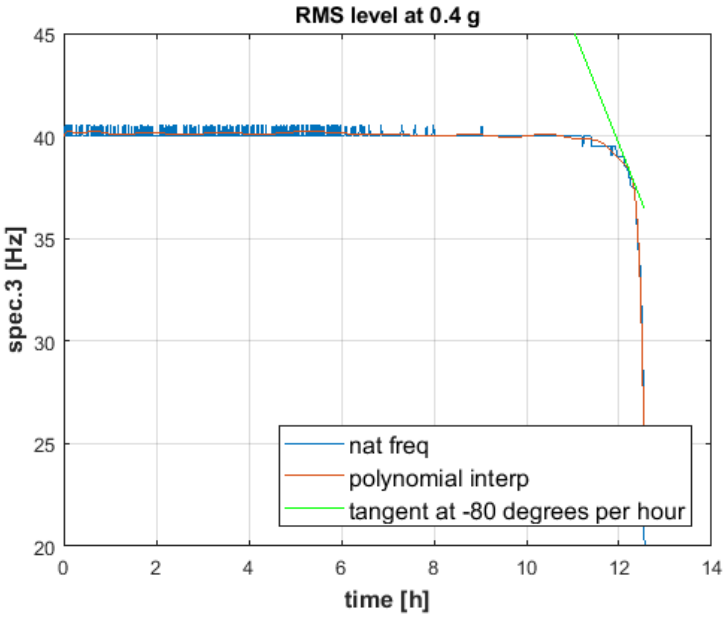

Fig.G.1: test performed at 0.4 g on specimen #3: the blue curve represents the natural frequency computed from the real measurements; the red one is the polynomial interpolation, whereas the green one is the tangent that defines the *TTF*.

The software used for the tests was TestLab, in particular the Random mode module. The flat *PSD* was defined in the interval [20 Hz,48 Hz], and as exemplified by the test performed on the same specimen reported in Fig.F.1, the *RMS* level was controlled precisely, as shown in Fig.G.2a. A 500

points *PSD* is shown in Fig.G.2b; the Nyquist frequency is 400 Hz because Testlab defined the sampling frequency of shaker drive signals to be equal to 800 Hz.

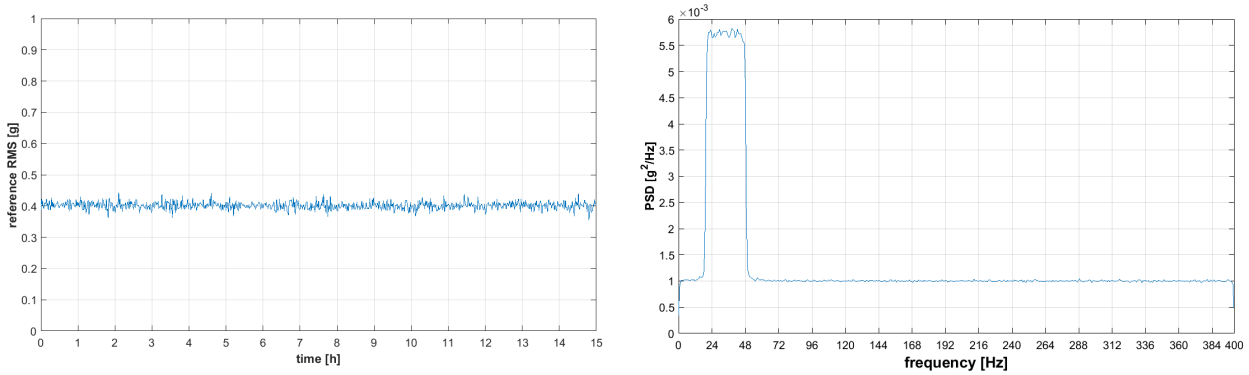

(a) (b)

Fig.G.2: test performed at 0.4 g on specimen #3: the shaker controller is able to follow the a) *RMS* and b) *PSD* specification

The tests were performed at the following levels (expressed in g): 0.3, 0.4, 0.5 and 0.6 and for each level the median *TTF* was taken. Each single test consisted of three specimens and those having the shortest *TTF* values were repeated twice, therefore the median value was extracted either from three or six samples. Both the *RMS* levels and *TTF* values are summarized concisely in the first two rows of Table G.1. Using the Least Squares method, the values of Table G.1 lead to a value of approximately 9.17 for parameter b. In order to gather more information about dispersion of data, the mean, minimum and maximum values for the *TTF*'s are reported in the remaining three rows of Table G.1. Wohler's curve is usually defined as the curve that coincides with 50% probability that the specimen reaches failure at the specific stress level considered on the curve. Therefore, it makes sense to consider the median values for the *TTF*. Nevertheless, in principle one might as well obtain Wohler's curves associated with different probabilities of failure: for instance, the maximum *TTF* values correspond to 100% probability that the specimens fail, etc. The curves that correspond to the: median, mean, minimum, maximum *TTF*'s were obtained via Least Squares as well; they are plotted in Fig.G.3, with their corresponding values of b. Since the values for the parameter b were calculated to be reasonably similar for the different curves (8.89 for maximum *TTF*'s, 9.38 for minimum *TTF*'s, 9.02 for mean *TTF*'s, 9.17 for median *TTF*'s), any choice of the value of b in the range 8.89 and 9.38 would be acceptable. Due to the intrinsic uncertainty of both the model used and the phenomenon studied, the parameter b was chosen to be equal to exactly 9.00 for the sake of simplicity.

Table G.1: median times to failure associated with each individual *RMS* level

RMS levels [g]	0.3	0.4	0.5	0.6
Median TTF [h]	97.0	9.17	0.422	0.396
Mean TTF [h]	87.6	10.7	0.474	0.366
Minimum TTF [h]	53.6	2.87	0.191	0.163
Maximum TTF [h]	112	21.2	0.810	0.538

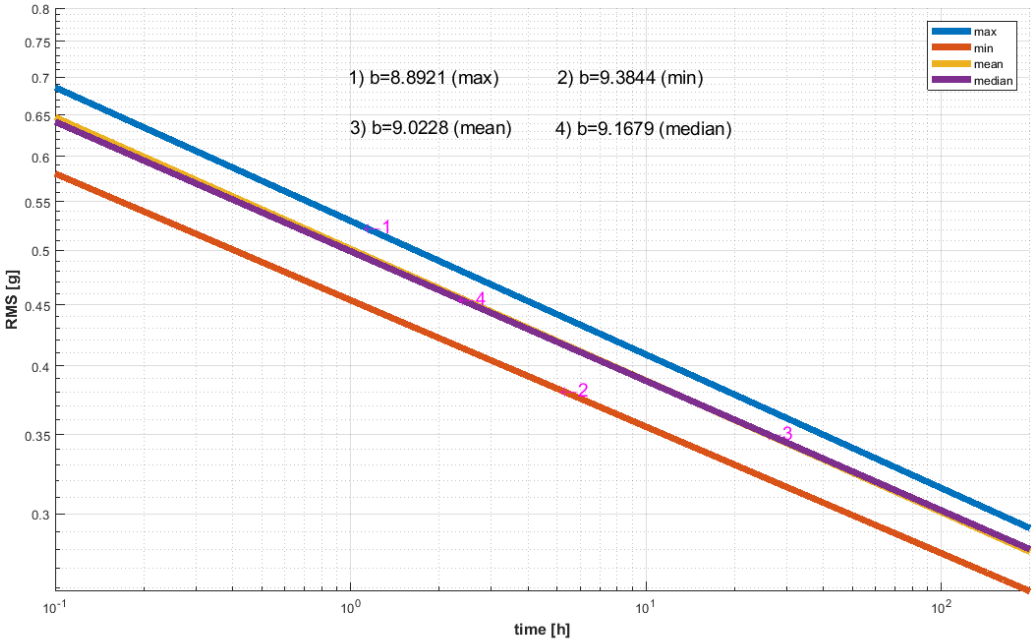

Fig.G.3: Wohler's curves estimated via Least Squares and associated with different probabilities of failure

Appendix H: *GUI* implementing the algorithms

The author's collaboration with industries led to the development of Graphical User Interfaces (*GUI's*) that implement all the novel algorithms proposed, as well as the standard methodologies. This appendix is not intended to serve as a step-by-step manual for the use of these *GUI*'s, since its purpose is only to highlight some of the main auxiliary characteristics – not usually available in standard software – arisen from the collaboration with interested companies. Three independent *GUI's* are shown in Fig.H.1, where the main external buttons outline some basic functionalities. Fig.H.1a shows the front end of the *GUI* related to kurtosis control, Fig.H.1b shows the one related to Standard Mission Synthesis, whereas Fig.H.1.c shows the *GUI* implementing the algorithms presented in section 2.2. Several other functionalities appear in the form of dialogue boxes while running the *GUI's*; among them, it is worth mentioning the possibility of: pre-processing signals by filtering, plotting the time-series and their *PSD's*, dealing with multiple situations[26] (either in parallel or in series), as well as synthesizing multiple time-series at a time.

Aside from the synthesis of signals, one of the most useful features implemented in the *GUI's* is the possibility of inserting specifications and make comparisons with measured data. In fact, in evaluating whether a component may withstand the loads distinctive of a particular application, it might be useful to compare the *FDS* derived from a given specification with the *FDS* computed from representative signals that are measured from the application. The analysis should then be performed on the frequency range of interest for the component: the *FDS* derived from the specification should be higher than the measurement's *FDS*, because specifications outline the domain of proper functioning that manufacturers guarantee. Usually, the specification is derived from both random tests and sweep tests. Therefore, the manufacturer might specify both a *PSD* and the characteristics of a sweep test on the component's catalogue. The *PSD* information should be paired with the important information of the test duration, whereas the most relevant characteristics of the sweep tests are: duration of the test, sweep rate, sweep amplitudes at different time instants. The *PSD* is usually defined in a chart, where the magnitudes at some relevant frequency points are reported; an example is given in Fig.H.2a, whereas Fig.H.2b helps visualize an example of a sweep test specification.

In the *GUI's* front end, by clicking on the "insert specification" button, it is possible to insert all the necessary inputs written on the catalogue. At the end of the procedure, this specification is translated to an *FDS* that can be visualized and compared with the reference signal's *FDS.* Fig.H.3 shows the steps that need to be performed to insert the random specification, whereas Fig.H.4 is analogous but the steps refer to the sweep specification.

The *FDS* derived from the *PSD* specification is computed from the *PSD* according to the frequency domain method, whereas the *FDS* derived from the sweep specification is computed from the sweep signal according to the time domain method. The sweep signal is obtained from the specification; an example is the sweep defined by Fig.H.2b, which is plotted in Fig.H.5.

[26] The phrase "multiple situations" refers to a subdivision of a product's life cycle into multiple dynamic events such as: handling, transport, storage, etc., in which the product is subjected to different vibrations. If different events take place during the life of the product, it is said that the events are in series; sometimes the latter can be in parallel, i.e. only one of them occurs, for example when it is not known whether the product will be transported by air or by sea. In this case, the damage estimation via the *FDS* function consists in measuring representative signals from each situation, compute the *FDS*, then sum the *FDS* curves of events that are in series and/or envelope *FDS* curves of events that are in parallel.

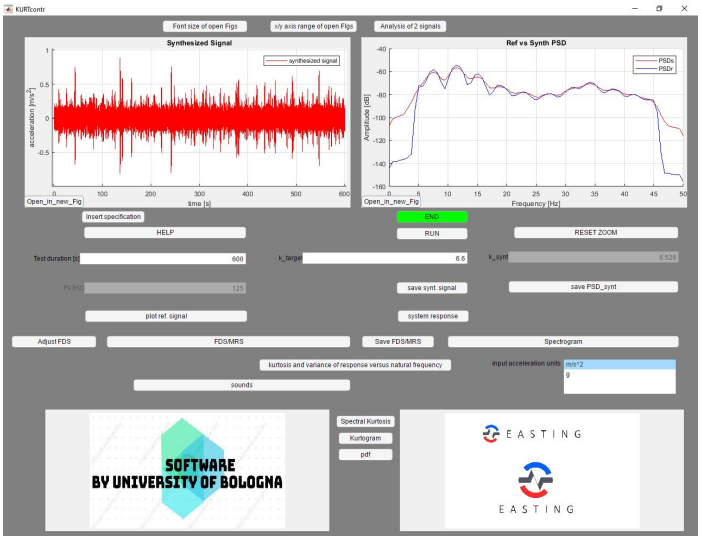

(a)

(b)

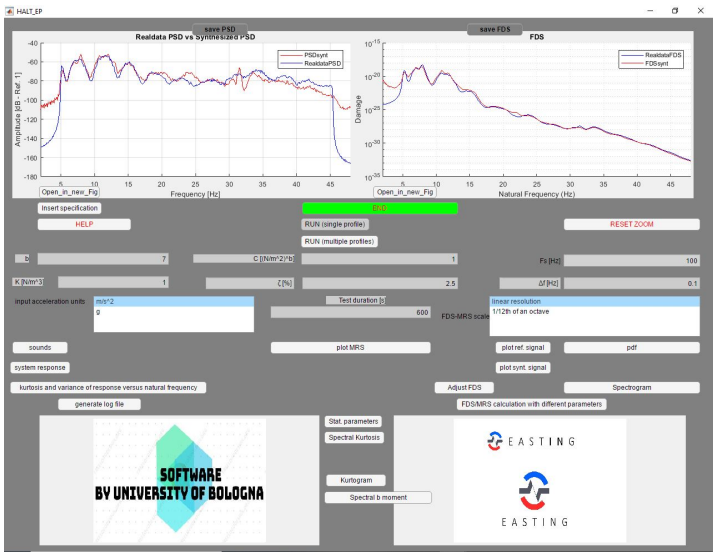

(c)

Fig.H.1: the *GUI's* front ends showing the main buttons: *GUI* related to (a) kurtosis control algorithms, (b) Standard Mission Synthesis, (c) novel algorithms with a priori *FDS* control

Frequenzbereich:	10 Hz bis 2000 Hz
Rauschprofil:	10 Hz -> 14 $(m/s^2)^2/Hz$ 20 Hz -> 28 $(m/s^2)^2/Hz$ 30 Hz -> 28 $(m/s^2)^2/Hz$ 180 Hz -> 0,75 $(m/s^2)^2/Hz$ 300 Hz -> 0,75 $(m/s^2)^2/Hz$ 300 Hz -> 0,51 $(m/s^2)^2/Hz$ 500 Hz -> 20 $(m/s^2)^2/Hz$ 2000 Hz -> 20 $(m/s^2)^2/Hz$
Beschleunigung (RMS):	**177 m/s²**
Anzahl Linien:	400
Degrees of freedom:	192
Crestfaktor:	3
Abschaltgrenzen (rot):	± 6 dB
Beanspruchungsrichtungen:	drei, senkrecht zueinander stehend
Prüfdauer pro Achse:	96 h
Prüfdauer gesamt:	**288 h**

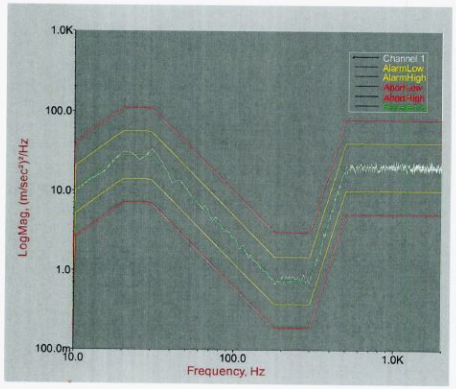

Abbildung 1: Schwingprofil Rauschen

(a)

Anregung:	**sinusförmig**	
Frequenzbereich:	**20 Hz bis 520 Hz** **20 Hz: (a = 11,4 m/s²) (CD)** **65 Hz: a = 120 m/s²** **260 Hz: a = 120 m/s²** **260 Hz: a = 90 m/s²** **350 Hz: a = 90 m/s²** **350 Hz: a = 60 m/s²** **520 Hz: a = 60 m/s²**	
Frequenzdurchlauf:	**0,5 Oktaven pro Minute**	**UP/DOWN**
Anzahl der Frequenzzyklen pro Achse:	zeitabhängig	
Prüfzeit pro Achse:	**96 h**	
Achsen:	drei (X,- Y-, Z-Achse)	
Gesamtprüfzeit:	**288 h**	

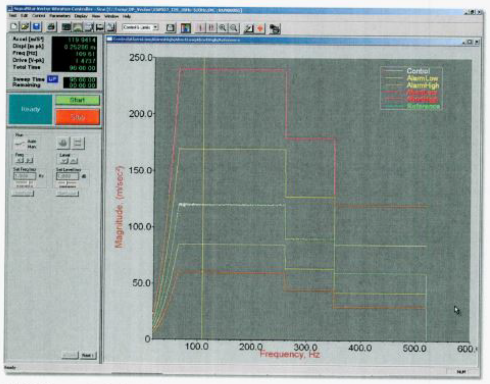

Abbildung 1: Schwingprofil Sinus

(b)

Fig.H.2: (a) random test specification, (b) sweep test specification

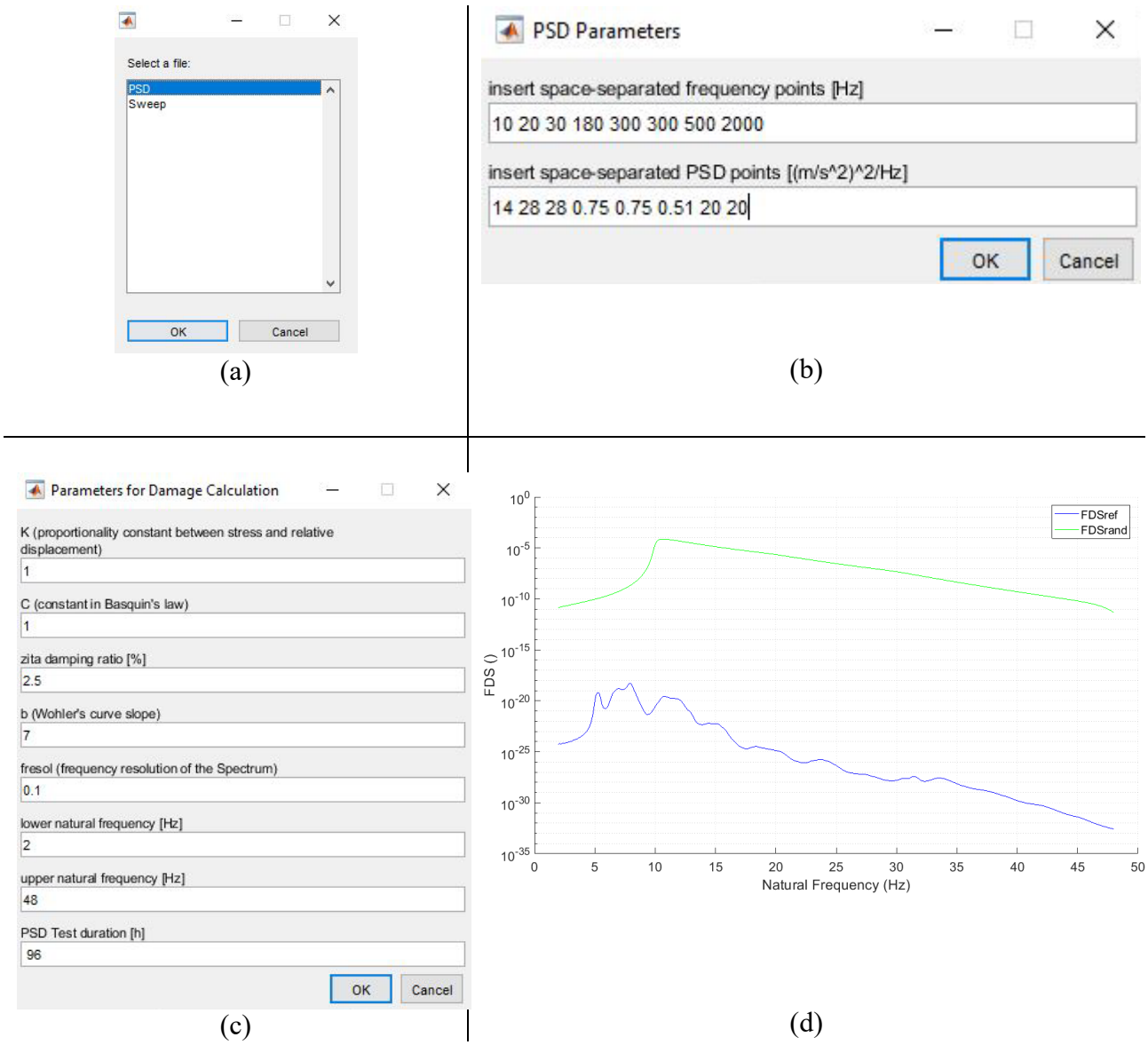

Fig.H.3: after clicking on the "Insert specification" button, the *PSD* specification is selected (a). Then, the *PSD* is input (b) and the parameters that lead to the calculation of the *FDS* are inserted (c). Finally, the *FDS* of the specification is compared with the *FDS* of the reference signal (in this case the comparison is made only in the range 0-50 Hz).

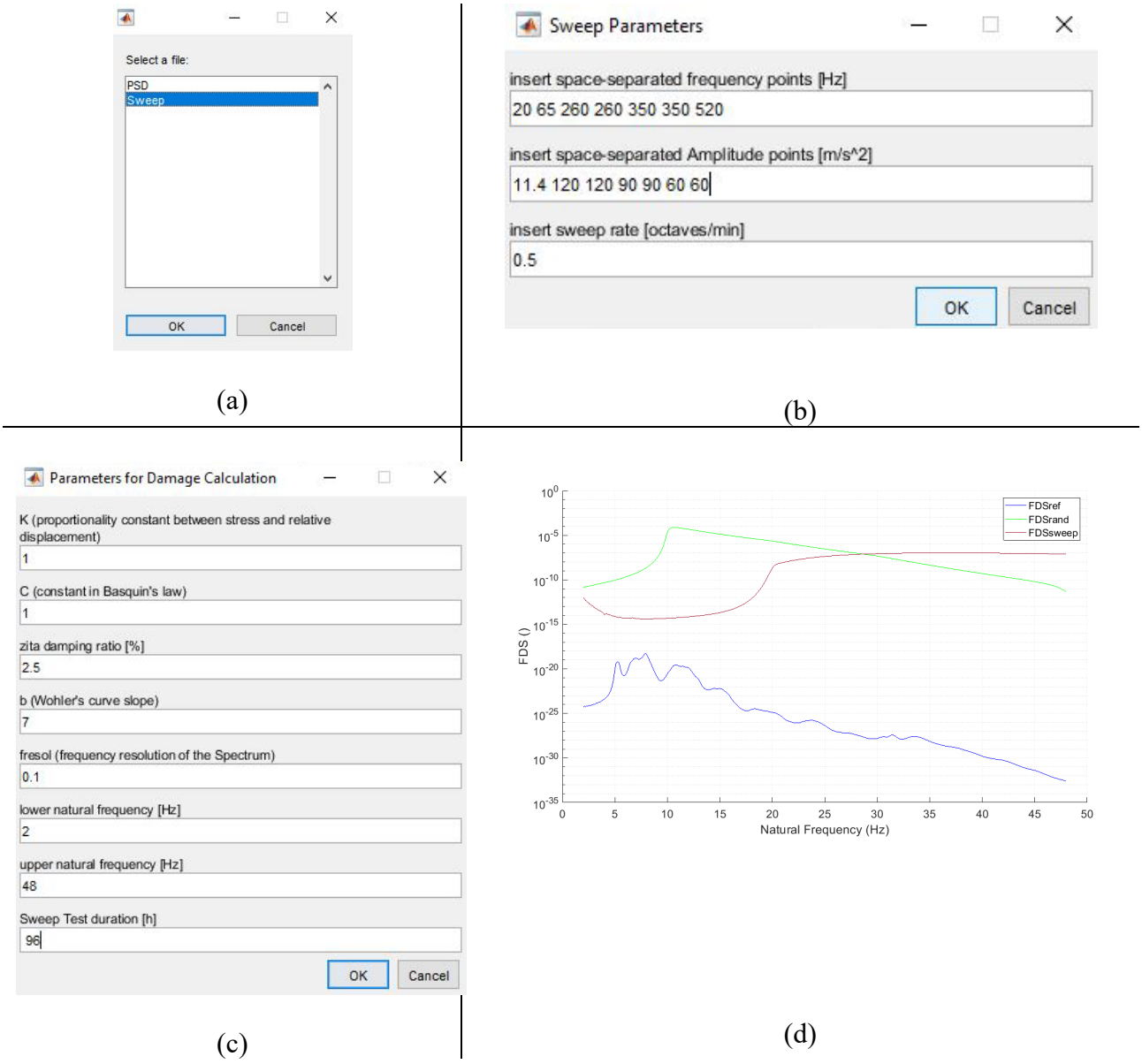

Fig.H.4: after clicking on the "Insert specification" button, the sweep specification is selected (a). Then, the sweep amplitudes are input (b) and the parameters that lead to the calculation of the *FDS* are inserted (c). Finally, the *FDS* of the sweep and *PSD* specifications are compared with the *FDS* of the reference signal (in this case the comparison is made only in the range 0-50 Hz).

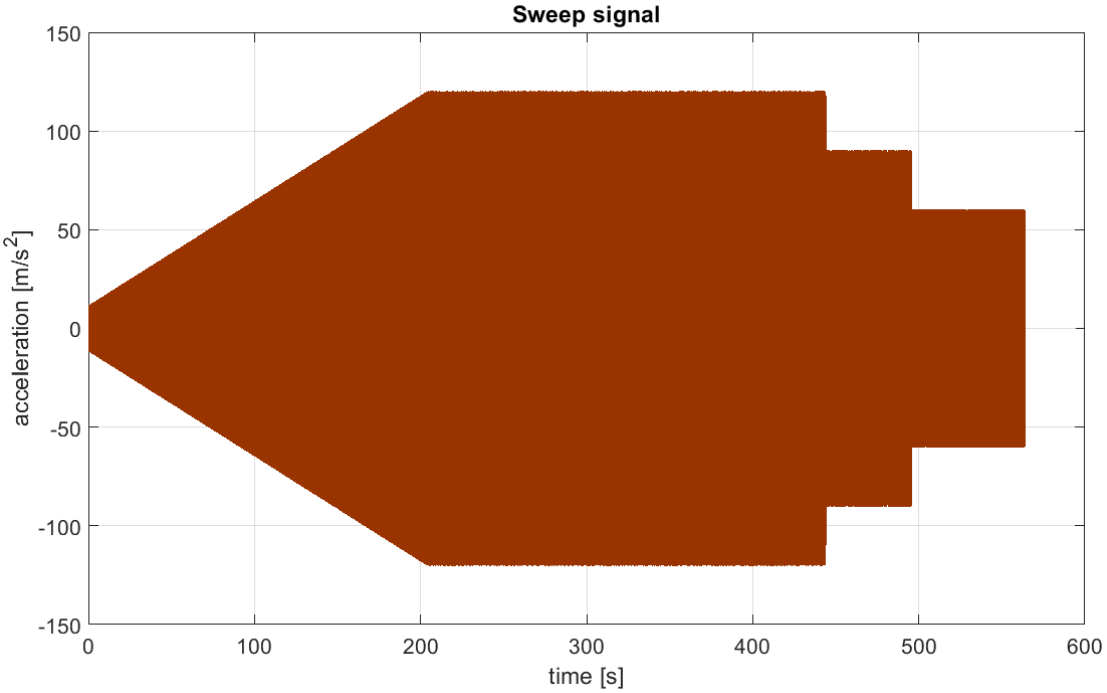

Fig.H.5: sweep specification in the time domain. According to the specification, this signal is repeated until 96 hours are reached.